The Dissertation Committee for Sareh Kouchaki Certifies that this is the approved version of the following Dissertation:

Improving Pavement Surface Texture Using Laser Scanning and Numerical Analysis

Committee:

Jorge A. Prozzi, Supervisor

Peter Müller

Raissa Ferron

Christian Claudel

Improving Pavement Surface Texture Using Laser Scanning and Numerical Analysis

by

Sareh Kouchaki

Dissertation

Presented to the Faculty of the Graduate School of

The University of Texas at Austin

in Partial Fulfillment

of the Requirements

for the Degree of

Doctor of Philosophy

The University of Texas at Austin

August 2019

To my husband Hossein,

To my parents Fakhri and Rasool,

To my brother Mohammad Reza,

And to my sister Azadeh.

Acknowledgements

My sincere gratitude goes to my supervisor Dr. Jorge A. Prozzi for his continuous guidance, encouragement, and support throughout my Ph.D. study. I have thoroughly enjoyed working with him, and I have learned a lot. It is a great honor for me that I had him as my supervisor.

I would also like to express thanks to my dissertation committee members, Dr. Christian Claudel, Dr. Peter Müller, and Dr. Raissa Ferron, for their time, support, and valuable comments for this dissertation. Special thanks are extended to my friends at UT Austin, Joaquin Bernardo Hernandez, Yorguo El Hachem, and Natalia Zuniga Garcia for their support during the field tests and working with me.

I want to extend my sincere appreciation to the Texas Department of Transportation (TxDOT)'s Materials and Tests Division for their support in this research. I really appreciate Richard Izzo, Edward Morgan, Jeffrey Prabo, and Michael Dawidczik for answering questions, providing the aggregate particles. I would also like to acknowledge the funding support that I received from the US DOT University Transportation Center (UTC) program and TxDOT during my Ph.D. studies.

Finally, the endless love and support of my husband, Hossein Roshani, and my parents, Fakhri Hosseini and Rasool Kouchaki, are greatly appreciated. You continue to be the inspiration in my life.

Abstract

Improving Pavement Surface Texture Using Laser Scanning and Numerical Analysis

Sareh Kouchaki Ph.D.

The University of Texas at Austin, 2019

Supervisor: Jorge A. Prozzi

Safe roads need pavement surfaces that provide an adequate level of skid resistance to reduce accidents, especially under wet conditions. The extent of skid resistance available on any given pavement is dependent on the design of the surface texture. When the pavement surface texture is worn, the tire-pavement friction decreases and consequently the safety of the road users is reduced.

Proper aggregate selection before construction helps in preserving adequate levels of skid resistance over the service life of the pavements. The critical engineering features expected from aggregates are their surface texture and resistance to the polishing actions of traffic. Currently, there are no standard quantitative test methods to measure the surface texture of aggregate particles directly. Besides, the existing laboratory test procedures used to evaluate the polishing resistance of aggregates are time-consuming, subjective, and cannot appropriately represent their frictional properties. A laboratory protocol is needed to assess the quality of aggregate particles for frictional purposes accurately.

Investigating the changes in pavement macrotexture is also required during the life of pavements to assess the potential skid-related problems and reduce crashes effectively. The pavement macrotexture is predominantly described by the Mean Texture Depth (MTD) using the Sand Patch Test (SPT), and by the Mean Profile Depth (MPD) using non-contact single-point profilometers. The reliability of the SPT is questionable because it is operator-dependent and the MPD calculated using a single texture profile cannot adequately describe the pavement texture. The limitations of the current measuring methods for pavement texture have directed researchers toward looking for new, more objective, accurate and reliable technologies that could potentially contribute towards better pavement surface texture evaluation. With a better texture characterization, highway agencies can better assess the level of skid resistance of their highway network with the aim of ensuring safer roads for the public.

The main contributions of this dissertation include a series of procedures and algorithms, developed using a high-resolution line laser scanner (LLS) prototype, to improve capturing and characterizing hot-mix asphalt (HMA) pavement surface texture. The methods and algorithms that have been developed in this dissertation include: 1) An outlier and spikes removal technique and set of criteria employing several filters to create clean 3D models of pavement surfaces, 2) A methodology to obtain the micro- and macrotexture of the surface profiles captured by the LLS, and automatically calculate the MPD based on pavements 3D texture data, 3) An algorithm to mimic the SPT on pavements 3D models and to automatically estimate the MTD based on the 3D texture data, 4) A new approach for quantification and differentiation the aggregates surface texture by using spectral analysis, 5) Using the Micro-Deval machine along with the LLS to develop a method for measuring aggregate polishing resistance, and 6) To categorize

the aggregate particles based on their polishing resistance using model-based clustering techniques.

This study was complemented by conducting a series of experimental field tests to compare the performance of the developed macrotexture characterization algorithms with current test methods. Results confirmed that the proposed algorithms could provide efficient, reliable, repeatable, and accurate measurements of the pavement surface macrotexture. Laboratory experiments were also conducted to characterize the polishing properties of seven types of aggregates based on their texture evolution. Following the polishing process, surface elevation profiles were obtained using the LLS and analyzed to determine the rate of change in the surface texture of aggregate samples. Texture measurements were carried out by using several texture parameters. Both visual examinations and statistical analysis were used to identify the differences between the aggregates polishing properties. The results showed that the polishing tendency of aggregates evaluated could be grouped according to the rate of change in surface texture.

Table of Contents

List of Tables

List of Figures

Chapter 1: Introduction

BACKGROUND

Worldwide, approximately 1.25 million people die annually as a result of road crashes, an average of 3,425 deaths a day. An additional 20 to 50 million are injured or disabled (*World Health Organization, 2015*). In addition to the loss of life, vehicle crashes have economic consequences as well. In order to reduce the number of accidents, the contributing factors must be controlled. Poor roadway conditions, primarily under wet weather, have been identified as a significant contributing factor in roadway accidents. Vehicle's loss of traction and skidding alone contributes to 15 to 35% of accidents that occur under wet conditions (*Horner et al., 2002*).

The tire-pavement interaction is what dictates the safety of motorists. The direct force developed at the tire-pavement interface is known as *skid resistance*, a property defined by the features of the tire, the vehicle speed and the pavement condition and texture (*Asi, 2007; Wang and Wang, 2013; Chen et al., 2017*). In wet conditions, the water film covering the pavement decreases the contact between the tires and the pavement surface; consequently, wet pavements provide a lower level of skid resistance to tires as compared to dry pavements (*Flintsch et al., 2005; Jayawickrama and Thomas, 1998*).

Many studies have related pavement skid resistance to accident rates. For instance, Kamel and Musgrove found that in pavement with high skid resistance, the wet weather crashes reduced by 54%. Miller and Johnson noted that an increase in average pavement skid resistance from 0.4 to 0.55 would result in a 63% decrease in wet-pavement crashes. Furthermore, Kamel and Gartshore reported that by improving the skid resistance, the rate of wet weather crashes reduced by 71% in intersections and 54%

on freeways (*Kamel and Musgrove 1981; Miller and Johnson, 1973; Kamel and Gartshore, 1982*). The relationship between the pavement skid resistance and the rate of crashes indicates that it is necessary for every highway management system to assess pavement skid resistance, especially in wet weather conditions with the purpose of reducing the rate of accident and improving the safety of road users.

Many devices are currently being used for measuring pavement skid resistance. All these devices have a common principle: they measure the resistance between a sliding tire and wetted surface of pavement while the tire is being dragged on the pavement (*Austroads, 2005*). These friction measurement devices require a truck carrying a large water tank to wet the surface at a defined level. Accordingly, the range of measurement depends on the amount of water carried on the truck. For long pavement projects, this tank needs to be filled too frequently which is not efficient in terms of both cost and time. Also, factors like water film thickness, temperature, measurement speed, rubber aging, rubber wear, and road evenness and curviness affect the skid resistance measurements and are difficult to control. So, skid resistance is not a fixed number but is a random variable.

The extent of skid resistance on any given pavement is dependent on the design of the surface texture—specifically its micro- and macrotexture. Pavement microtexture is defined as the pavement surface irregularities with characteristic dimensions along the surface of less than 0.5 mm while the pavement macrotexture is defined as texture irregularities with the wavelengths of 0.5 mm to 50 mm (Henry,1996). Microtexture, as the surface texture of aggregate, breaks up the continuity of the thin water film on the pavement and provides frictional resistance at the tire-pavement layer by generating intermolecular bonds. Macrotexture, which is known as an overall characteristic of asphalt mixture, prevents hydroplaning by providing surface drainage at the tire-

pavement interface that increases the wet frictional resistance (*Henry, 1996; Masad et al., 2009*).

Regardless of the surface microtexture amount, lack or shortage of macrotexture results in a weak contact between the pavement and tire. Vice versa, a rough macrotexture is not sufficient enough by itself to provide water drainage at the pavement-tire surface without the need for microtexture. The majority of pavement surfaces fall in between these two scenarios with a medium amount of macrotexture, in which the microtexture would play an essential role in providing adequate friction in wet conditions (*Dunford, 2013*).

When the pavement surface is worn, the tire-pavement friction decreases, consequently reducing the safety of the road users. As the pavements get older with the passage of the time, traffic polishes off the microtexture of the pavements continuously. Therefore, the type of aggregates used in the pavement surface plays an essential role in this phenomenon. Wearing course aggregates are required to have two characteristics: first, being rough-surface-textured, and second, being resistant to polishing by traffic to provide enough microtexture which is crucial for skid resistance (*Mahone and Sherwood, 1995; Webb, 1970*). The aggregates frictional properties and their capability of being resistant to polishing should be considered before any pavement construction. Failing to consider these factors in mix design would result in extra expenses in surface treatment and maintenance.

In addition, investigating the changes in pavement macrotexture is required during the life of pavements to assess the potential skid-related problems and reduce crashes effectively. Evaluating and understanding of the condition of the road surface

texture could lead to improved tolls to trigger maintenance activities which, in turn, could lead to increased skid level and safety.

PROBLEM STATEMENT

Several laboratory procedures are used to measure the aggregates' polishing resistance using the aggregate bulk properties. The Los Angeles abrasion test (*ASTM C535*), Micro-Deval (*AASHTO T 327*) are among those procedures. There is no standard test method to quantitively investigate the changes in aggregate surface texture due to polishing and to classify them accordingly.

In addition, in terms of assessing pavement macrotexture, the methods highway agencies currently use to determine the adequacy of pavement texture present several issues. For example, the sand patch test (SPT), specified under *ASTM E965*, is widely used these days to measure the mean texture depth (MTD) of pavements. Although the SPT is relatively inexpensive and straightforward, this test is subject to human errors and is affected by low repeatability and reproducibility. The errors mainly arise from volume and diameter measurements. Also, this test relies on the operator's ability to spread the material into a circular patch. Operator error could result in a circle that overestimates the area formed by sand and underestimates the MTD. Furthermore, the SPT can be affected by wind, as losing sand throughout the testing process can skew the results and likewise overestimate the available texture. If the factors promoting human error can be eliminated from the MTD measurements, the reliability of the results would improve significantly and, hence, the decisions taken based on them.

Laser-based devices such as Circular Track Meter (CTM) and high-speed profilers have been used recently to measure pavement surface texture automatically without operator intervention. However, these devices only capture a single texture

profile of the pavement surface. Given the fact that the footprint of a tire on a pavement covers an area, a unique profile can partially capture the texture information. For more comprehensive and accurate measurements of the texture depth at the interaction of the tire and pavement, three-dimensional (3D) texture measurement is needed.

RESEARCH MOTIVATION

Recently, a great variety of scanning tools have been developed and widely employed in various fields such as medicine, mechanical engineering, etc. These instruments allow the scanning of objects in variable sizes and on different scales. With the recent development in laser scanning technologies and the vast improvement in the computing and processing power of computers, it is now feasible to characterize the 3D pavement surface texture with high resolution and in a timely, labor-efficient, and objective manner. Besides, these advanced techniques can be used to obtain accurate quantification of the aggregate texture properties, hence addressing the limitations of the current methods.

RESEARCH SCOPE AND TASKS

The primary goal of this dissertation is to improve the characterization of the pavement surface micro- and macrotexture. Within the scope of this study, a high-resolution line laser scanner (LLS) prototype was developed. This laser scanner was used to scan pavement surfaces and aggregate particles and collect 3D surface texture data. Several objectives were considered to achieve the goal of this study:

1. Preprocessing the collected 3D data using signal and image processing techniques.

2. Developing algorithms to automatically calculate the pavement texture depth based on the 3D texture data.
3. Use the Grip-Tester to collect continuous friction data at traffic speed, calculate the MPD values of texture data and perform statistical analysis to establish correlations between texture and friction.
4. Developing a methodology to digitalize the SPT and to estimate the MTD of pavement surfaces automatically.
5. Developing a methodology to determine the difference in surface texture on different aggregate particles using Fourier Transform and power spectral density (PSD).
6. Developing an aggregate classification framework based on their texture properties.

This research study involves the following tasks:

Task 1: This task consisted of performing a comprehensive literature review covering pavement friction, friction measuring methods, assessing the relationship between friction and pavement texture, and evaluating the recent advances in measuring pavement micro- and macrotexture.

Task 2: This task involved laboratory investigations that included scanning pavement surfaces and aggregate samples using the LLS prototype to specify procedures for accurately collecting data and processing them. In this task, data mining techniques were employed to overcome potentially undesirable outputs caused by the noise in the raw data and accurately reconstruct 3D models of the scanned objects.

Task 3: This task included two parts: a) developing algorithms for determining the MPD and MTD; and b) validating the reliability and repeatability of the developed algorithms.

As part of this task, several field tests were performed to collect data on different pavement sections.

Task 4: In this task, a new method to measure aggregates surface texture using the LLS prototype and spectral analysis was established. For this purpose, a methodology was developed to obtain the micro- and macrotexture of aggregate particles. The surface textures of various aggregates were analyzed using numerical methods such as discrete Fourier transform and power spectral density (PSD). By means of statistical analysis on PSD results, the most effective components of microtexture were selected and compared to statistical surface parameters: root mean square roughness (Rq) and depth of surface smoothness (Rp).

Task 5: In this task, an experimental study was performed to validate the methodology developed in Task 4. Samples of coarse aggregates from several sources across TxDOT were evaluated. Aggregate texture measurements were carried out on two samples of aggregates: non-polished particles and polished particles. The surface texture profiles were captured employing the LLS prototype. Then, the methodology developed in the previous task was applied to check its feasibility in capturing the variation in the surface texture of aggregates.

Task 6: In this task, an aggregate classification system based on their surface texture was developed. This task consisted of several steps: 1) collecting several quarry aggregate samples; 2) scanning aggregate particles using the LLS prototype; 3) processing the scan data to remove noises and outliers; 4) computing the surface texture of aggregate particles using the derived parameters; 5) applying a clustering approach to categorize aggregate particles.

RESEARCH ORGANIZATION

This dissertation is divided into seven chapters. Chapter 1 presents a brief introduction to the topic with the problem statement and research motivation. The goal and objectives are stated in Chapter 1 as well. Chapter 2 presents the background for the study and reviews pavement surface friction and its generation mechanisms as well as the pavement surface texture and its characteristics that are important for tire/road friction generation. A review of the related research studies is also contained in Chapter 2. The configuration of the laser scanner used in this study, its components, and preprocessing steps of the texture data are illustrated in Chapter 3. Texture capturing and measuring methods developed in this study are described in three chapters: 4, 5, and 6. In Chapter 7, conclusions are drawn from the results and recommendations are presented.

Chapter 2: Literature Review

PAVEMENT FRICTION

According to the AASHTO Guide for Pavement Friction, "pavement friction is the force that resists the relative motion between a vehicle tire and a pavement surface." The coefficient of friction μ, a dimensionless ratio, is a measure of the friction between tire and pavement (*Flintsch et al., 2012*). It is obtained by dividing the tangential force resisting the motion of the vehicle (F) by the normal force pressing the vehicle to the surface (F_W). These Forces are illustrated in Figure 2.1. Friction provides the driver with the ability to control and maneuver the car by ensuring the ability to stop, accelerate, reduce speed, change lanes, turn, and perform other maneuvers.

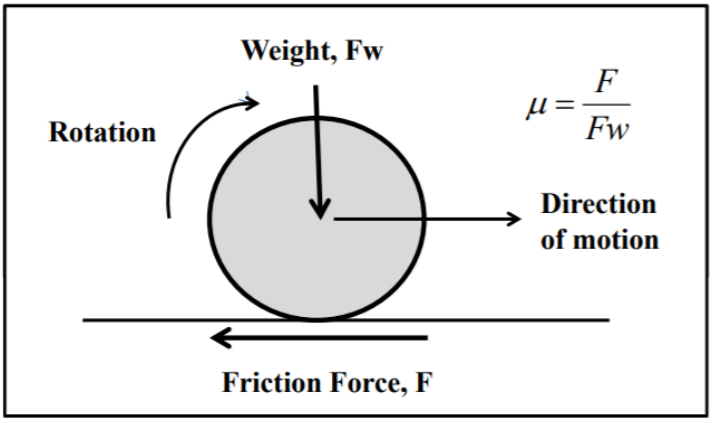

Figure 2.1: Friction Force Diagram (Flintsch et al., 2012).

There are many devices currently used for measuring pavement friction, which can be categorized into three groups based on the measurement principles: longitudinal friction coefficient (LFC), transverse, and stationary or slow-moving *(Descornet et al., 2006; Do and Roe, 2008*). The LFC measurement principle aims at measuring friction

Some sections of this chapter were previously published in Kouchaki et al., "Evaluation of aggregates surface micro-texture using spectral analysis," Journal of Construction and Building, vol. 156, pp.944–955, 2017, and Kouchaki et al., "Field Investigation of Relationship between Pavement Surface Texture and Friction," Journal of Transportation Research board, vol. 2672, p. 395-407, 2018. The author of this dissertation contributed to these published articles by designing the research methodology, collecting and analyzing the data, and preparing the manuscript.

when a vehicle is traveling forward in a straight line. When the brakes are applied, both the angular velocity of the wheel and the overall velocity of the vehicle decrease. When the braking force on the wheels is too strong, the wheels are "locked" and consequently slide over a surface. LFC measurement devices can apply slip ratios that simulate the wheel slipping process when a wheel slides over a surface. More specifically, the slip ratio compares the vehicle's velocity to the angular velocity of the wheel. When the slip ratio is 0.0, the angular velocity of the wheel is the same as the velocity of the vehicle (i.e., no slip between wheel and surface). When the slip ratio is 1.0, there is no angular velocity in the wheel (i.e., the wheel is fully locked and slides over the surface). LFC devices can have either a fixed or a variable slip ratio *(Kane et al., 2013; Do and Roe, 2008)*.

The stationary or slow-moving measurement principle is used in compact devices usually found in the laboratory or still testing. One such device uses a pendulum arm; others, such as the Dynamic Friction Tester (DFT), use a rotating head. Both devices use rubber sliders that use the surface friction to slow down the pendulum or the rotating head *(Descornet et al., 2006; Do and Roe, 2008; Andriejauskas et al., 2014)*.

Table 2.1 summarizes LFC measurement devices commonly used around the world. LFC devices can measure between 3.1 and 87 km/h and can come in the form of compact trailers or large-capacity trucks. LFC devices use a watering system, requiring vehicles to carry a water tank for measurement purposes.

Transverse friction measurement devices are usually larger, more expensive, and can take measurements for longer distances since greater water capacity increases maximum measurement distance. While inexpensive and easy to use, stationary or slow-moving devices must be operated manually and require traffic control *(Andriejauskas et al., 2014)*.

Device Name	Theoretical water film thickness (WFT), Speed, Tire type, Measurement interval (Interval)	Assembly	Device Picture
ADHERA	TWFT: 1 mm Speed: 40–120 km/h Tire type: Smooth PIARC tire 165R15 Interval: 20 m Country/Countries of Use: France	Assembly: Trailer that can be hooked up to a vehicle Commercially Available: No	
BV-11	TWFT: 1 mm Speed: 20–160 km/h [C] Tire type: Trelleborg tire T49 Interval: 20 m Country/Countries of Use: England, Sweden, and Finland	Assembly: Trailer that can be hooked up to a vehicle Commercially available: Yes	
Grip-Tester	TWFT: 0.5 mm Speed: 5–100 km/h Tire type: Smooth ASTM tire, 254 mm diameter Interval: 10 or 20 m Country/Countries of Use: United States, United Kingdom, and others	Assembly: Trailer that can be hooked up to a vehicle. Commercially available: Yes	
ROAR DK	WFT: 0.5 mm Speed: 60–80 km/h Tire type: ASTM 1551 Interval: 5m + Country/Countries of Use: Denmark	Assembly: Trailer that can be hooked up to a vehicle Commercially available: No	
ROAR NL	TWFT: 0.5 mm Speed: 50–70 km/h Tire type: ASTM 1551 Interval: 5–100 m Country/Countries of Use: Netherlands	Assembly: Three-axle tanker truck with two measuring systems mounted at the rear of the chassis. (Tank capacity is about 12,000 liters.) Commercially available: No	
RWS NL	TWFT: 0.5 mm Speed: 50 – 70 km/h Tire type: PIARC smooth 165 R15 Interval: 5 – 100 m Country/Countries of Use: Netherlan ds	Assembly: Trailer that can be hooked up to a vehicle. Commercially Available: No	

Table 2.1 Continued

Skiddometer BV-8	TWFT: 0.5 mm Speed: 40–80 km/h TT: AIPCR ribbed, 165 R15, with four longitudinal grooves Interval: 30–50 m Country/Countries of Use: Sweden	Assembly: Trailer that can be hooked up to a vehicle Commercially available: Yes	
SRM	TWFT: 0.5 mm Speed: 40–80 km/h TT: AIPCR ribbed, 165 R15, with four longitudinal grooves Interval: 20 m Country/Countries of Use: Germany	Assembly: The test wheels are mounted on the back of a tanker vehicle at the approximate location of a vehicle tire paths. Commercially available: No	
TRT	WFT: 0.5 mm Speed: 40–140 km/h Tire type: Smooth ASTM Interval: Typically, 20 m Country/Countries of Use: Czech Republic	Assembly: The measuring equipment is under a specially equipped vehicle Commercially available: No	
SRT-3	WFT: 0.5 mm Speed: 30–90 km/h Tire type: Tire with thread (200kPa) Interval: 100 m Country/Countries of Use: Poland	Assembly: Trailer that can be hooked up to a vehicle Note: SRT-3 is more sensitive to micro-texture changes than to macro-texture changes. Commercially Available: No	
IMAG	WFT: 1.0 mm Speed: up to 140 km/h Tire type: PIARC smooth profile tire Interval: N/A Country/Countries of Use: France, Germany, and Poland	Assembly: Trailer that can be hooked up to a vehicle Commercially available: Yes	
ICC	WFT: 1.0 mm Speed: 65 to 80 km/h Country/Countries of Use: The United States, and others	Assembly: Trailer that can be hooked up to vehicle Commercially available: Yes	

Table 2.1: Comparison of the LFC Measuring Devices ((Descornet et al., 2006; Do and Roe, 2008; Andriejauskas et al., 2014).

FACTORS AFFECTING FRICTION

Generally, factors affecting pavement friction can be grouped into three major categories: weather condition, vehicle properties, and roadway condition.

Weather Condition

The friction between tire and pavement is affected by the presence of water, in the form of rainfall or condensation. Under wet conditions, the potential for hydroplaning increases. Under this situation, braking and steering effectiveness is reduced, and the vehicle becomes uncontrollable. Persson et al. stated that the reduced friction contribution of rubber results because of the smoothened pavement surface caused by water that decreases the viscoelastic deformations of rubber in contact with surface asperities (*Persson et al., 2005*). Accordingly, it is important to avoid having thick layers of the water film on the pavement. Its effect on friction is minimal at low speeds (less than 20 mph); however, it increases exponentially at higher speeds. This effect is also influenced by tire design and conditions.

Vehicle Properties

In recent years, vehicles have increased the number of safety features incorporated. The Anti-lock Braking System (ABS) allows the wheels to maintain tractive contact with the road surface while braking, preventing the wheels from locking up (ceasing rotation) and avoiding uncontrolled skidding. The tire tread design (type, pattern, and depth) and condition (tear and wear), as well as the tire inflation pressure, have a critical impact on the friction, especially when water accumulates on the pavement surface. New ribbed tires are preferred to ribbed or smooth thoroughly worn tires. Under-inflated tires can considerably reduce friction at high speeds. On the other hand, tire over

inflation causes only a small loss of pavement friction (*Henry, 1983; Kulakowski et al., 1990*).

Roadway Condition

The capacity of the roadway surface texture to resist polishing and abrasion under accumulated traffic repetitions is directly related to the ability of the pavement to maintain a good level of the surface friction. Pavement friction is a time-dependent parameter. During the first years after construction, it is common to have crash accidents due to the low pavement friction because the asphalt binder is covering the aggregate particles. Once this binder film is worn away, and the surface of the aggregates are exposed by the passage of vehicles, the friction levels are increased. Then, depending of the abrasion resistance of the aggregates, friction will decrease during the pavement life. The rate of friction change during a pavement life depends upon the type of its surfacing material (*Do et al., 2007; Woodward et al., 2002*).

Among the factors mentioned above, pavement surface texture is the one that highway agencies can control. A detailed study illustrating the association between pavement texture and friction is be covered in the following sections.

PAVEMENT TEXTURE AND FRICTION

Skidding resistance is the term utilized to express the contribution of the road pavement to the formation of friction *(TRL, 2002*). The extent of skid resistance on any given pavement is dependent on the design of the pavement surface texture *(Henry, 2000*). The deviations of the pavement surface from a true planar surface is known as pavement surface texture (*ASTM E867, 2012; Hall et al., 2009*). The World Road Association, previously the Permanent International Association of Road Congresses

(PIARC), has categorized pavement texture by a range of wavelength (λ) and amplitudes (A). The standard specifications, such as the American Society of Testing Materials (*ASTM E867, 2012*), International Organization for Standardization, and German Institute for Standardization (*DIN on ISO 13473-1*), accepted and incorporated these definitions. The ISO 13473-1 refined the terms incorporating typical amplitudes as follows (*Sandberg, 1998*):

- Unevenness (500 mm < λ < 50 m, A > 50 mm, where λ is wavelength and A is amplitude).
- Megatexture (50 mm < λ < 500 mm, A = 0.1 to 50 mm).
- Macrotexture (0.5 mm < λ < 50 mm, A = 0.1 to 20 mm).
- Microtexture (λ < 0.5 mm, A = 1 to 500 μm)

As shown in Figure 2.2, unevenness is the major deviation that is felt by a bouncy behavior of the vehicle on the road. It has a significant effect on the safety and comfort of riding on a highway because of its impact on dynamic parts of the vehicle. Mega-texture comprises surface irregularities like cracks, roughness, and potholes. Megatexture has wavelengths in the same order of size as the tire/pavement interface. It is strongly associated with noise and rolling resistance (*Lees, 1983; Hall et al., 2009; Kagbara et al., 2016*). Macrotexture refers to the large-scale texture of the pavement surface due to the aggregate particle size, aggregate gradation and arrangement. In asphalt pavements, the mixture properties (aggregate shape, size, and gradation) which define the type of mixture, control the macrotexture. In concrete pavements, the method of finishing (such as dragging, tinning, grooving or grinding), as well as the width, spacing, and direction of the texturing, controls the macrotexture *(Hall et al., 2009*). Microtexture refers to the

small-scale texture of the aggregate surface. Microtexture is a function of aggregate particle mineralogy, petrology, and source, and is affected by the environmental effects and the action of traffic (*Rezaei et al., 2009*).

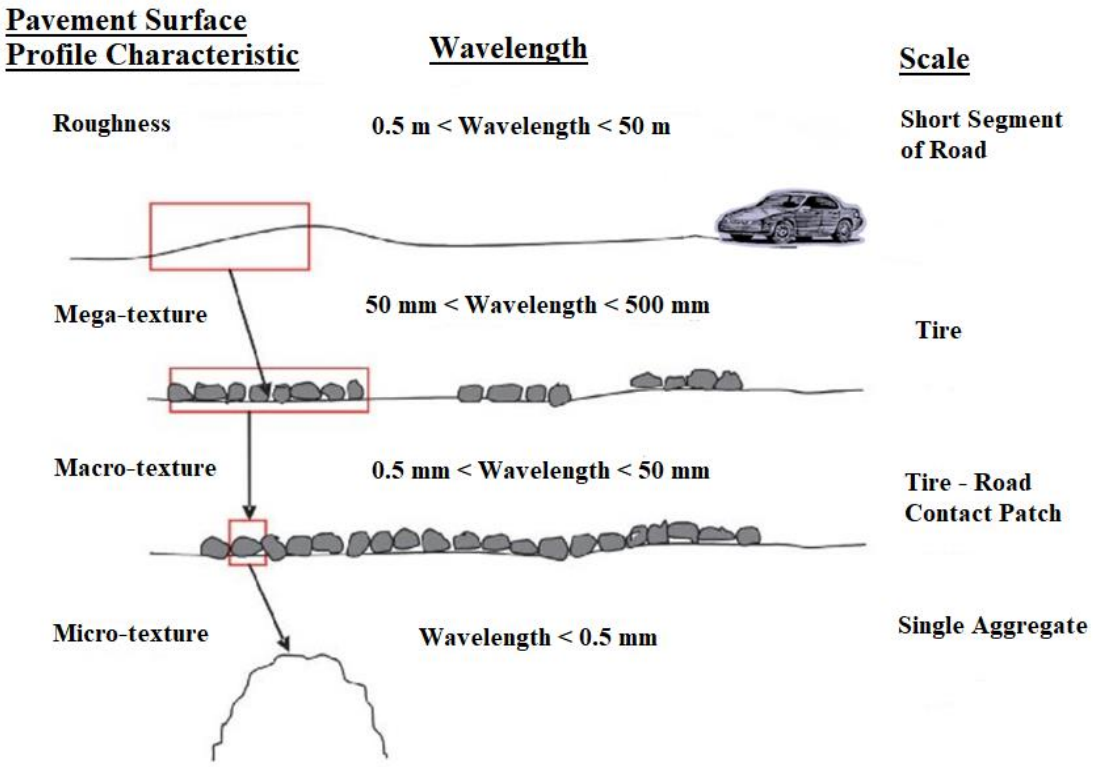

Figure 2.2: Pavement Texture Characterization (*Sandburg, 1998*).

Based on the unified theory of rubber and tire friction, by Hartwig W. Kummer, two main forces, adhesion and hysteresis, contribute to friction (*Kummer, 1966*). Although there are other components of pavement friction, such as tire rubber shear, they are insignificant when compared to the adhesion and hysteresis force components. Thus, friction can be viewed as the sum of the adhesion and hysteresis. As depicted in Figure 2.3, adhesion is the force developed when the tire and the pavement surface interlock.

The force is the result of the temporary bond formed between the rubber and the surface at the molecular level. During this phenomenon, the micro-asperities of both surfaces are bound to each other with Van der Waals forces providing the attractive force. The pavement microtexture is the main contributor to adhesion. On the other hand, hysteresis, is the force developed when the tire deforms while in contact with the pavement. When the vehicle travels over the roadway, the rough asperities compress and decompress the tire making it lose energy. Macrotexture plays a vital role in the development of the hysteresis component of friction which depends on energy loss due to tire compression and decompression (*Hall et al., 2009*).

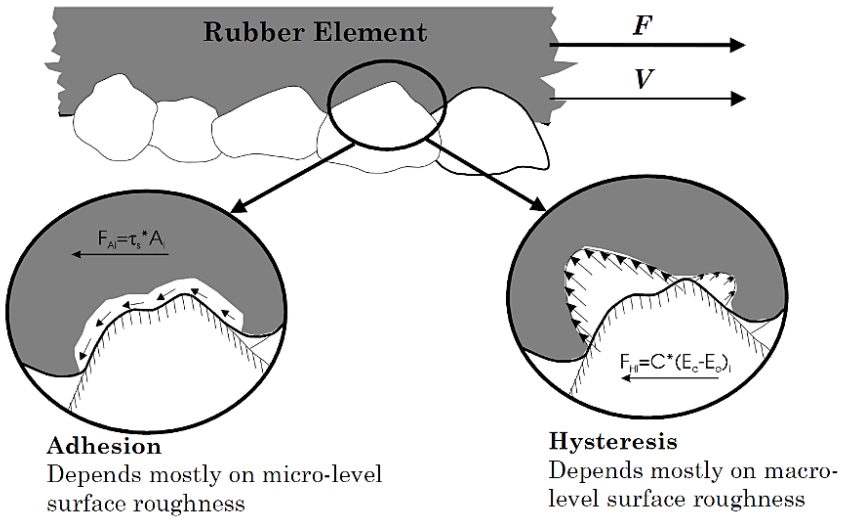

Figure 2.3: Adhesion and Hysteresis Components of Friction (*Hall et al. 2009*).

On wet pavements, macrotexture is responsible for the most substantial contribution for skid resistance. The pavement surface needs to have sufficient macrotexture to disperse water accumulated on the surface of the pavement rapidly to mitigate the potential for hydroplaning. However, the role played by microtexture under

wet pavements should not be disregarded. Microtexture is the component that is the most vital at low speeds yet still contributes to friction at relatively higher speeds. Savkoor (1990) pointed out the necessity of having a minimum microtexture height to arise from the water film. He also mentioned that the low thickness of the water film (few microns) provides high viscosity for which microtexture needs to be adequately sharp to break the water film.

Over the years, many efforts have been made to correlate the pavement friction and texture. These correlations specify how macro and microtexture affect pavement-tire friction. Ergun et al. (2005) measured friction and the texture of pavement on eighteen road sections with different surface characteristics in Belgium. A full-scale friction test was carried out by the Odoliograph at 20, 30, 40, 50, 60 80, and 90 km/h vehicle speeds, and macrotexture was measured by a laser profilometer at 36 km/h vehicle speed. Microtexture measurements of pavement core samples taken at the same sections were conducted in the laboratory using an image analysis system. After statistically analyzing both micro- and macrotexture, a prediction model was found to predict road surface friction at all speeds. Results indicated that, at any speed, there are substantial effects from both micro- and macrotexture on road surface friction. In another research study by Serigos et al. (2013), the friction and texture data were collected from 28 in-service flexible pavement surfaces. Macrotexture and microtexture data were collected using the CTM and the Laser Texture Scanner, respectively. The skid resistance was evaluated under wet conditions using a British Pendulum Tester. The researcher concluded that accounting for both the micro- and the macrotexture components of the surface can remarkably improve the prediction of skid resistance of flexible pavements. Ueckermann et al. (2014) collected pavement micro- and macrotexture under laboratory conditions by

the optical testing system. The researchers used two skid resistance devices to measure friction: a laboratory device called the W/S device, which corresponds to a locked-wheel braking test at a speed of 60 km/h, and the ViaFriction device, a tool developed for road and airfield monitoring purposes which measures the skid resistance under controlled longitudinal slip and is corresponded to ABS braking conditions. In this study, the rubber friction theory of Persson was applied to predict skid resistance using collected texture data. The authors found a close relation between measured and predicted friction coefficients. They concluded that a strong skid resistance could be measured without contact through measuring micro- and macrotexture.

MEASURING PAVEMENT TEXTURE

The connection between the pavement's skid resistance and surface texture makes pavement texture a vital topic for highway agencies and state Departments of Transportation (DOTs) to address; pavement texture issues are of particular importance in wet conditions. Pavement texture is a critical factor to maintain desired pavement skid resistance, and it is recognized as a safety factor contributing to crash ratios (*Hall et al., 2009; Roe et al., 1991; Roe et al., 1998*).

Standard Measuring Methods

Currently, SPT, CTM, and high-speed profilers are the commonly used methods to judge the adequacy of the pavement texture in terms of the MTD and MPD. SPT (as shown in Figure 2.4) consists of spreading a predetermined volume of dry, uniformly graded, fine (Ottawa) sand on the pavement surface, and working it into a circular pattern of the maximum diameter through the circular motion of a small hand-held spreading tool. As provided in Equation 2.1, MTD is calculated from the bulk volume (V) of the

sand and the mean diameter (D) of the circular sand patch. Results of the test can be used in the field to assess the adequacy of texturing compared to specification requirements and to improve construction practices, where required. The test is quick and straightforward, but still involves traffic control measures to ensure the safety of the operators. The test has a well-defined procedure and controlled test method detailed within ASTM E965 (ASTM E965, 2006).

$$\mathbf{MTD} = \frac{V}{\frac{\pi D^2}{4}} \qquad \textbf{Eq 2.1}$$

Figure 2.4: Sand Patch test.

Several studies have been conducted to assess the reliability of the SPT. In 1974, J.G. Rose conducted a study measuring the mean texture depth using the sand patch. He mainly focused on measuring the skid resistance of the pavement surface and the average surface texture depth. Using the SPT, Rose measured 44 different pavements including open-graded and dense-graded asphalt concrete, chip-sealed and fog-sealed asphalt concrete, and deeply textured, smooth, and grooved PCC (Portland Cement Concrete) pavements. Instead of measuring a circle like the previous sand patch method discussed, Rose used a volume of sand required to fill a 12-inch square aperture, and the average texture depth was computed using the volume and the area. Two same tools were used by two different operators to test the same locations accounting for a total of 160 tests. From

the results, he found that the SPT had poor repeatability. The results of the SPT were compared to the results from the California Portable Tester and towed trailer skid testing equipment. The towed trailer skid tester determined the skid resistance of the right wheel track. At higher texture depths, there was a general trend of higher skid numbers and coefficients of friction. They were unable to find a relationship between texture depth and both skid number and speed gradient due to poor repeatability.

In 1982, Chamberlin and Amsler also conducted a study on the variability of the sand patch test. Their objective was to determine the number of tests that should be performed to acquire an accurate MTD. They observed the level of precision of different samples focusing mainly on the variability in the precision of the measurements. These deviations in the precision were caused by human error and sampling error. By measuring these errors, they were able to judge the repeatability of the sand patch test. Human error includes variability in "single-operator precision," or repeatability, and "multiple-operator precision," or reproducibility. The first consists of the repeatability of a single person taking multiple measurements and getting precise results. The other consists of the similarity between different people's estimations. Their findings showed that there was a greater standard deviation in the multiple-operator precision than the single-operator precision.

The sand patch test will always be operator dependent. If human error factors can be minimized during MTD measurements, the results can show more accuracy and precision. This is why efforts to measure the pavement texture depth using a laser-based device have being concerted around the world. The CTM and high-speed profilers are the laser-based methods developed to measure the pavement texture depth in terms of MPD. According to ASTM E2157, the CTM (shown in Figure 2.5) consists of a laser-

displacement sensor that rotates over a circle with a diameter of 284.5 mm (11.2 in.) and measures the profile of pavement surface texture. The profile includes 1,024 points scanned at an interval of 0.87 mm (0.034 in.). Using the instructions provided by ASTM E 1845, the measured profile then is sectioned into eight equal parts, and the mean profile depth (MPD) in each part is measured. The CTM measures the MPD of pavements at a fixed location and requires traffic control. Accordingly, high-speed profilers have been developed to collect the MPD of pavements dynamically on the go without requiring stopping and traffic control (*Serigos et al., 2014*).

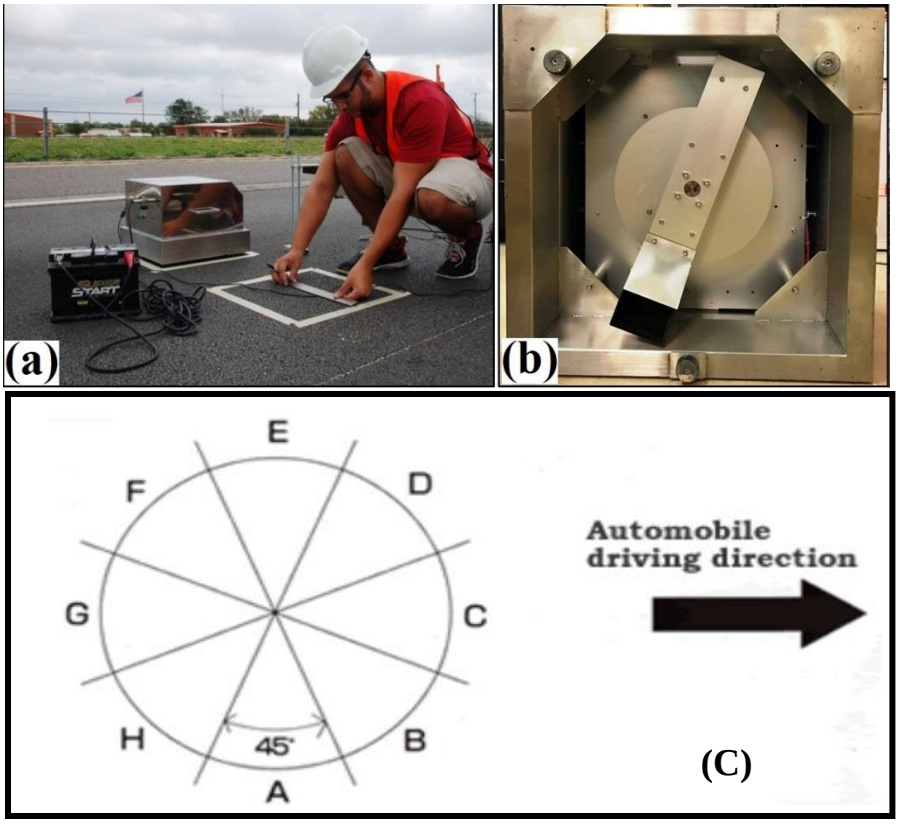

Figure 2.5 a) The CTM powered by a battery measuring the texture at the right wheel path, b) A bottom view of the CTM, and c) The scanned area by the CTM.

Flintsch et al. (2005) with the Virginia Department of Transportation conducted a study comparing macrotexture measurements taken with SPT and three other devices: (1) CTM, (2) International Cybernetics Corporation (ICC) profiler, and (3) MGPS profiler. Flintsch et al. compared the results of MPD measurements from these three different devices by creating a model that normalizes their results to that of the SPT. The results indicated that the CTM correlated the most with the SPT and the ICC profiler correlated the least. Besides, the researcher developed several models for converting the laser-based texture measurements to MTD.

Furthermore, in 2005, Hanson and Prowell evaluated the accuracy of the CTM by comparing the MPD results obtained using the CTM to MTD results of the SPT, and by assessing the repeatability and reproducibility of the CTM. Both MPD and MTD measurements were obtained in five random locations. The tests were carried out on 45 different pavement sections of the National Center for Asphalt Technology (NCAT) Test Track. The selected pavement sections have a variety of mix designs including coarse and fine dense graded Superpave mixes, Open-Graded Friction Course (OGFC), Hveem mixes, Stone Mastic Asphalt (SMA) and Novachip. Several correlations were developed between MTD and MPD considering the pavement type. The researchers concluded that the CTM is more variable than the SPT. However, the authors pointed out that less technician skill is required to operate the CTM.

Recent Advancement in Pavement Texture Measurement

Most existing profilers (e.g. CTM) collect surface texture data using a single-point laser, which results in a two-dimensional (2D) texture profile. Pavement texture varies depending on the direction of the measurement. Therefore, a 2D profile fails to describe characteristics of the texture completely. Besides, the current pavement texture

measurement devices are not able to capture the micro-level of pavement texture. Todate, high-resolution 3D texture surfaces can be readily measured using advanced line laser-based devices to overcome these issues. These new technologies could potentially contribute to better pavement surface texture measurement.

Various 3D laser scanners are currently on the market and have been used in a variety of researches. For instance, Miller et al., (2012) utilized the texture data collected by the stationary laser profilometer (SLP) to characterize the texture properties of pavement and estimate the frictional properties. SLP (as shown in Figure 2.6) is a high-resolution line laser-based stationary pavement texture profiler. The system yields excellent repeatability. SLP could capture both micro- and macrotexture of asphalt mixtures.

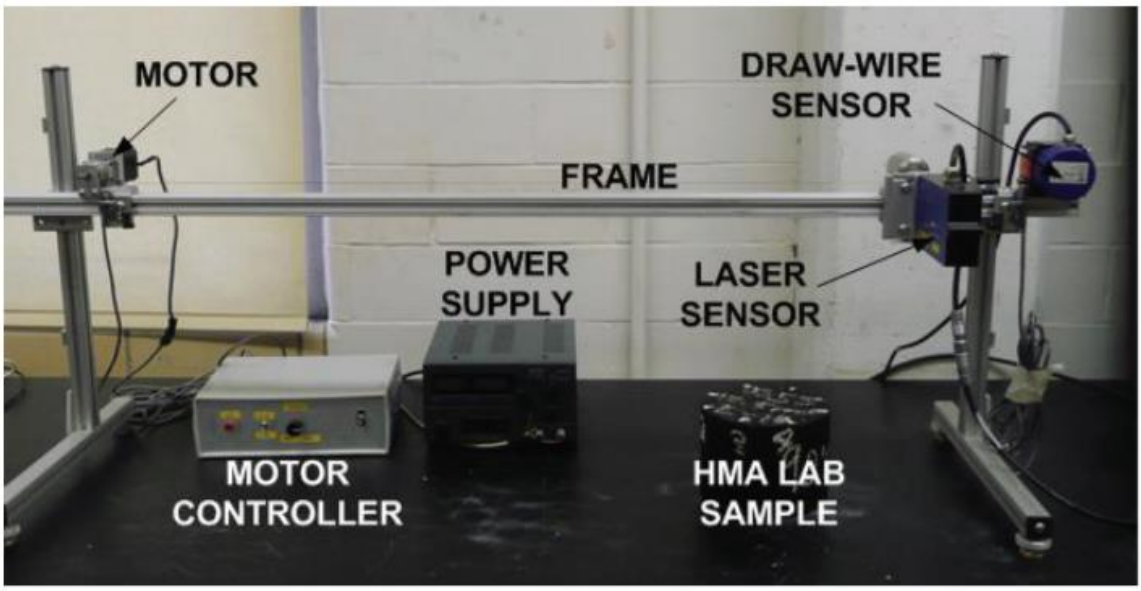

Figure 2.6: Stationary laser profilometer, (*Miller et al., 2012*).

The research study conducted by Bitelli et al., in 2012, describes an experiment on the use of 3D laser scanner techniques on various types of asphalt pavements for

texture characterization. This research study used the laser scanner produced by Next Engine Inc. A series of road pavement specimens cored on site and some others reproduced in the laboratory were scanned. The cylindrical samples used were representative of three different types of road pavement: Dense Graded Asphalt Concrete (DGAC), Open Graded Asphalt Concrete (OGAC) and Splitt Mastic Asphalt (SMA). The research aim was to quantify the texture of scanned specimens using 2D parameters which are calculated from surface profiles and 3D parameters, which are calculated based on the 3D texture data, and compare them. In addition to MPD, the texture parameters presented in Table 2.2 were used in this study. These parameters are detailed explained in ISO standards, i.e., ISO 13473, ISO 13565, ISO 25178, and ISO 4287. This study underlined that, although the pavement surface texture can be characterized by either 2D profile parameters or 3D surface parameters, 3D texture parameters could provide complete texture characterization. Besides, this study pointed out that 3D texture data offers higher potential for pavement surface evaluation by providing the possibility of creating new surface and volume parameters.

2D Texture Parameters & Description	**3D Texture Parameters**
R_a (Average Roughness)	S_a
R_{sk} (Skewness)	S_{sk}
R_{ku} (Kurtosis)	S_{ku}
R_t (Peak to Valley Height)	S_t
R_u (Levelling Depth)	S_u
R_m (Mean Depth)	S_m
Abbot Curve for a Single Profile and the Parameters: Rk, Rpk, and Rvk.	Abbot Curve for a Surface and the Parameters: Sk, Spk, Svk.

Table 2.2: 2D and 3D Texture Parameters.

In 2015, Liu and Shalaby., used a 3D surface measurement and analysis device, named LS-40, to collect and reconstruct concrete pavement surface texture. The objective

of this research was to investigate the surface texture of concrete containing nano-silica using the LS-40, to assess whether correlations exist between texture indices and the nano-silica content. LS-40 is a portable scanner which can be used either in a laboratory or in the field. This scanner (shown in Figure 2.7) scans a 4.5" by 4" areas and produces a high resolution of 0.01mm.

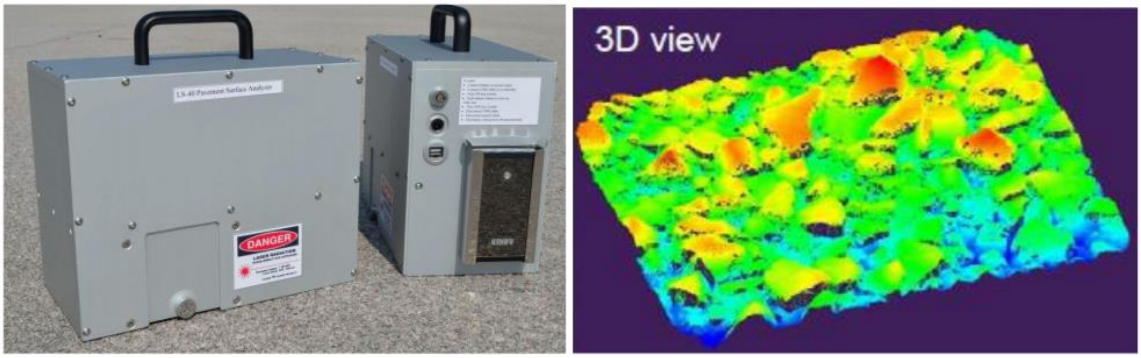

Figure 2.7: LS-40 Scanner and 3D Pavement Scan (*Yang, 2017*).

In 2012, Burak Sengoz assessed the determination of pavement surface texture depth by using a 3D Laser Scanner. The study entailed using a scanner including an enhanced sensor to inspect a full range of colors and depths on the selected asphalt pavement surface. The laser equipment was mounted on a portable vehicle attached to a portable computer (PC). The developed prototype measures texture using laser light. This study was conducted on sections which were exposed to the same environment but different traffic loading conditions. The results of the study showed that the 3D laser scanning produces results comparable with the SPT indicating that further development and research in this area is promising.

In this regard, in 2016, Hao et al. also studied the use of a laser texture meter to replace the sand patch method for measuring texture depth. The scanner device consisted of a charge coupled device (CCD) camera, a line-focused laser source, encoder, industrial

computer, global positioning system, uninterruptable power supply, and a vehicle carrying this equipment. The laser line can reach up to 1.0 mm width, and the wavelength is 808 nm. 3D data was collected automatically using the laser pulse reflection principle and laser triangulation. The laser collects height data points and a MATLAB algorithm processes these data points to remove any outliers due to noise. The main challenge in developing the MATLAB algorithm was that the outliers needed to be filtered out without removing pavement characteristics. The study objective was to develop an algorithm to make the line laser scanner measurements correlate with the SPT measurements. Figure 2.8 shows an example of the pavement surface profile collected by the laser scanner. Within the developed algorithm, the surface profile is first divided into three segments. Then, a straight line is fitted to each segment using the least square method. The distances between the points and the corresponding line are calculated. This process is repeated for all the collected surface profiles. The MTD of the scanned pavement is equal to the average of all previously computed distances. However, as illustrated in Figure 2.8, the algorithm does not remove the slope from the collected data; hence, the calculated MTD is biased.

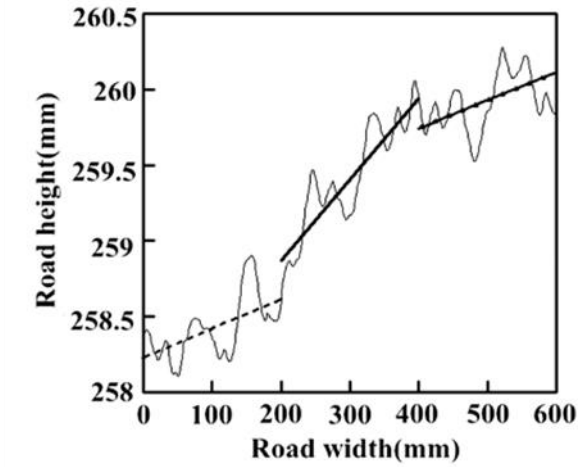

Figure 2.8: Schematic Representation of the MTD Calculation Method Developed by Hao et al., 2016.

AGGREGATE PROPERTIES AFFECTING PAVEMENT SKID RESISTANCE

Micro-texture is a critical component of pavement texture as well as a major contributing factor in roadway safety. Pavement microtexture refers to the small-scale irregularities imparted by the surface texture of the aggregates being used in the pavement (Hall et al., 2009). The texture of aggregates and their abrasion/polishing resistance affect directly on the level of skid resistance. In 2007, Asi performed friction tests on different pavement mixtures and concluded that mixtures constructed with harder aggregates present higher values of friction. A research study by Pelloli [42] on five different types of surfaces demonstrated that the association between the pavement skid resistance number and the water depth accumulated on the pavement surface depends on the amount of microtexture. Also, Horne in 1977 and Ong et al. in 2005 showed that it is possible to reduce the chance of vehicle skidding and hydroplaning in pavements with a good microtexture. Masad et al., (2007) found a close correlation between pavement skid resistance and aggregate texture properties.

Highway agencies must take careful consideration in selecting aggregates. Proper aggregate selection before surfacing helps in preserving adequate levels of texture and hence skid resistance over the service life of the pavements. Rough-surface-textured and hard aggregates must be used in surface pavement layers to provide an adequate level of surface microtexture and the resistant to polishing/abrasion of vehicle tires as well (*Mahone and Sherwood, 1995; Webb, 1970*). Dahir 1979, Abdul-Malak et al., 1996 and Crouch et al., 1996 stated that coarse aggregates at the surface are the primary source of surface texture for flexible pavements since they come into contact with the tires more than the fine aggregates do.

TxDOT's Wet Weather Accident Reduction Program (WWARP) establishes a method to ensure that pavements with high polishing resistance aggregates are constructed. In this method, depending on the frictional demand, aggregates are selected from the surface aggregate classification (SAC) system established by TxDOT's Construction Division (CST). Four tests are used in this program to examine the quality of the aggregates. The polishing resistance of aggregates is mainly categorized based on the results of the Micro-Deval and the Los Angeles Abrasion tests (Tex-410-A and Tex-461-A specifications). The Micro-Deval test consists of a rotating container with small steel balls in which aggregate particles are polished in the presence of water. In the Los Angles abrasion test, the aggregate particles are also polished in a rotating container by contacting with steel balls, except that their polishing resistance is measured in dry condition. The aggregates polishing strength is estimated by calculating their average mass loss after abrasion. The mass loss occurred in these two tests could be due to either abrasion or breakage. Thus, mass loss alone cannot correctly represent the abrasion resistance (*Chowdhury et al., 2017*). Two other tests, Soundness of Aggregates by Magnesium Sulfate and Acid-Insoluble Residue are also being conducted in addition to

Micro-Deval and Los Angles abrasion tests to examine the durability of aggregates. The soundness test is used to assess the resistance of an aggregate to the effects of freezing and thawing (*Jayawickrama, 1992*). The Acid-Insoluble Residue test determines the amount of noncarbonate material in aggregates. A large amount of noncarbonate material shows higher polishing resistance (*Kandhal and Bishara, 1992*). The latter has the shortcoming that all limestones will fail the test, even those harder limestone aggregates that could potentially offer good performance in terms of skid resistance.

By using Sac, highway engineers can select appropriate aggregate for pavement surfaces. The first SAC was developed in 1999 in which the aggregates were classified into four groups, A, B, C, and D. Class A are allocated to the groups of aggregates that show the best durability characteristics whereas class D represents aggregates with the worst characteristics. This classification system was based on the polishing value (PV) and magnesium sulfate soundness test results. The second version of SAC was developed in 2006 which classified aggregates based on the Acid Insoluble Residue (AIR) values, magnesium soundness loss (MSL), and polishing value (PV). Finally, in 2007, TxDOT revised the SAC classification and published the new version which is shown in Table 2.3 (*Masad et al., 2009*).

Property	Test Method	SAC A	SAC B	SAC C
Acid Insoluble Residue, % min	Tex-612-J	55		
5-Cycle Mg, % max	Tex-411-A	25	30	35
Crushed Faces, 2 or more, % min	Tex-460-A	85	85	85

Table 2.3: TxDOT's Surface Aggregate Classification (*Masad et al., 2009).*

As shown in Table 2.3, WWARP's aggregate selection system relies mainly on aggregate properties such as AIR, MSL, and crushed faces test results regardless of the importance of the surface texture. Due to the relationship between the aggregates surface texture and skid resistance, there is a need to modify the current aggregate classification system by using the indices that can reflect the texture properties of aggregates.

Measuring Aggregate Surface Texture

The significance of aggregate surface texture in tire/pavement friction can be dated back to the study performed by Knill in 1960. Nevertheless, so far, there has been no standard test procedure developed and use for measuring the surface irregularity of an aggregate particle. Most of the existing standard tests provide indirect measurements of aggregate surface texture. For example, standardized manual tests, such as ASTM Standard C 1252-03 and the AASHTOT P 56, measure the surface texture of aggregates by measuring uncompacted air voids or some highway agencies differentiate the aggregate surface texture by using the sense of touch. Both methods are labor intensive and subjective. Besides, no two observers will have the same opinion about the category of aggregates. To one inspector an aggregate particle may be fairly rough while to another it may be smooth.

The changes of aggregate surface texture due to polishing action have recently been quantitatively examined by the development of high-resolution devices and the ability to capture the micro-level of texture. In recent years, the use of image and laser scanning techniques for quantifying the texture properties of aggregates has gained increasing interest. Due to the availability of low-cost, powerful and fast processing software as well as signal and digital image processing techniques, various devices and techniques have been developed to measure the surface texture of aggregates directly. For

instance, Masad developed the Aggregate Imaging System (AIMS), which is capable of analyzing the texture properties of coarse and fine aggregates (*Masad, 2003*). It consisted of a camera, video microscope, lighting systems, aggregate tray, computer automated data acquisition system, and processing software. AIMS (shown in Figure 2.9) can capture an image of 640 × 480 pixels of 6–10 fine aggregate particles. For coarse aggregate, only one particle could be captured per image. The AIMS measure the texture of aggregate particles by analyzing grayscale images captured at the aggregate surface. The drawbacks of using the AIMS is that it is low resolution and only capable of taking 2D measurements and measuring texture using image-based analysis.

Imaging techniques are useful, but there are a few shortcomings such as being sensitive to picture quality and environment condition. In a research study, Wang et al., (2010) stated out that although visually discernable differences could be noted in particle texture before and after abrasion, these differences were not being satisfactorily identified through the image analysis processing based on optical images.

Laser-based scanning is another technique that has been developed for measuring aggregate texture properties. Kim et al., 2001 and Anochie-Boateng et al., 2011 have conducted several studies on the use of laser-based technologies to measure aggregate texture. The results of these studies showed that the laser could provide reliable and precise measurements. But the downside is that the laser scanner device developed by Anochie-Boateng et al. (shown in Figure 2.10) can only scan one aggregate particle at a time. Besides, the laser device scans with a 0.1 mm scanning resolution which is low for capturing the micro level of texture. As presented in Figure 2.11, the laser-based aggregate scanning system developed by Kim et al., (2001) is capable of scanning more than one aggregate. However, the resolution for the X, Y, and Z directions of the laser

scanner are 0.3 mm, 0.3 mm, and 0.5 mm, respectively which are not small enough to capture micro-texture.

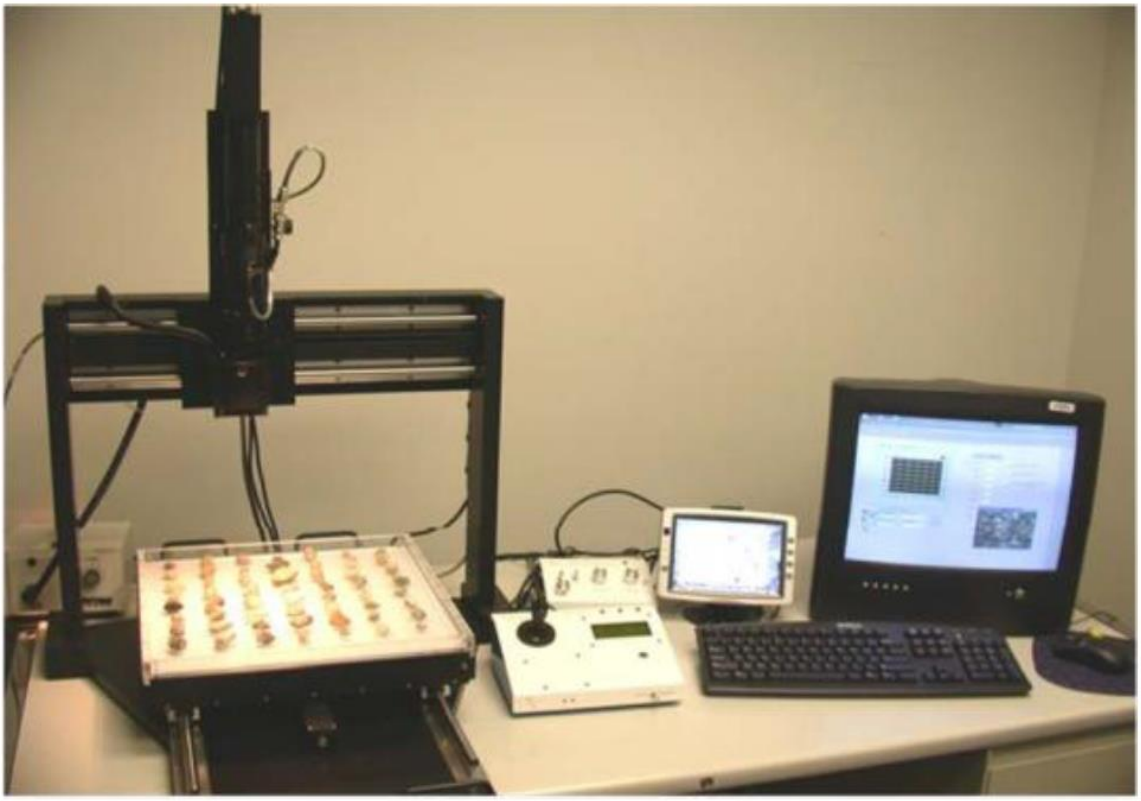

Figure 2.9: The Aggregate Imaging System Developed by Masad, 2003.

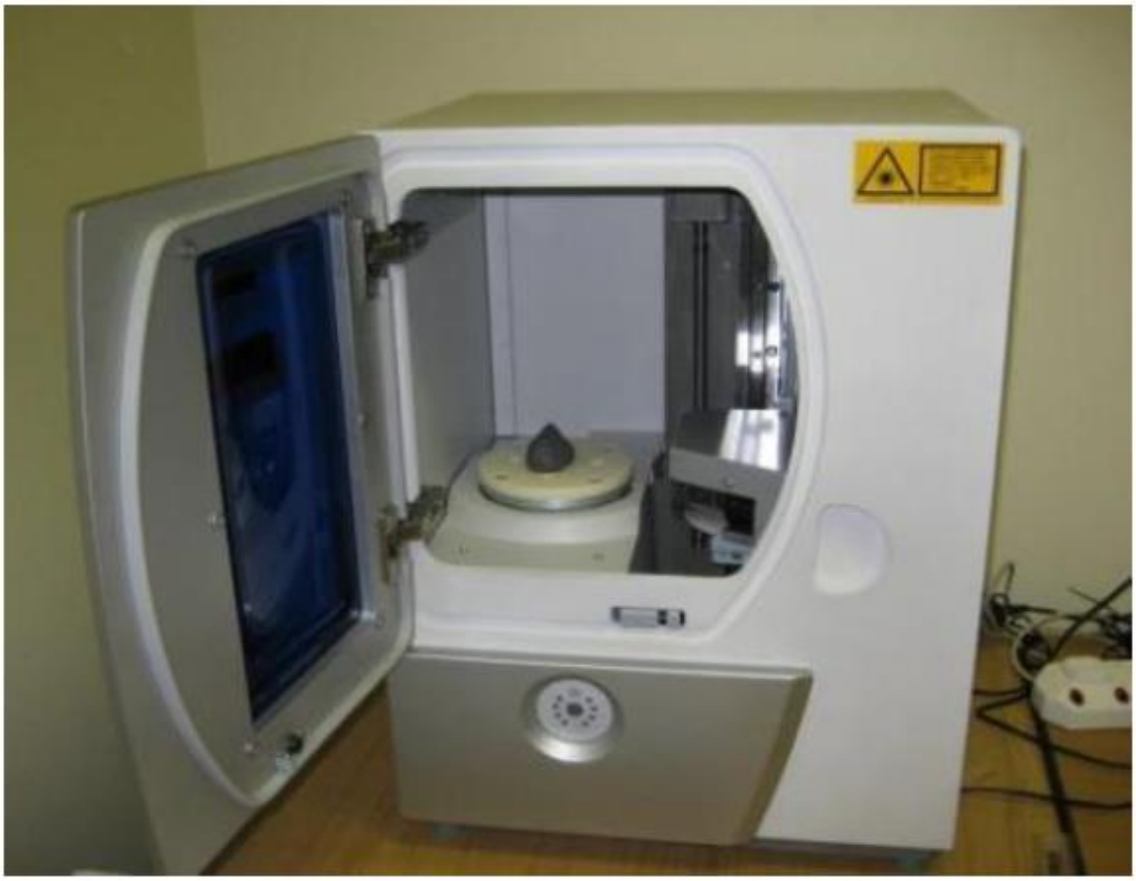

Figure 2.10: The 3D Laser Scanner Developed by Anochie-Boateng et al., 2011.

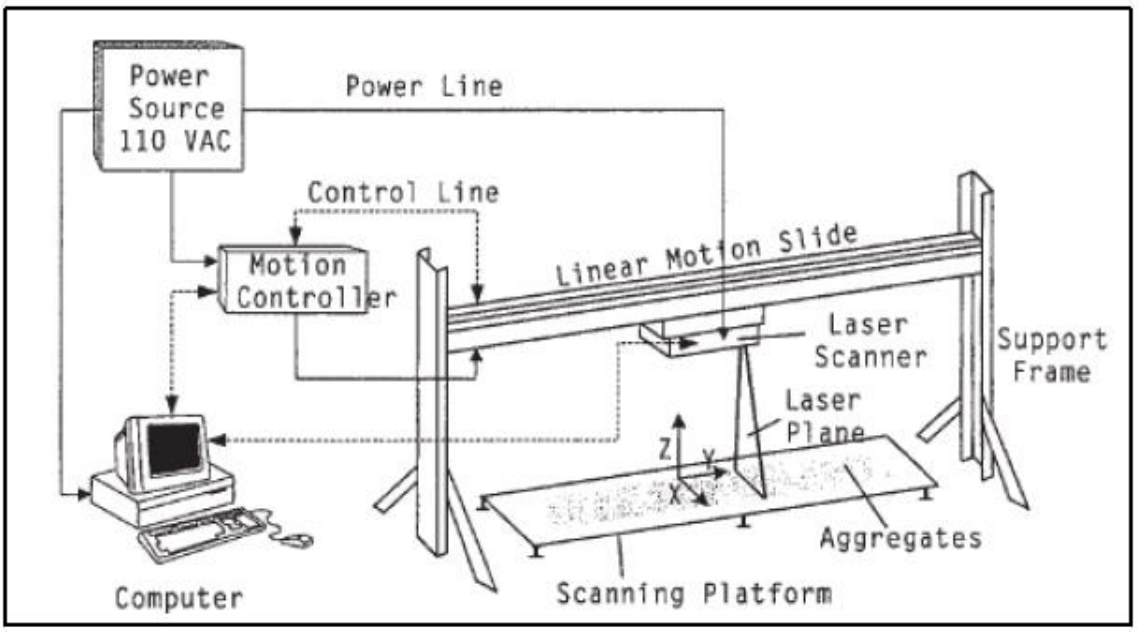

Figure 2.11: The Laser-based Aggregate Scanning System Developed by Kim et al., 2001.

CHARACTERIZING AGGREGATE SURFACE TEXTURE

Quantification of surfaces texture using height profiles is extensively used in surface engineering. The use of summary statistics is the base of texture characterization. Height parameters are mainly used to measure the surface texture owing to the role of the aggregate surface texture in tire/road friction (Do and Cerazo, 2015). Height parameters such as mean arithmetic deviation of a profile (Ra), root mean square roughness (Rq), and the depth of surface roughness (Rp) are statistical indicators obtained from the height profile of the aggregate's surface and found to have significant correlation with the British Pendulum Number, which is widely used to measure pavement surface friction (Cafiso and Taormina, 2007). These height parameters are calculated using the following equations:

$$\boldsymbol{Ra} = \frac{\mathbf{1}}{\boldsymbol{N}}\sum|\boldsymbol{Z_i} - \overline{\boldsymbol{Z}}| \qquad \textbf{Eq 2.2}$$

$$\boldsymbol{Rq} = \sqrt{\frac{\mathbf{1}}{\boldsymbol{N}}\sum(\boldsymbol{Z_i} - \overline{\boldsymbol{Z}})^{\mathbf{2}}} \qquad \textbf{Eq 2.3}$$

$$\boldsymbol{Rp} = \frac{\mathbf{1}}{\boldsymbol{N}}\sum_{\boldsymbol{i}}(\boldsymbol{Z_{max}} - \boldsymbol{Z_i}) \qquad \textbf{Eq 2.4}$$

where Z_i is the generic ordinate, $\bar{Z}$ is the average of Z_i values, Z_{max} is the maximum Z value, and N is the number of points.

Nataadmadja et al., 2015 showed that the curvature of asperities is also relevant to explain the evolution of roads' skid resistance under the polishing of traffics. According to this study, the curvature is calculated as shown by Equation 2.5.

$$\frac{\mathbf{1}}{\boldsymbol{r_i}} = \frac{\boldsymbol{z_{x-\Delta x,i} - 2.z_{x,i} + z_{x+\Delta x,i}}}{\boldsymbol{\Delta x^2}} \qquad \textbf{Eq 2.5}$$

where $z_{x,i}$ is the height value of asperity (i) located at abscissa x and Δx is the sampling interval of the profile.

Various mathematical-based approaches such as Fourier Transform (FT) and Power Spectral Density (PSD) have also been used to quantify surface texture. Fourier analysis provides an alternative representation of a height profile in which its frequency components can be observed and analyzed. Using the FT, the surface roughness power spectrum, or PSD, can be derived from the measured height profile which is the most critical parameter of randomly rough surfaces (*Persson, 2002; Persson, 2005; Persson, 2006*).

In 2005, Wang et al. implemented the Fourier analysis method to quantify the surface texture of aggregates, in order to then compare quantitative measurements with qualitative human-observation-based judgments. By applying FT, the profile of an aggregate is broken down to its harmonics of different frequencies. The results of this study demonstrated that harmonics with lower frequencies captures the shape of the

aggregate particle, and higher frequency components capture the texture. Researchers ranked and quantified ten different aggregates in terms of shape and surface texture. The results showed that the orientation of the aggregate particles in the profile images did not significantly affect the surface texture factors of those particles having similar size; however, the texture factors might be entirely different for the aggregates of different sieve size ranges (*Wang et al., 2005*).

Another study conducted by Slimane et al. in France sought to develop a new method to measure and characterize road surface micro-texture using image analysis. The power spectral density (PSD) of the high-frequency information obtained from surface cartography was studied. The PSD values were normalized, and the aggregate surfaces were compared considering the PSD's standard deviation. The researchers then successfully used a combined method of geometric and frequential criteria to find a meaningful relationship between friction values and roughness descriptions (*Slimane et al., 2008*). Researchers at the *Rheinisch-Westfälische Technische Hochschule* (RWTH) Aachen University in Germany (*Wang et al., 2017*) employed a high-resolution profilometer to collect the surface topography of the aggregate specimens. They used FT to convert the surface texture information of the aggregates to a spatial frequency domain in order to investigate the wearing behavior of the aggregates. Micro-Deval (MD) and Aachen Polishing Machine (APM) were utilized to polish the aggregates. The two-dimensional power spectral density (2D-PSD) was calculated before and after a polishing test to evaluate the surface texture and the texture changes. Comparing 2D-PSD values indicated that the polishing test affects surface texture only at very short wavelengths (below 62.8 micrometers).

FOURIER ANALYSIS

A signal is a function of an independent variable, usually time or space, and it is generally used to describe physical phenomena over time or distance (*Hsu, 1995; Oppenheim, 1998*). Signal processing is a mathematical and engineering process that was initially developed in electrical engineering, but it has become common outside of electrical engineering to extract the information embedded in signals. Sometimes, the time/spatial view of a signal might be challenging to understand. Transformation of that signal to the frequency domain helps to represent it in a different way exposing features that are not seeing in the space/time domain. The most important reason why the Fourier analysis is important in signal processing is that this approach shows what frequencies are included in a specific signal and in what proportions.

According to the Fourier theory, all signals, whether real or arbitrary, could be represented as the sum of sinusoidal waves of various amplitudes and frequencies. This approach helps to find the amplitudes corresponding to those sinusoids (*Yoo, 2001; Karrenberg, 2013*). Generally, Fourier analysis includes two parts: i) Fourier series, and ii) Fourier Transform (FT). The former decomposes a periodic function into the sum of sinusoidal functions, whereas the latter expands this theory to general functions that are not necessarily periodic (*Putman, 2007*).

This section explains the FT method by which non-periodic signals can be represented in the frequency domain. Figure 2.12 (a) shows a non-periodic finite wave that covers the time ranges between –T1 and T1 and is equal to zero outside of that range (*Hsu, 1995*). A periodic signal $x_{T_0}(t)$ (as shown in Figure 2.12) can be produced by repeating $x(t)$ with an arbitrary period of T0 such that $\lim_{T_{0\to\infty}} x_{T_0}(t) = x(t)$. The complex exponential FT representation of $x_{T_0}(t)$ is expressed as Equation 2.6.

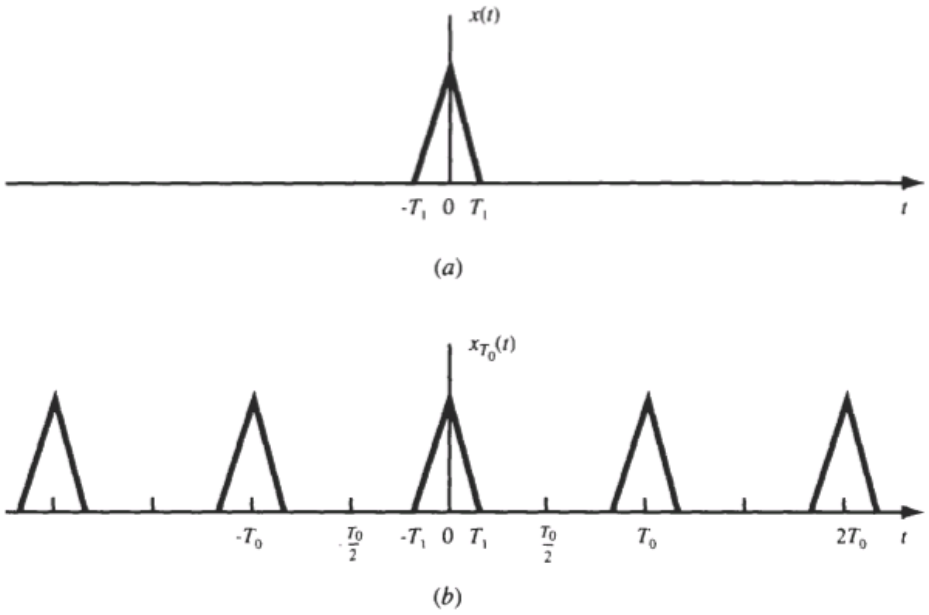

Figure 2.12 A Non-Periodic and (b) A Periodic Signal (*Hsu, 1995*).

$$x_{T_0}(t) = \sum_{k=-\infty}^{\infty} C_k e^{i2\pi(\frac{k}{T_0})t} \quad \textbf{Eq 2.6}$$

where T_0 is period, k only gets integers from $(-\infty, \infty)$, i is equal to $\sqrt{-1}$, and C_k is known as the Fourier coefficient and is calculated using Equation 2.7.

$$C_k = \frac{1}{T_0}\int_{\frac{-T_0}{2}}^{\frac{T_0}{2}} x(t) e^{-[2\pi i\left(\frac{k}{T_0}\right)t]} dt \quad \textbf{Eq. 2.7}$$

Since $x(t)$ is zero outside of (-T_1, T_1), the Fourier coefficient C_k for the non-periodic signal $x(t)$ can be rewritten as following:

$$C_k = \frac{1}{T_0}\int_{-\infty}^{\infty} x(t) e^{-[2\pi i\left(\frac{k}{T_0}\right)t]} dt \quad \textbf{Eq. 2.8}$$

Discrete Fourier Transforms (DFT)

Most of the real phenomena, such as the surface of aggregates, can be modeled by analog signals, but they cannot be analyzed using digital computers. To store and process analog signals using computers, they need to be converted to digital signals (*Baraniuk, 2009*). A digital signal is a set of discrete samples picked from a continuous signal at a given sampling interval (*Hsu, 1995)*. The proper sampling interval is dictated by the largest frequency or the smallest period of interest (*Olshausen, 2000*).

Consider a discrete function $x(t)$ with *N* points at an interval of $\Delta T = 1$. Therefore, we have a discrete function, $x[n]$, with the length of $N\Delta T = N$ and a finite number of samples. Discrete Fourier series (DFT) is the FT of this sampled function that transforms *N* discrete points of the signal to the *N* equally spaced discrete frequencies.

Using the inverse and forward DFT, we can transform a given function from the time domain to the frequency domain and vice versa. In the case where we have $x[n]$, forward DFT provides the Fourier coefficients C_k. When we have the Fourier coefficients C_k we can find the *N* values of $x(t)$ using inverse DFT (*Orfanidis, 1995; Oppenheim, 2009*). Equations 2.9 and 2.10 show the inverse and forward DFT formulations.

$$\boldsymbol{x[n] = \sum_{k=0}^{N-1} C_k e^{2\pi i \frac{k}{N} n}} \qquad \textbf{Eq 2.9}$$

where *N* is the number of samples and *n* = [0, 1, …, N-1].

$$\boldsymbol{C_k = \frac{1}{N} \sum_{k=0}^{N-1} x[n] e^{[-2\pi i \left(\frac{k}{N}\right) n]}} \qquad \textbf{Eq 2.10}$$

Normally, forward and inverse DFT are accomplished using effective computational algorithms: FFT and Inverse FFT. For this study, these algorithms were implemented in MATLAB.

Power Spectral Density (PSD)

Power spectral density (PSD) is an analysis in the frequency domain that provides the power associated with constituent frequencies (or spatial frequencies) of a signal (Elson, 1995; Benbow, 2006). The PSD of a signal x(t) can be calculated using the following equation:

$$\boldsymbol{PSD = \frac{1}{N}\sum_{k=0}^{N-1}|C_k|^2} \qquad \textbf{Eq 2.11}$$

where *N* is the total number of Fourier frequencies and C_k is the Fourier coefficients of the signal $x(t)$.

Parsvel's theorem states that the average power in one period of a signal is equal to the sum of the square of absolute value of Fourier coefficients. Equation 2.12 shows the Parsvel relationship for a periodic signal $x(t)$ (*Oppenheim, 1998*).

$$\boldsymbol{\frac{1}{T}\int_{over\ T}|x(t)|^2 dt = \sum|C_k|^2} \qquad \textbf{Eq 2.12}$$

where *T* is the period.

Accordingly, the average power of a signal over one period is equal to the sum of the power over Fourier components of that signal. PSD gives the power of the signal $x(t)$ and shows how much energy of the signal $x(t)$ has at a particular frequency.

Chapter 3: Evaluation of the LLS Performance Through Laboratory Measurements

INTRODUCTION

In this chapter, the process for the development of a three-dimensional (3D) non-contact line laser scanner (LLS) prototype at the University of Texas at Austin is presented. The description of the main components of the LLS, design of the prototype, and the system operations are also included in this chapter. This laser scanner was used to scan pavement surfaces and aggregate particles, to collect the 3D surface data from them, and measure their texture properties. In this chapter, the laboratory investigations and data processing performed to overcome the signal noise and filter of outliers in the scanned data are explained in detail.

LASER SCANNER PROTOTYPE COMPONENTS

Figure 3.1 (a) presents the schematic view of the LLS prototype. This prototype consists of two major components: 1) a 2D non-contact laser sensor and 2) a linear translation stage. The LLS projects a blue light having a wavelength of 405 nm in a horizontal line. Generally, the line laser scanners available in the market work based on two different light colors: blue and red. The superiority of blue light over red light is its smaller wavelength, which results in less error and higher precision. The light is emitted from the LLS and a detector captures the reflection of the light from the scanned surface. The angle between the emitted light and the captured reflection is known by the calibrated laser. Using triangulation principles (Figure 3.1 (b)), changes in the height due to the texture irregularities along the laser line can be measured.

Some sections of this chapter were previously published in Kouchaki et al., "Characterization of Aggregate Texture and Correlation with Surface Skid Resistance," Report No. FHWA/TX-17/0-6878-3, 2018. The author of this dissertation contributed to this published report by collecting and analyzing the data and preparing the manuscript.

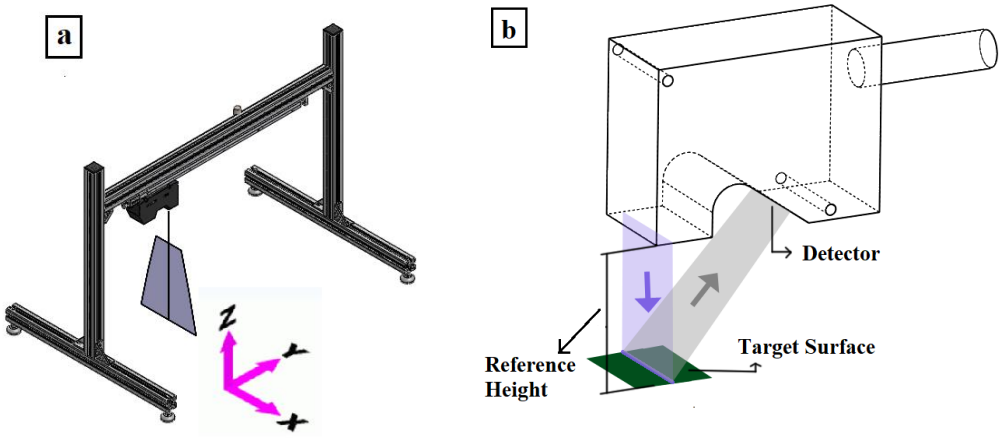

Figure 3.1: a) 3D Schematic View of the Developed LLS Prototype, b) Triangulation System of the LLS.

The triangulation technique is used to find the height of the scanned object. Figure 3.2 (a) demonstrates the setup of the camera and the laser sensor. As can be seen in this figure, the laser is placed perpendicularly to the surface with a distance of 'h.' But the camera is angled toward the surface with and angle of 'θ' with the horizontal axis and a distance of 'l' from the surface. The height (h) is calculated using the following equation:

$$\boldsymbol{h = l * tan(\theta)} \qquad \textbf{Eq 3.1}$$

Figure 3.2 (b) shows that the height of the object 'h_{obj}' from the surface is lower than 'h' which is the distance from the laser to the surface. The following equation is used for measuring the height of the object:

$$\boldsymbol{\alpha = arctan(\Delta X / f)} \qquad \textbf{Eq 3.2}$$

$$\boldsymbol{m = l * tan(\theta - \alpha)}$$

$$\boldsymbol{\Delta h = h - m = l * (tan(\theta) - tan(\theta - \alpha))}$$

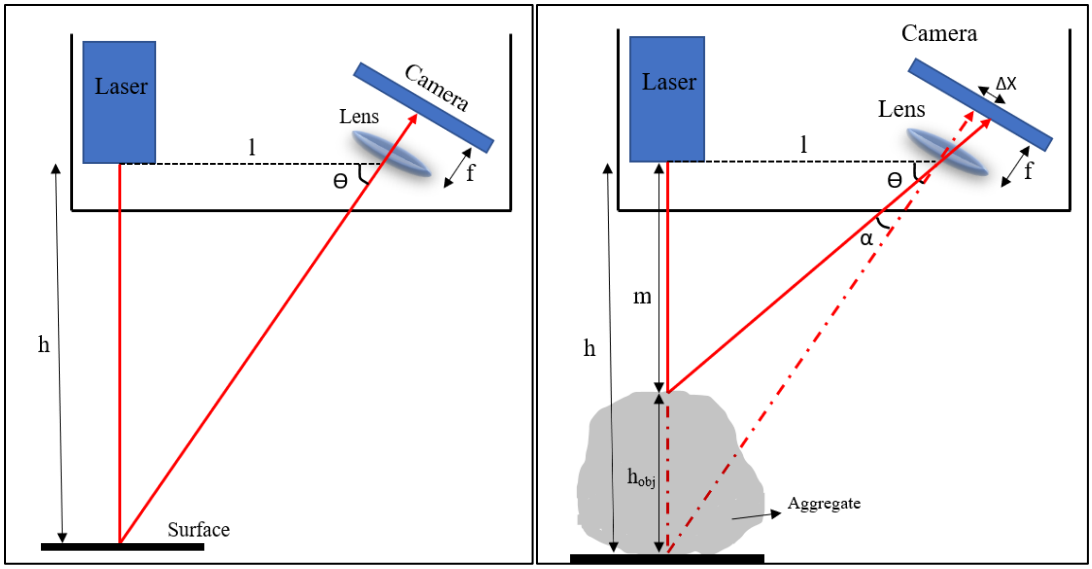

Figure 3.2: (a) Laser Triangulation Geometry and (b) Laser Triangulation Geometry in the Presence of an Object (*Ashok et al., 2015*).

The LLS was mounted on a linear translation stage to travel over the surface and scan it. The developed LLS prototype is capable of collecting a maximum of 800 points in the transverse direction (X-direction) and a maximum of 15,000 points in the longitudinal direction (Y-direction). At each point, the LLS captures the relative height of that point, in millimeters (Z-direction). Combining the discrete height values captured in Y or X-direction provides height profiles. Therefore, the LLS is able to capture the maximum 800 or 15000 parallel height profiles in Y or X-direction, respectively. While 800 points along the X-direction are captured at once and independent of time, the measurement along Y-direction depends on the speed of the scan and the frequency of the measurements. Both the linear translation stage and the laser are connected to a computer, and the scanned data are collected there in an Excel file. Each row of the Excel file contains the scanned data in X-direction, and each column contains the scanned data in Y-direction.

Based on the scope of this study, two different laser sensors were used: LLS – 80 and LLS – 300. The specifications of the two laser sensors are provided in Table 3.1. This section presents the mechanism of the LLS – 80 to understand the basic functioning principles and capabilities of the system. However, it should be noted that the same experimental tests were performed with the LLS – 300..

Model			**LLS - 80**	**LLS - 300**
Installation Condition			Diffuse reflection	
Reference Distance			80 mm	300 mm
Measurement Range	Z axis (Height)		±23 mm	±145 mm
	X axis (Width)	Near side	25 mm	110 mm
		Reference distance	32 mm	180 mm
		Far side	39 mm	240 mm
Light Source			Blue semiconductor laser	
	Wavelength		405 nm (Visible light)	
	Laser Class		Class 2	
	Output		4.8 mW	
Spot Shape (Reference distance)			Approx. 48 mm x 48 µm	Approx. 240 mm x 610 µm
Repeatability	Z axis (Height)		0.5 µm	5 µm
	X axis (Width)		10 µm	60 µm
Linearity	Z axis (Height)		±0.1% of F.S.	±0.05% to ±0.15% of F.S.
Profile data Interval	X axis (Width)		50 µm	300 µm
Sampling Frequency			Max. 16 µs (High-speed mode) Max. 32 µs (Advanced function mode)	
Environment resistance	Operating ambient luminance		Incandescent lamp: 10000 lx or less	
	Operating ambient temperature		0 to +45 °C	
	Operating ambient humidity		20 to 85% RH (No condensation)	
	Vibration resistance		10 to 57 Hz double amplitude 1.5 mm; 3 hrs in X, Y and Z directions	
Material			Aluminum	
Mass			Approx. 400 g	Approx. 1000 g

Table 3.1: Lasers Data Sheet (*KEYENCE, 2017).*

According to the LLS – 80 manufacturer's instruction (*Keyence, 2017*), the reference distance in the Z-direction, which is the vertical distance between the laser and the object (Figure 3.3), is 80 mm. The target should be close to the reference distance and within the measurement range of ±23 mm in Z-direction to achieve an acceptable measurement. On the other hand, the measurement range in X-direction depends on the vertical distance of the target from the laser so that the closer distance to the laser, the narrower the measurement range in X-direction. As depicted in Figure 3.3, the measurement range in X-direction is 25 mm at the near side, 32 mm at the reference distance, and 39 mm at the far side.

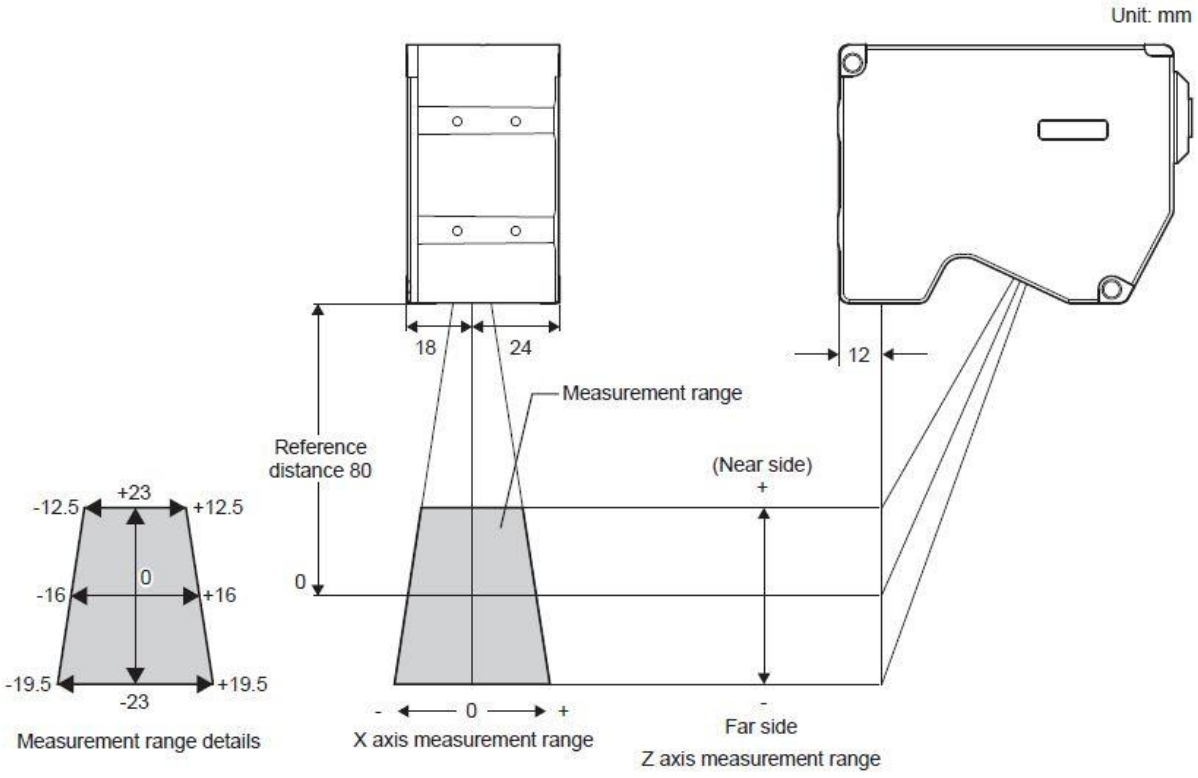

Figure 3.3 The LLS Measurement Range in X and Z-direction (*KEYENCE, 2017*).

LABORATORY INVESTIGATIONS AND DATA PROCESSING

Correcting for Tilt

It is ideal to have a leveled surface for the measurement in order to minimize scan errors. However, in some cases, the presence of laser line tilt in X-direction is inevitable due to the slope in the existing surface or the laser head, hence, tilt correction is required. This correction can be done automatically through the LLS software. In addition, before the data processing, the slope line of the scanned surface in Y-direction must be leveled to diminish the errors in the future calculations.

Filtering out Outliers

After scanning an object via the LLS, the points with extremely low values of -99.9999 mm, called negative dropouts, were observed at the two sides of the scan along with X-direction. Experiments to understand the negative dropouts at the edges of scans were performed. The experiment led to an understanding of the number of dropouts observed as a result of different heights. As provided in Figure 3.4, when the laser head was fixed at the height of 60 mm from the surface being measured, the number of dropouts increases. Therefore, the X-direction had approximately 220 negative dropouts. When the laser head was fixed at its reference height of 80 mm, the number of dropouts were at approximately 95-100 points. Finally, the laser head was fixed at 100 mm and it was found that there were no dropouts and the scan line was at its full 800 points in the X-direction. The results showed that an algorithm within the laser controller adds dropouts to the profiles based on the height. The closer the laser head is to the surface, the more dropouts there are and the less of the scan line. The opposite is true for when the laser is at approximately 100 mm: it has no dropouts, and the full scan area can be used.

This is done to keep the distance between two consecutive points in the X-direction constant, i.e., 50 microns.

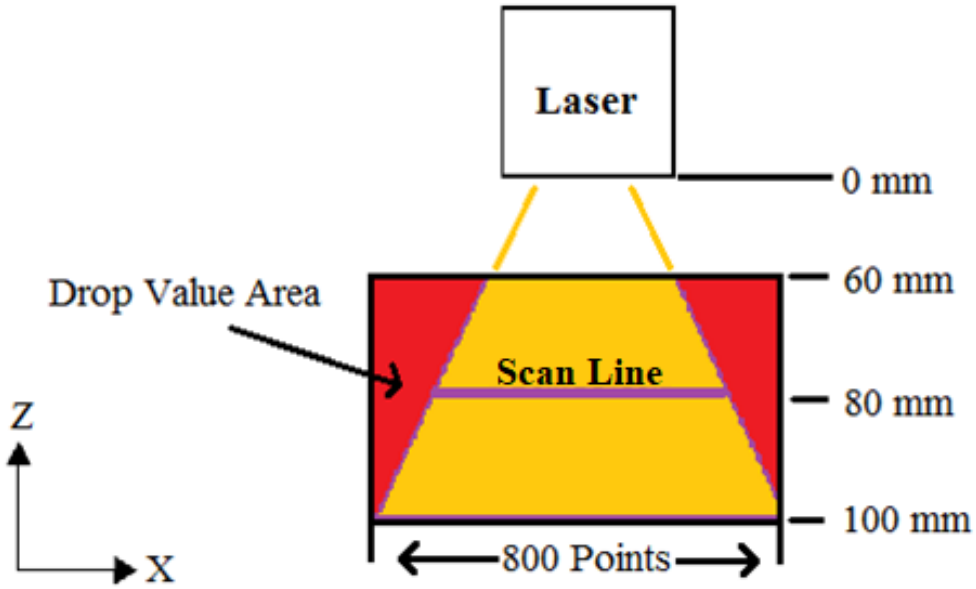

Figure 3.4: Schematic of the laser's scan area.

Scanning Interval

The focus of this study was to capture the surface texture of pavements and aggregates at two levels: macrotexture and microtexture. As explained earlier in this dissertation, macrotexture refers to the features of the surface with the wavelengths between 0.5 and 50 mm and the microtexture consists of the surface features with the wavelengths less than 0.5 mm. Three ranges of wavelength were considered in this study: 1) the second decade of microtexture (0.005 mm < λ < 0.05 mm), 2) the first decade of microtexture (0.05 mm < λ < 0.5 mm), and 3) the first decade of macrotexture (0.5 mm < λ < 5 mm). Based on Shannon theorem (Nyquist theorem) the interval between scanning

points must be equal to half of the smallest wavelength of interest. Accordingly, in order to capture the second decade of micro, the scanning interval should be equal to 2.5 microns. Since the scanning interval in X-direction (Δx) is 50 microns, microtexture cannot be captured in this direction. As mentioned before, the scan interval along the Y-direction *(*Δy) is dependent on the speed of scan (v) and the frequency of sampling (*f*); hence, different scanning intervals can be obtained by adjusting these two parameters in the LLS. Equation 3.3 presents how the scanning interval are obtained considering the sampling frequency and speed. For instance, by setting the frequency at 1 kHz and the moving speed at 2.5 mm/s, the scanning interval would be 2.5 microns and the first decade of the microtexture could be captured.

$$\Delta y = \frac{v}{f} \qquad \textbf{Eq 3.3}$$

where

Δy: Scanning resolution in Y direction (mm)
v: moving speed (mm/s)
f: scanning frequency (Hz)

REPEATABILITY OF THE SCANS IN Y DIRECTION

The LLS specification provides the repeatability in X and Z-direction of 10 and 0.5 microns, respectively. The repeatability of the developed prototype in Y-direction is required to ensure the accuracy of the measurements. The surface of an object was scanned five times in Y-direction to check the repeatability of the LLS and the reliability of the captured data. The repetitive scanning was performed under the same conditions without moving the developed LLS prototype or the object. The height profile located in the middle of each scanned data was selected in the five scans. As an example, a profile captured in Y-direction is depicted in Figure 3.5. The horizontal axis in these figures

represents the number of points that were scanned in Y-direction with scanning interval of 2.5 microns and the vertical axis shows the height values. To study the repeatability, the standard deviation of five profiles was calculated and plotted along Y-direction below the height profile in Figure 3.5. According to this figure, at all scanned points the standard deviation of five height values was greater than 5 microns. In addition, higher standard deviations were observed within the areas in which the longitudinal profile was steep. Therefore, it can be concluded that, despite manufacturer specifications, the laser measurements were not reliable in the second decade of the microtexture. Therefore, the second decade of microtexture was excluded from the study and the rest of the study focused on the first decade of micro- and macro-texture, which is above 50 microns. Accordingly, the scan speed and frequency were adjusted to obtain the scanning interval of 25 microns.

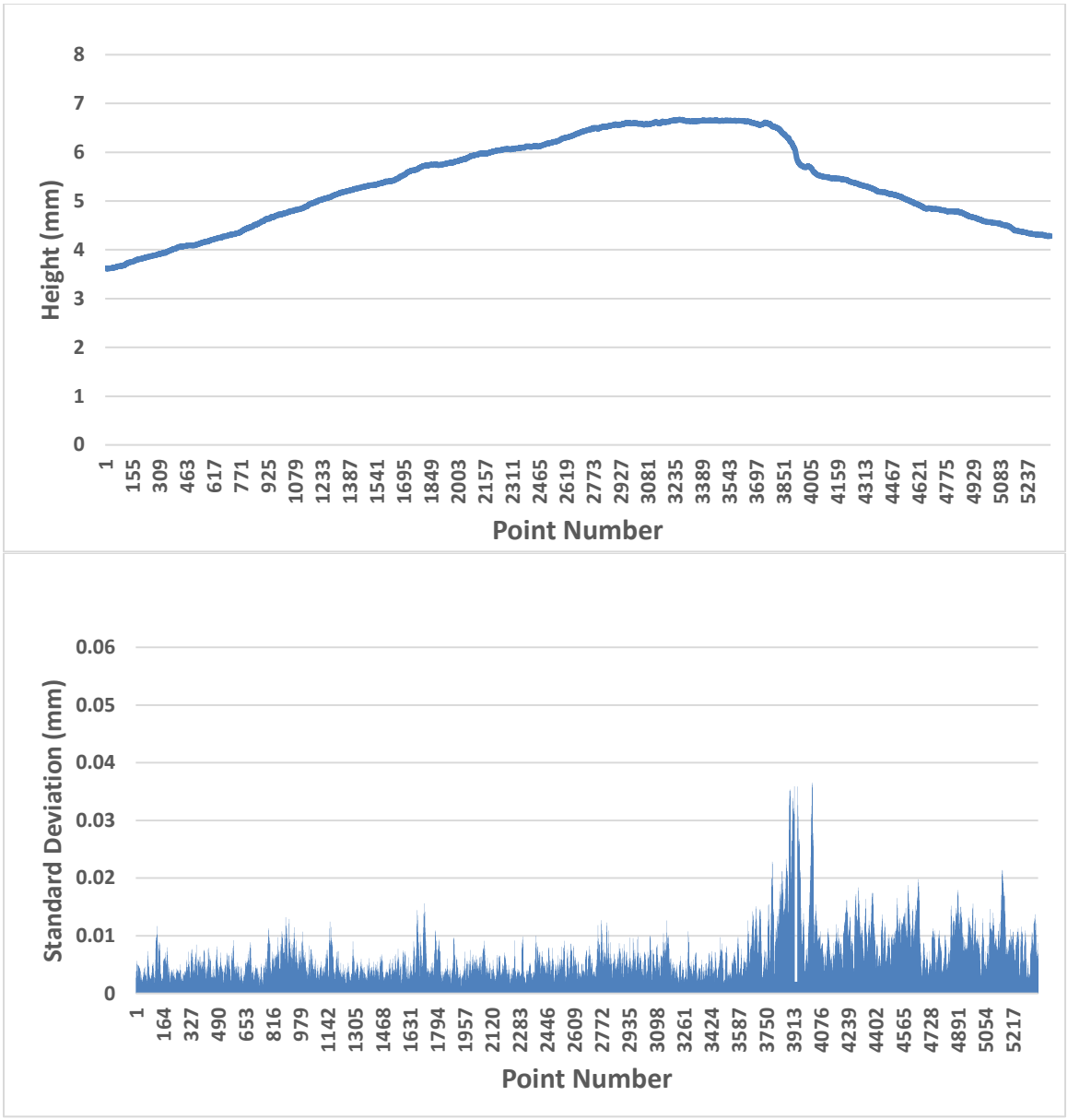

Figure 3.5: Height profile of aggregate along y-direction (top), and corresponding standard deviation (bottom).

SCANNING AGGREGATE PARTICLE VIA LLS

Figure 3.6 (a) presents the 3D scan of an aggregate particle captured by the LLS prototype. The negative dropouts described in the section of "Filtering out Outliers" can

be seen on the two sides of the scan. To remove these errors from the analysis, fifty columns in each edge need to be trimmed out from the data. Thus, the final scan data (as presented in Figure 3.6 (a)) consists of 700 points in each row. During the scan, there exist limitations that arise from the nature of the measurement. The dark areas in Figure 3.6 (a) are the missing data in which the laser was not able to detect the laser line reflected from the aggregate surface specifically at the edges of the aggregate particle. The X-Y view of the scan is also provided in Figure 3.6 (b) to see these dark areas around the aggregate better. Several factors such as background color, glossiness, ambient light, scanner settings, etc. might affect the quality of the scanned data and the size of the dark area. Accordingly, several laboratory experiments were conducted to study the influence of these factors on the scanned data.

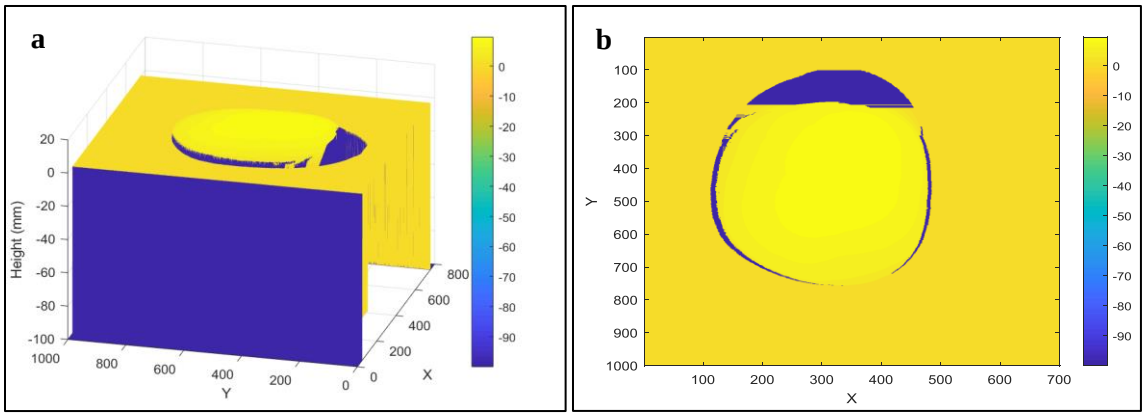

Figure 3.6: (a) 3D Scan of an Aggregate Particle Captured by the LLS Prototype, (b) X-Y View of the Scan of the Aggregate.

The Effect of the Background Color and Ambient Light

To understand how the LLS works, a basic explanation is given as to how semiconductor lasers emit light. To start, a diode consists of two semiconductors that are

either n-type or p-type. The semiconductor is doped with atoms that have different electron configuration. For an n-type, the atoms are doped with allowance for extra electrons to flow freely, as there is one extra electron in the outermost energy level. The p-type is doped with an element that has a 'hole,' lacking an electron in the outermost energy level. When the two materials, or semiconductors, are combined into a diode, electrons flow to the holes and vice versa. An electrical power source is used to continue this interchange of holes and electrons with the use of current. At the junction of the semiconductors, photons are released as the electrons combine with the hole. The wavelength is dependent on the semiconductor material; the different materials can have different energies from the electron-hole interaction, and the photon energy is inversely proportional to wavelength (*Hecht, 2008*).

The spectral range of light is presented in Figure 3.7. For the case of the LLS, the photon has a 405-nm wavelength which is in the visible spectrum of light, and it is seen as the color violet/blue to the human eye. The violet light is emitted from the LLS, and then the reflection of the light from a given surface is captured by a detector. In order to evaluate the effect of background color on the accuracy of laser measurement, different background colors were used beneath the aggregate particle (as depicted in Figure 3.8) and tests were performed.

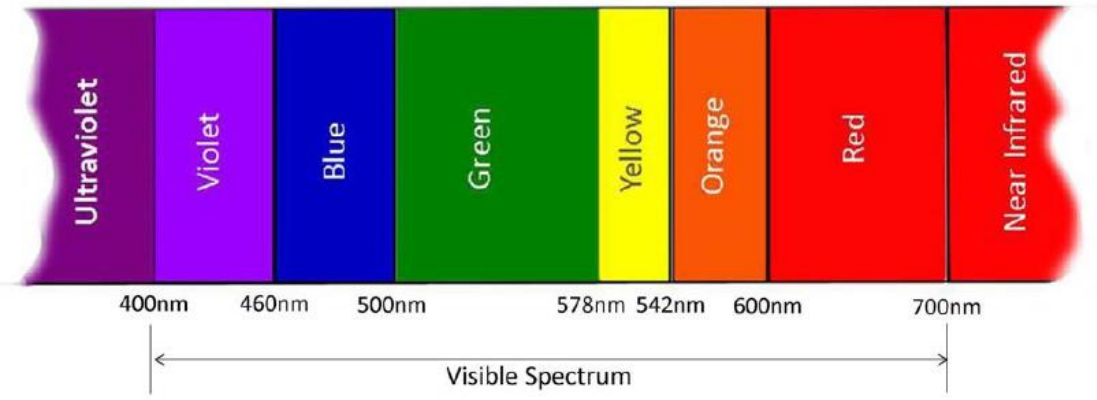

Figure 3.7: Spectral range of light.

The measurements were compared to each other with respect to the number of dropouts that occurred for each color paper used in the test. The results showed that the effect of the background color is negligible on the data measured by the laser. This might be due to the short wavelength of the LLS photon, which is violet, compared to the other colors. In addition, in order to perceive how the scanning results differ by changing the intensity of external lights, an aggregate particle was placed on a selected background and scanned twice; in a bright room and a dark room with a covering box on the laser. Other conditions were kept the same for both tests. The number of dropouts compared the tests. It was found that the laser scans are not affected by the room light.

Figure 3.8: Using Different Background Colors in Measurement.

Adjusting the Settings of the LLS Software

The LLS software offers several features to deal with the negative dropouts during the scanning. The software offers three interpolation modes including no interpolation, linear interpolation, and vertical interpolation. Figure 3.9 depicts how profile changes by choosing the different interpolation modes. In each scan, one of these modes was selected to find how the interpolation feature influences the measurement. Several tests were performed to get a better understanding of the effect of these features on the measurement. It turned out that using either the linear interpolation mode or vertical interpolation mode some parts of the dropouts at the edges of the scanned particle were fixed. For instance, Figure 3.10 depicts an X-Y view of an aggregate scan developed by applying the linear interpolation mode.

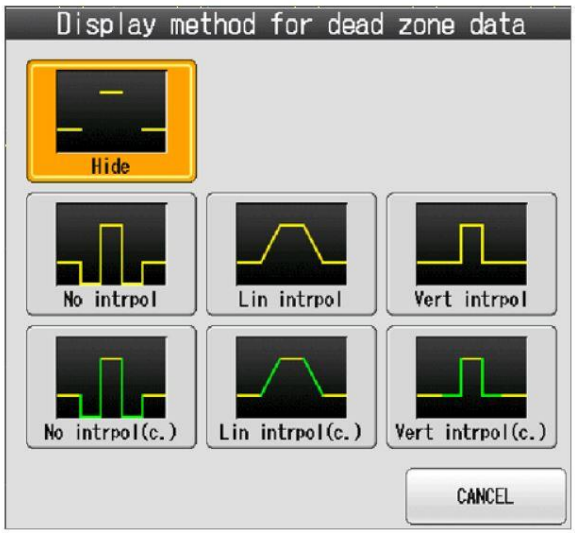

Figure 3.9: Three Interpolation Modes in the LLS Software (*KEYENCE, 2017).*

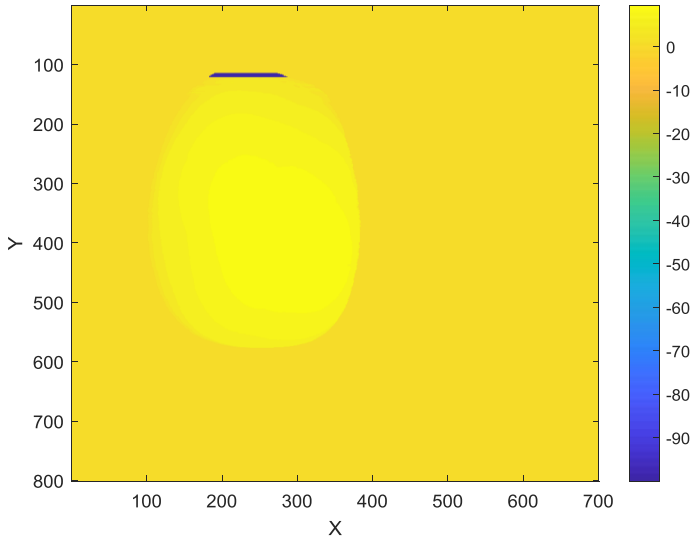

Figure 3.10: X-Y View of the Scanned Aggregate by Applying the Linear Interpolation Mode.

As can be seen in Figure 3.10, the dark area is still visible at the beginning of the scan. At this time, an aggregate particle was placed in the scanning area of the laser and scanned in two different directions, from left to right (Figure 3.11 (a)) and then from right to left (Figure 3.12 (b)), to see whether the direction of scanning affects the dark area. Figures 3.11 (b) and 3.11 (d) illustrates the X-Y view of the scanned aggregate. The result obtained from these two tests is that the dark area (undetectable parts by the laser) occurred at the same location in two scans. Therefore, it was established that the performance of the laser is similar in both directions.

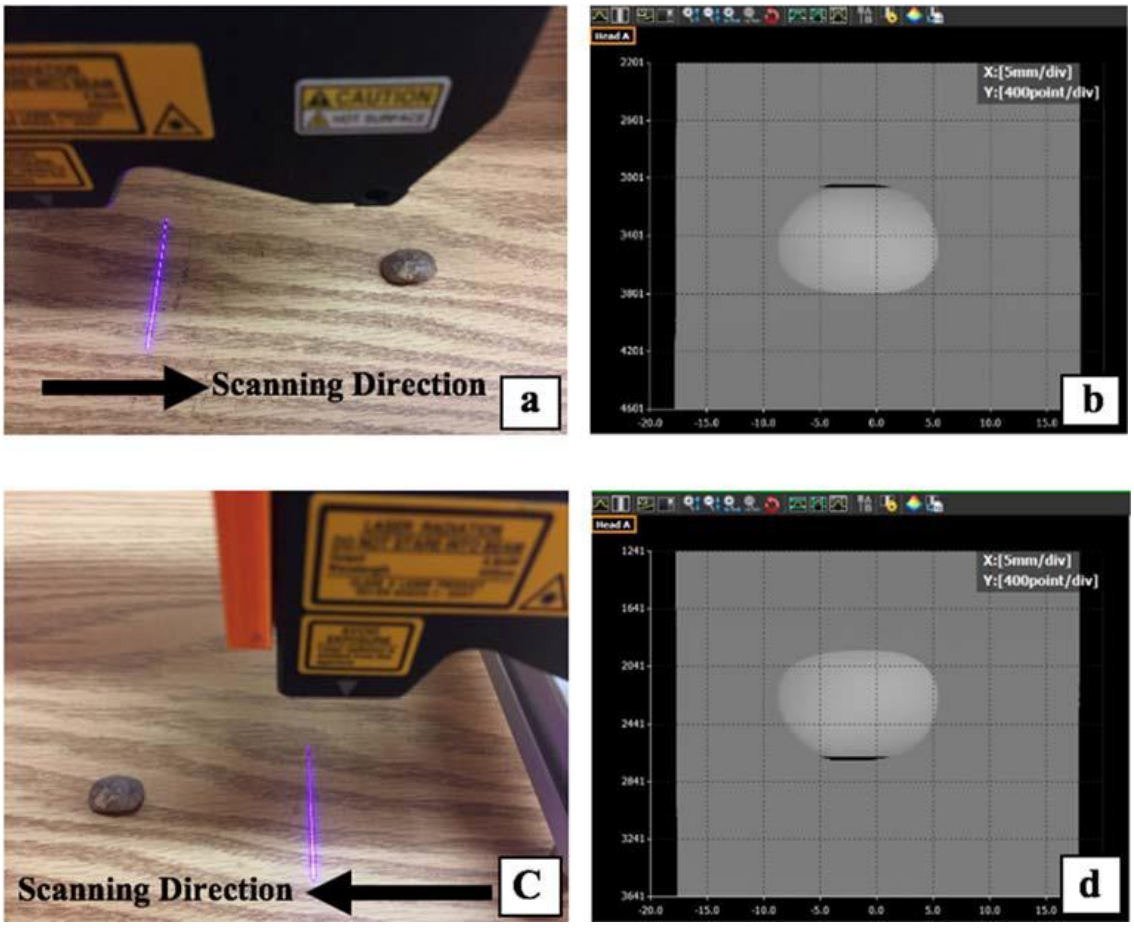

Figure 3.11: a) Scanning an Aggregate from Left to Right, b) X-Y View of the Scanned Aggregate, c) Scanning an Aggregate from Right to Left, d) X-Y View of the Scanned Aggregate.

Combining Two Scanned Data

The dark area is minimal and does not have a significant effect on the study of the surface texture, but when the shape properties of an aggregate are evaluated, a perfect scan of the aggregate particle is required. To overcome the dark area, two scans were performed on an aggregate so that the aggregate was rotated 180 degrees in each scan. Then, the scanned data were merged using a code developed in MATLAB. For this purpose, a metal plate was built, as shown in Figure 3.12, and the aggregate was glued to

the plate. After the first scan, the plate was rotated 180 degrees and scanned from the other direction.

It should be noted that after rotation, the plate was kept in the same location to reduce additional noise in the measurements. This allowed the reconstruction of the 3D scan using the superposition of the subsequent measurements. In order to merge the two datasets, the data of the second scan was rotated 180 degrees. The similar parts of the two scans were determined, and then the two datasets were overlaid. Figure 3.12 illustrates the two scans and the merged one.

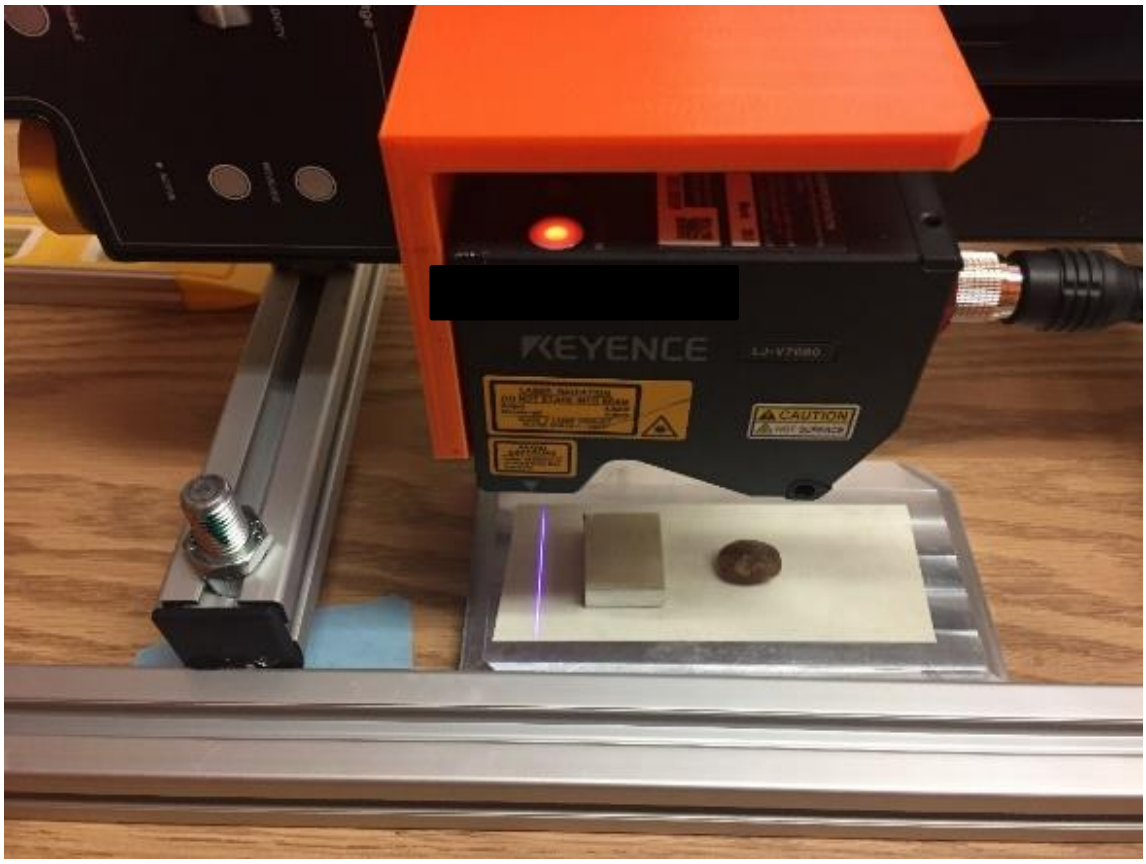

Figure 3.11: Metal Plate.

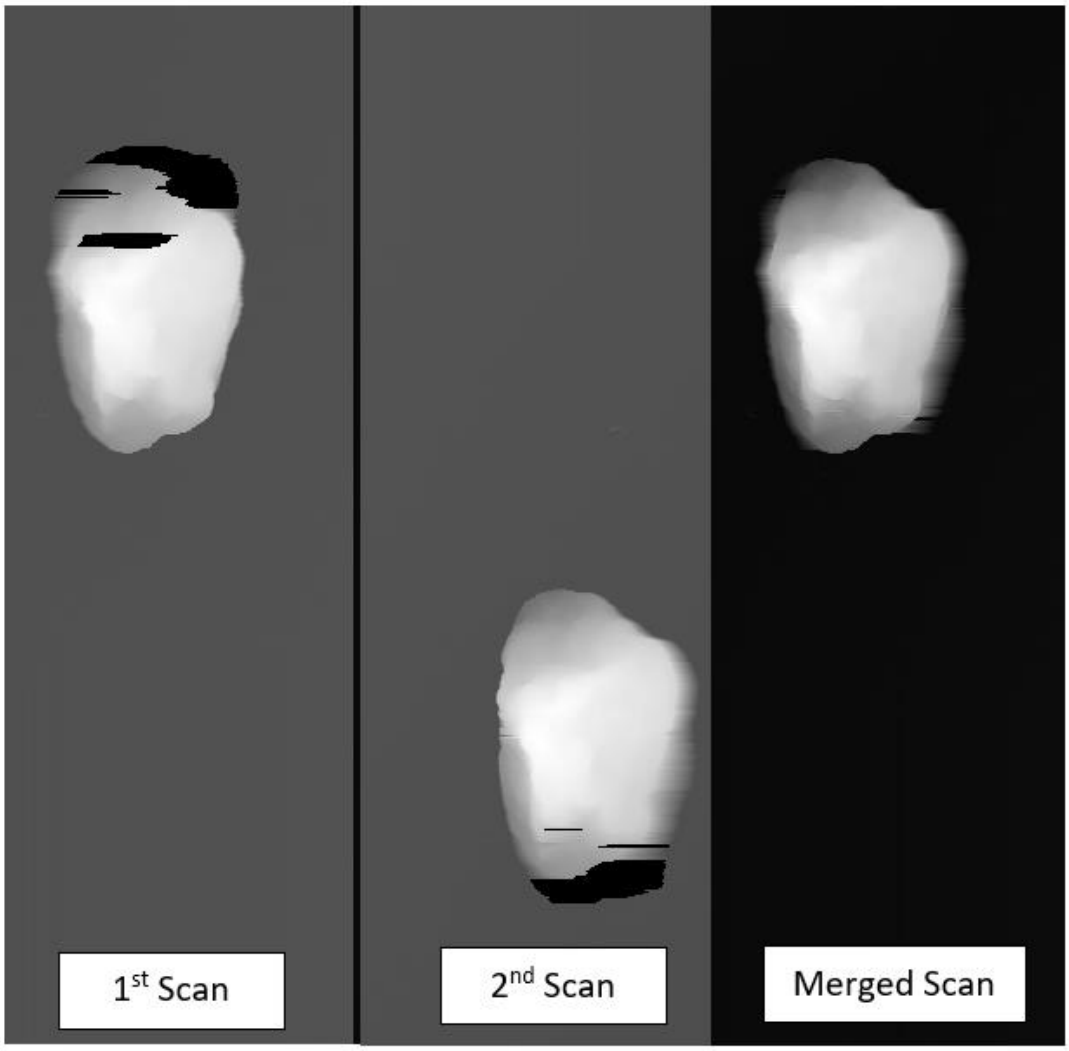

Figure 3.12: Black and White Image of the First Scan, Second Scan and the Merged Scan.

SCANNING PAVEMENT SURFACES VIA LLS

One of the objectives of this study was to scan in-service pavement sections to measure their surface texture. As provided in the LLS manual, the maximum illuminance resistance is 10,000 lux. The illuminance is used as the intensity of light that hit a surface. An illuminance of 10,000 lux corresponds to a full daylight with a non-direct sun which

means that the laser should not be exposed to a direct sun. Accordingly, during the field measurement, direct sunlight could affect the measurement of the laser, since the illuminance can exceed the maximum resistance. Therefore, for all the measurements taken in the field from pavement surfaces, a covering box was required.

In some cases, the raw scanned data collected by the LLS were contaminated by outliers not belonging to the scanned surface. These outliers may be caused by reflective surfaces, surfaces with high voids, and the failure of the camera to receive the reflected laser beam. These invalid data make measurements inaccurate and cause erroneous calculated texture values. Consequently, identifying and fixing these errors is vital in order to get precise measurements. The data preprocessing steps are detailed in this section by providing an example of a pavement surface scan contaminated by outliers:

Step 1: The data gathered by the LLS is imported into MATLAB. Figure 3.13 (a) illustrates a raw scan data collected by the LLS on a pavement surface.

Step 2: As explained in the section of "Filtering out Outliers," there are always dropouts at the edges of the scans collected by the LLS. These dropouts always have a fixed value and can be easily recognized. These invalid data points need to be trimmed out from the two sides of the scan data.

Step 3: As can be seen in Figure 3.13 (b), dropouts also exist within the data. These dropouts are detected based on the measuring range of the LLS. For instance, the measuring range of the LLS - 300 (as presented in Table 3.1) is from -145 mm to 145 mm meaning that every point with a height value less than -145 mm is a dropout. Once the dropouts are found, the Neighborhood Averaging Filter (NAF) is applied. This filter was developed in MATLAB within the scope of this study. NAF is a sliding window filter which only replaces a dropout with the average value of neighboring pixels,

excluding itself and other dropouts. This filtering continues until the number of dropouts reaches zero.

Step 4: In this step, the data (shown in Figure 3.13 (c)) should be detrended to eliminate the slope of the height profiles in the Y-direction. The detrended data is depicted in Figure 3.13 (d).

Step 5: The other type of outliers that occurs in the scanning data is the presence of the impulsive noise (or spikes). For instance, Figure 3.13 (e) shows one sample height profile of the scan data. Spikes are shown in this plot with a red circle around them. Spikes were noted all over this scan data. A median filter was used to eliminate these spikes. This filter is another sliding window filter that moves over the scan, considers each data point in the scan in turn, and replaces the data point being considered with the median of neighboring data points. The median is calculated by sorting all the data points within the window. A seven by seven pixel window was used in this study to apply the median filter.

At each LLS scan on an asphalt pavement surface, steps 1 through 5 are required to obtain a 3D model relevant to the pavement surface. Ignoring these steps while creating the 3D model of the pavement surface could result in the miscalculation of the texture. Figure 3.13 (f) illustrates the clean 3D model of the selected pavement section.

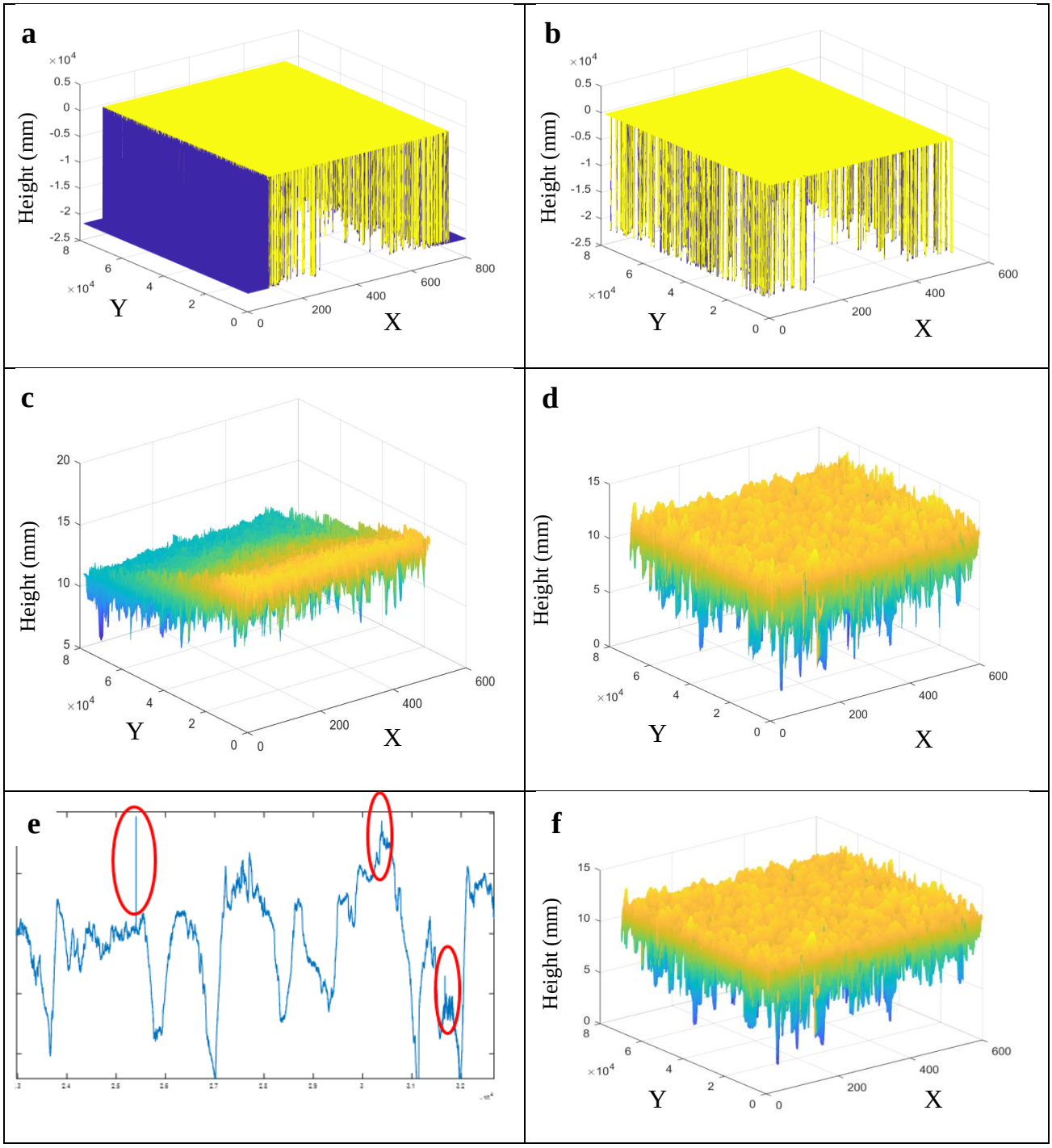

Figure 3.13: Illustration of the Filtering Process

Chapter 4: Field Investigation of Relationship between Pavement Surface Texture and Friction

INTRODUCTION

Understanding the texture-friction relationship is valuable for transportation agencies and engineers for proper pavement maintenance and better design of pavement, especially when higher skid resistance is needed. A few studies have been conducted in this regard, but the effects of pavement texture on the friction produced at the pavement surface are still not fully understood. The primary goal of this section is to find the correlation between field-measured texture and friction data. For this purpose, a process consisting of the following steps was followed:

- Use the LLSP to collect texture data,
- Develop an automatic algorithm to calculate the MPD values of texture data,
- Evaluate the LLSP's performance by comparing its results to those of the CTM,
- Use the Grip-Tester to collect continuous friction data at traffic speed, and
- Perform statistical analysis to establish correlations between texture and friction.

FIELD-DATA COLLECTION

Test sections and pavement types

Three test sections, each more than five years old, were selected. Each section had established measurement data for the CTM and LLS. The sections chosen provided a variety of mix designs, ensuring variation of surface texture for the test. The test sections are located in Bastrop, Bryan, and Fort Worth in Texas:

- Bastrop:
    - Mix design: Porous Friction Course (PFC)

A paper based on this chapter was published: Kouchaki et al., "Field Investigation of Relationship between Pavement Surface Texture and Friction," Journal of Transportation Research board, vol. 2672, p. 395-407, 2018. The author of this dissertation contributed to this published article by designing the research methodology, collecting and analyzing the data, and preparing the manuscript.

    - Average annual daily traffic (AADT): 13,972
- Bryan:
    - Mix design: Dense-Graded Type C
    - AADT: 5,843
- Fort Worth:
    - Mix design: Dense-Graded Type D
    - AADT: 57,385

At each location, six samples were taken: three in the right wheel path and three in the center of the lane, with a 12.5 m (41 ft) distance between the locations (Figure 4.1). To maintain consistency in the surface measurements, the LLS was placed in the same locations used for the CTM. Note, however, that these devices operate differently due to the mechanism of motion in each: the CTM measures in a circle and the LLS measures linearly. For the CTM, eight segments of 111.5 mm (4.39 in.) arcs are scanned by a point laser, which results in a full circle. Among the segments, as depicted in Figure 4.2, two of them are parallel to the direction of traffic. To ensure an equivalent comparison with the CTM's measurements, the LLS was configured to scan a 120 mm (4.72 in.) length. The area scanned by the LLS (shown in Figure 4.2) was the same as the two segments of the CTM that were parallel to the direction of traffic.

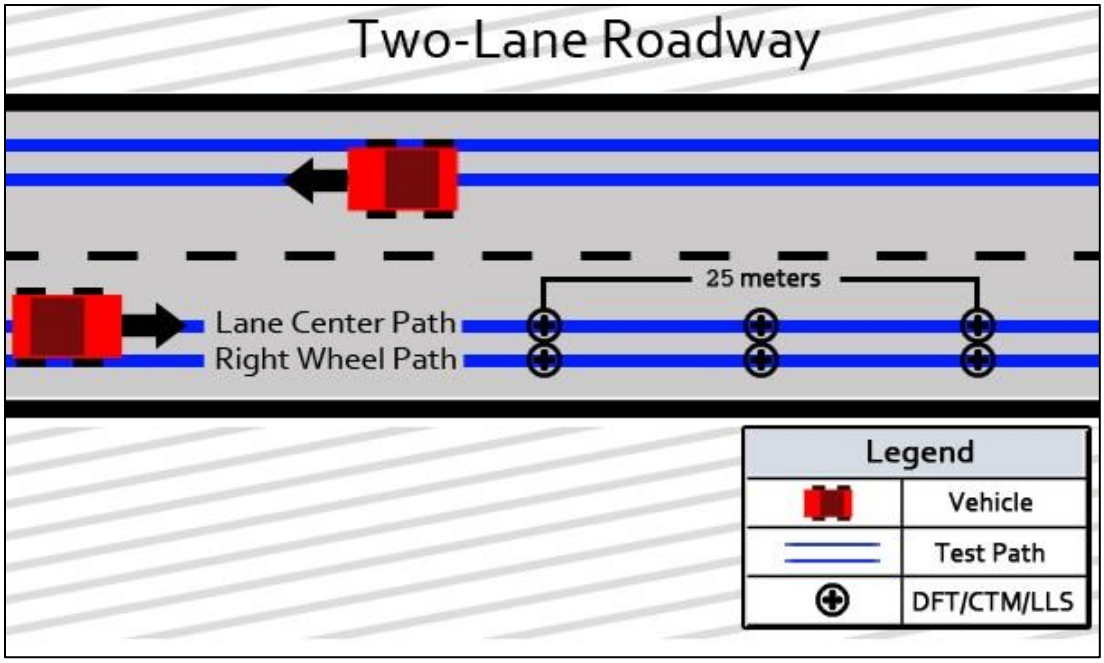

Figure 4.1: Illustration of test section and test location.

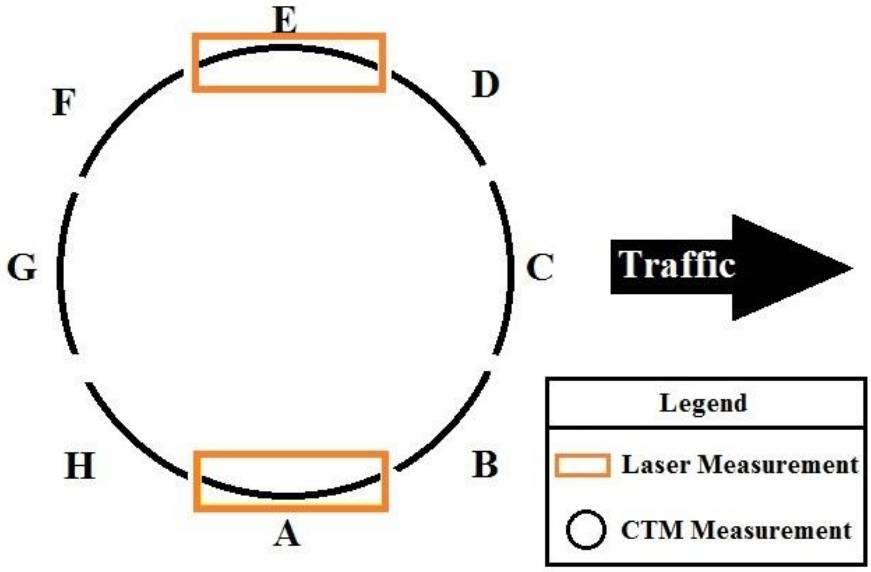

Figure 4.2 The scanned areas by the CTM and the LLS.

To measure friction, the Grip-Tester was selected because of its wider range of testing speeds, better repeatability and reproducibility (depending on the operating speed), greater efficiency in water usage, and commercial availability *(Andriejauskas et al., 2014)*. The Grip-Tester is a friction-measuring trailer that uses a fixed slip wheel to simulate anti-lock braking on a wet road surface. This is achieved by the Grip-Tester having three wheels: two have patterned treads and are connected by a drive axle, while the third is a smooth tread tire. The drive axle, connecting the two drive wheels, has a 27-tooth sprocket; it is connected by a transmission chain to the measuring wheel that has a 32-tooth sprocket *(Thomas, 2008)*. The difference in sprocket teeth creates a 15% continuous slippage on the measurement tire. To create wet road conditions, a watering system supplies a constant water thickness specified by the user to the measuring wheel.

The axle connecting the measuring wheel outputs the dynamic friction by using strain gages to measure the horizontal drag force and vertical load force. The information is used to estimate the Grip Number (GN), or coefficient of friction, in real-time *(Thomas, 2008)*. As shown in Equation 4.1, the GN is the ratio between the fraction of tractive drag force (F_d) and the load force (Q).

$$\boldsymbol{GN = \frac{F_d}{Q}} \qquad \textbf{Eq 4.1}$$

The Grip-Tester (Figure 4.3) needs a vehicle capable of towing the trailer as well as a water tank to supply water to the measuring wheel. The Grip-tester measurement consisted of two target speeds (50 and 70 km/h) to evaluate the dependency of speed on friction. The speed needs to be maintained within 5% of the target speed.

Figure 4.3: The Grip-Tester attached to a vehicle.

RESULTS AND DISCUSSIONS

MPD Calculation from the LLS Data

After scanning the pavement surfaces, the same filtering procedure, as explained in Chapter 3, was followed to remove the dropouts and the spikes. Afterward, Fourier transform was applied to convert the texture profiles, those collected in the Y-direction, from the space domain to frequency (or wavelength) domain. Figure 4.4 (a) provides a sample of captured surface profiles. The FT plot of this profile is presented in Figure 4.4 (b). In addition to macro-texture, the obtained texture profile includes the wavelengths that are lower than 0.5 mm (microtexture). In order to obtain a measure of macrotexture, the texture profile was passed through a low-pass filter. Using this filter all the frequencies above 2 (cycles/mm) (wavelength lower than 0.5 mm) were rejected to isolate the macrotexture components (as shown in Figure 4.4 (c)). Figure 4.4 (d) shows the plot of the original texture profile along with its macrotexture profile.

In the next step, the MPD was calculated followed by ASTM E1845 for all filtered profiles captured in a pavement section and then the median of the results was reported as the estimation of the MPD of the pavement section.

For the MPD calculation, the first step consisted of correcting for the inclination slope of the height profile. Thus, a regression line was calculated and then subtracted from the height profile and so the initial profile will be converted to a zero-mean profile. As a second step (Figure 4.5), the height profile was divided into two segments with the length of L/2 for which the maximum height is detected. By using Equation 4.2, MPD is calculated as the average of the two determined maximum heights.

$$MPD = \frac{Max\ Height\ of\ 1st\ Segment + Max\ Height\ of\ 2nd\ Segment}{2} \qquad \textbf{Eq 4.2}$$

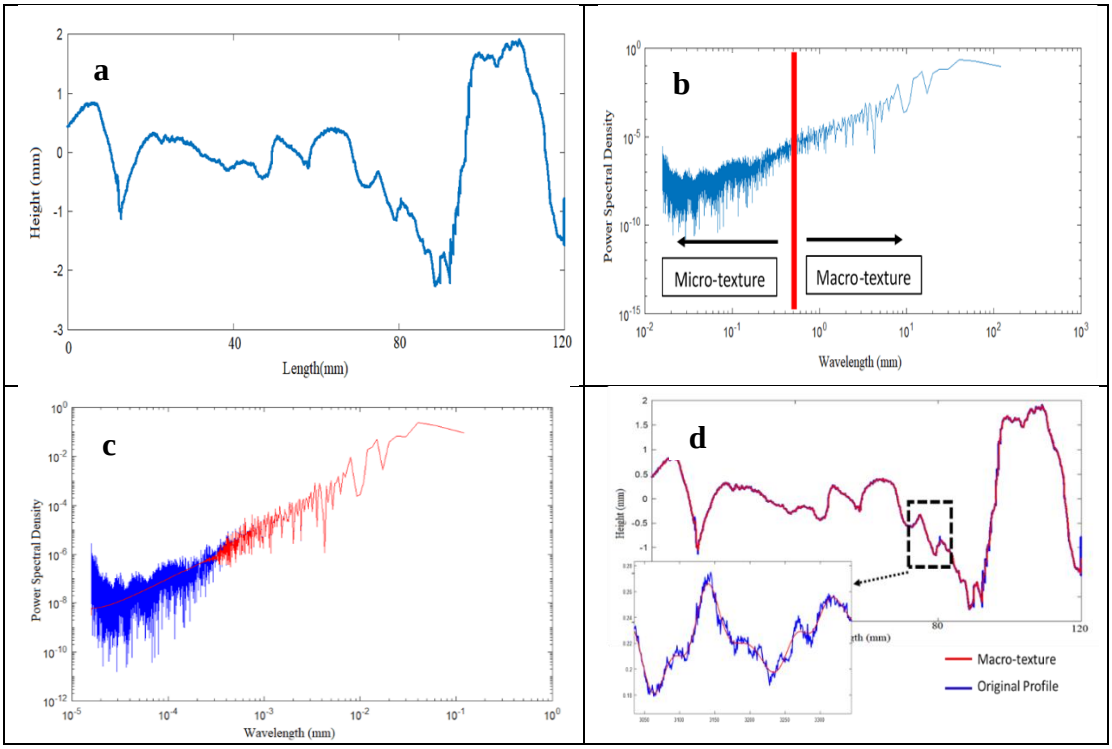

Figure 4.4: a) A surface profile captured by the LLS, b) PSD of the surface profile, c) PSD of the macro-texture components, and d) Macro-texture profile along with the original profile.

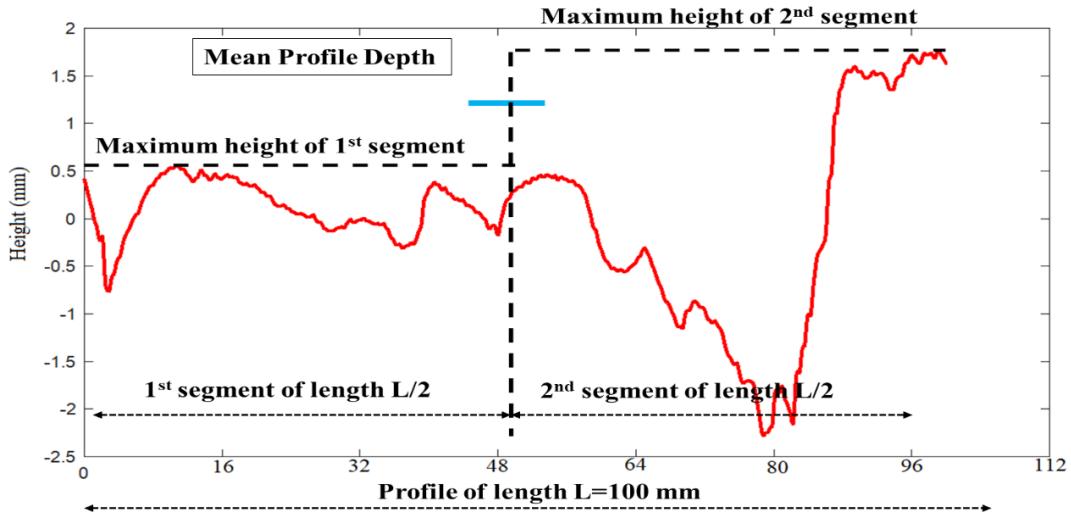

Figure 4.5: Graphical illustration of MPD calculation.

Repeatability of LLS

The LLS results were compared to those from the CTM for both segments A and E, which were shown in Figure 4.2, to investigate the repeatability and reliability of the developed LLS prototype. The MPD, as a surface characteristic, was calculated for all test locations. Then, single values of MPD for the right wheel path and the center were obtained by averaging the three respective samples. This was done for both LLS and CTM as graphed in Figures 4.6 (a) and 4.6 (b): the "R" and "C" represent the right wheel path and center lane path, respectively. As this figure illustrates, the MPD values obtained by the LLS, denoted as *MPD-by-LLS*, are very close to the MPD values of CTM, denoted as *MPD-by-CTM*. There were no observable biases between the MPD values with which to draw a general conclusion.

Repeatability of the developed LLS prototype was evaluated by calculating the average and standard deviation of three MPD-by-LLS and MPD-by-CTM values obtained at each test section from their respective test paths. Then, the standard deviation of each group of data was compared. For example, the three MPD-by-LLS values for the pavement surface under the right wheel path at the Bryan test section were compared to each other with respect to their standard deviation. Due to the short distance between test locations, similar texture characteristics were expected at those locations. As Figure 4.6 (c) indicates, for the segment A, the standard deviations of MPD-by-LLS data were significantly lower than MPD-by-CTM in the entire test sections. Similarly, Figure 4.6 (d) shows that the standard deviations of MPD-by-LLS data, obtained from segment E, were notably lower in three test sections (Bastrop-C, Bastrop-R, and Bryan-R). Comparable MPD values were observed at the rest of the sections. According to these

results, it can be concluded that the developed LLS prototype is capable of providing an accurate and precise measurement of the pavement surface texture.

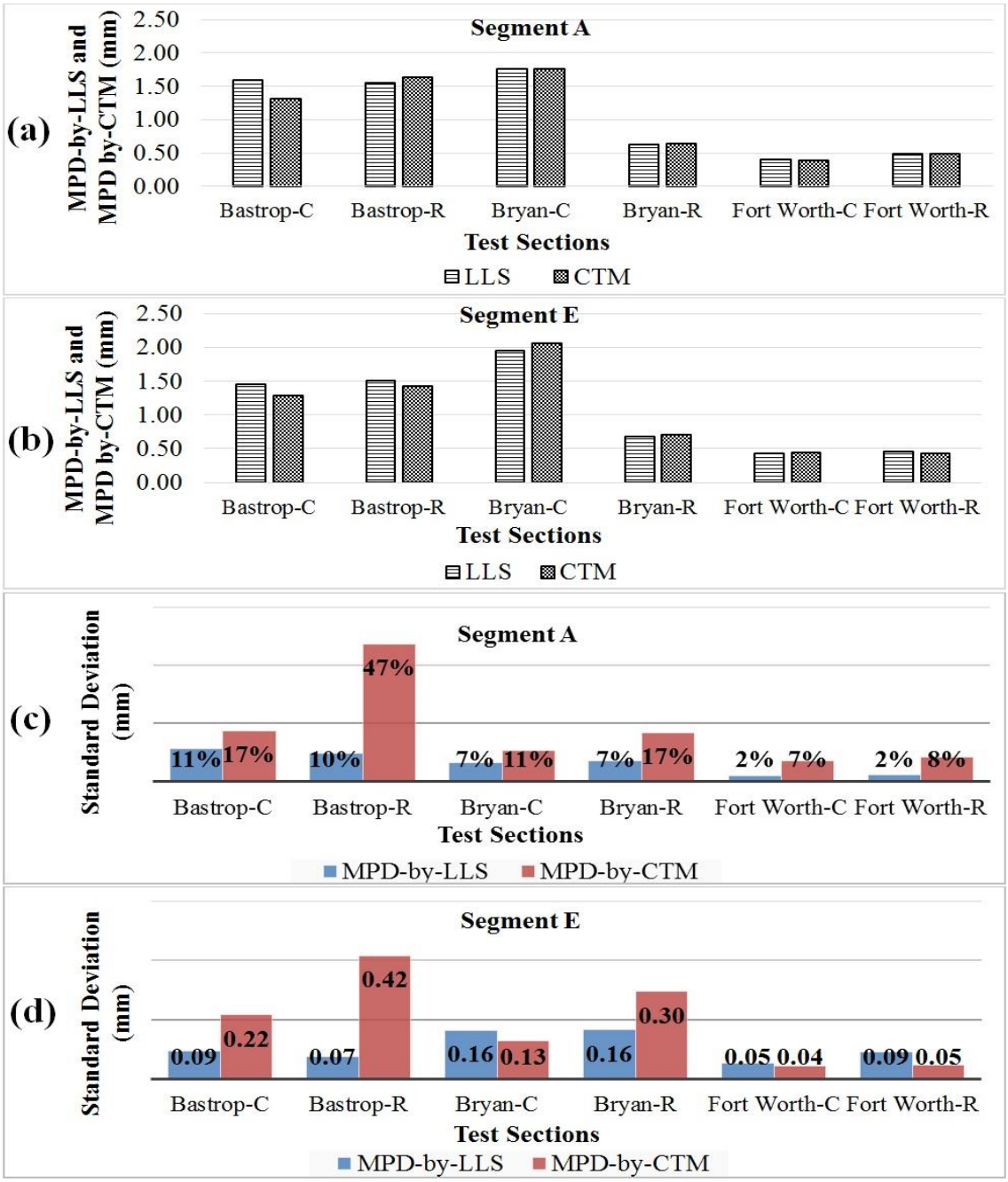

Figure 4.6: Parts a and b show the comparison of mean MPD values obtained from developed LLS prototype and CTM in segments A and E respectively; Parts c and d show the standard deviation of MPD values measured by developed LLS prototype and CTM at six test sections in segments A and E respectively.

Grip-Tester Results

Based on the literature, there is no a unique and consistent speed specified by agencies to perform the friction test. Hence, understanding the effect of speed on GN, would help researchers and practitioners interpret the friction results in different cases when the test speed is variable. The results, plotted in Figure 4.7, show that, as expected by the theory, the GN decreased when the speed increased. This finding is reasonable but contrasts with the results of a study conducted at the University of Auckland by Wilson et al. in 2013, in which they stated that at speeds less than 75 km/h, the GN may not be affected by test speed.

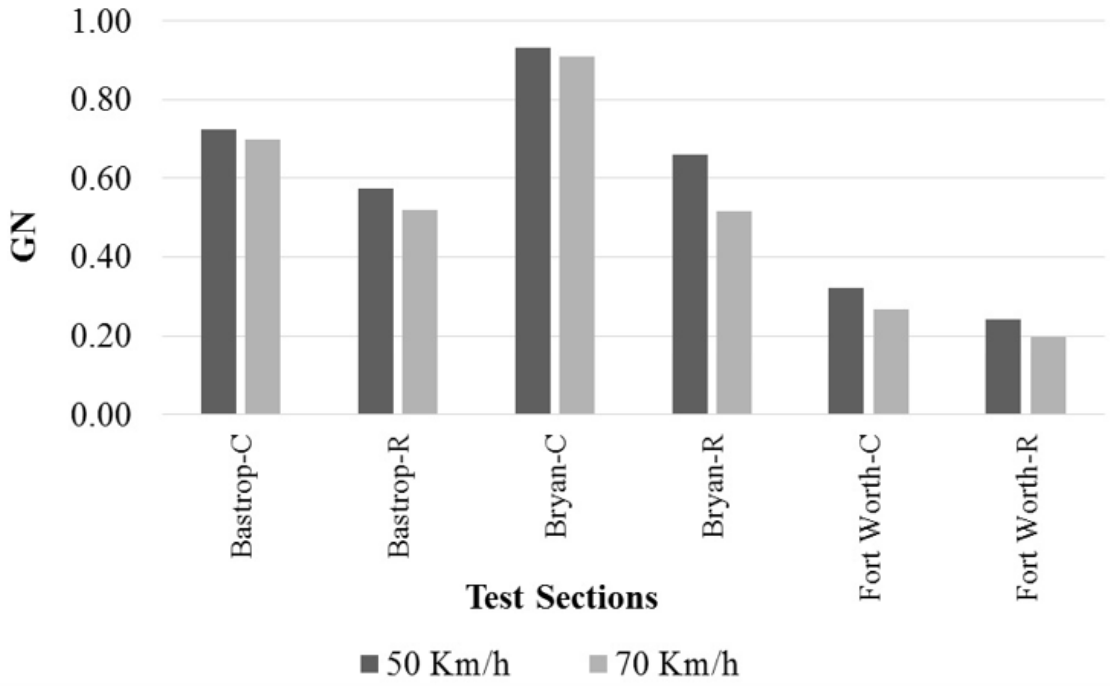

Figure 4.7: The Grip number at different test sections at different speeds.

According to Figures 4.6 (a) and 4.6 (b), the MPD value of the section Bryan-R, which is about 0.70 mm, is lower than Bastrop-R with MPD of 1.50 mm. However, interestingly, in Figure 4.8, the GN at Bryan-R is higher than that of Bastrop-R. It should be mentioned that, in these test locations, the water film thickness of 0.5 mm (applied by Grip-Tester) can only cover a portion of surface texture depth. The PFC pavement is an open-graded friction course that allows drainage of water through the asphalt layer. The surface pavement type of the Bastrop test section is PFC; therefore, the lack of small-size aggregates results in higher MPD values. On the other hand, the mix design of the Bryan test section is dense-graded type C, which contains all ranges of aggregate size and thus results in a lower MPD value but a greater tire-pavement contact area. This indicates that friction-texture relationships are not unique and are significantly affected by surface conditions and mixture types. Therefore, any attempt to establish universal relationships between friction and texture need to incorporate these two variables and possible others too.

Although a PFC mix design increases the surface MPD (and thus causes more hysteresis), PFC's design also decreases the chance of the aggregates being fully exposed and coming into contact with the tire (thus decreasing the contact area and adhesion). A smooth surface is associated with more contact area and better adhesion, but it significantly decreases the MPD that results in lower hysteresis. Therefore, the balance between adhesion and hysteresis in the pavement surface should be optimized in order to maximize the surface friction and skid resistance. This is achievable by using an appropriate mix design providing both macrotexture and microtexture *(Kane et al., 2013).*

The lowest friction was observed in the Fort Worth test sections where the MPD values were below 0.46 mm (0.018 in.). Considering the water film thickness of 0.5 mm

(0.019 in.) applied by the Grip-Tester for wetting purpose, it can be concluded that the surface texture was fully covered by water. In this case, the water trapped in the V- or U-shaped areas of the pavement surface bears the load from the tire and prevents the tire penetrating the spaces between the aggregates—thus reducing the contribution of the aggregate surface to the friction force by decreasing the tire-aggregate contact area *(Meegoda and Shengyan, 2015).*

Relationship between the Texture and Friction

While the GN represent the friction properties of the pavement surface, the MPD values obtained by the LLS and CTM reflect the texture characteristics of the surface. To explore the relationship between the friction and texture, those two groups were plotted against each other in two forms: GN vs. CTM, GN vs. LLS. For this purpose, the data obtained from the segment E, shown in Figure 4.2, were considered. Using statistical analysis, the correlation coefficient (R) was used to evaluate the relationships. The R ranges from -1 to +1, where negative and positive signs represent the negative or positive linear correlation, respectively.

The statistical analysis shows that the relationship between the GN values and MPDs is strongly linear with high correlation coefficients (Figure 4.8). For the Grip-Tester performed at 50 km/h, the R = 0.83 was found for GN-CTM, and R = 0.82 for GN-LLS. In addition, higher correlation coefficients were observed at the speed of 70 km/h. The R values of 0.88 and 0.89 show a strong linear relationship between GN as a friction parameter, and MPDs of CTM and LLS, respectively. Thus, it can be suggested that friction and skid resistance could be estimated by means of texture measurement data with high confidence.

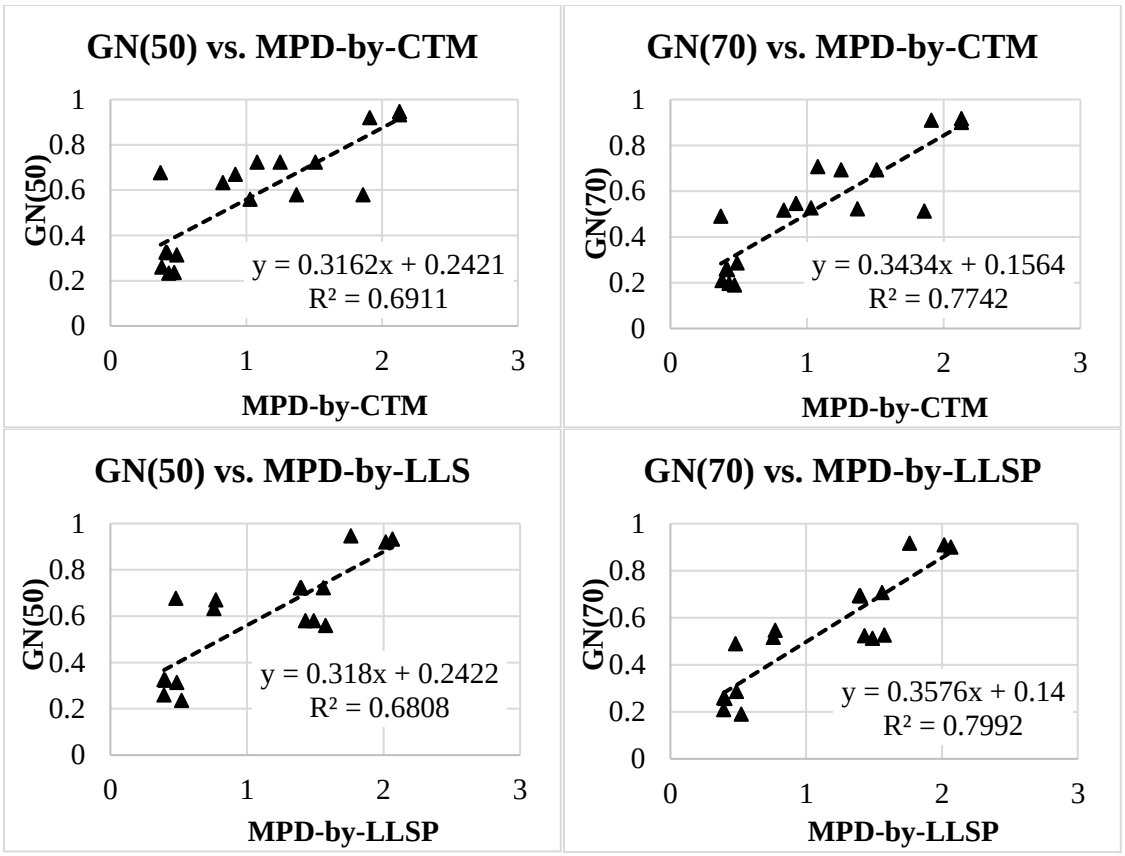

Figure 4.8: Plotted texture-friction data points including GN values, and MPD values.

Chapter 5: An Automatic Method for Measuring the MTD

INTRODUCTION

Pavement's skid resistance is of particular importance in wet conditions. The relationship between the pavement's skid resistance and its surface texture makes pavement texture a vital topic for highway agencies to address. The SPT is the most widely used method of judging the adequacy of the available texture. However, the reliability of this test is questionable because it is operator dependent. This chapter is aimed at proposing a methodology consisting of a laser scanner and an algorithm to represent the SPT on a 3D model of the pavement surface. To achieve this goal, several objectives were defined:

- Conducting several field SPTs on different pavement surfaces, calculating the MTD values, and evaluating the variability of this texture measurement test method,
- Scanning the pavement surfaces using the LLS to create the 3D models of pavement surfaces, and
- Developing a texture measurement algorithm and comparing its repeatability to that of the SPT.

VARIABILITY OF THE SPT

In an effort to address operator's dependency of the SPT, the following field test was performed on two sections in Speedway Street in Austin, Texas. Seventeen operators each conducted two SPTs per section, yielding a total of 34 tests. In each section, every operator performed their test attempt in the same location in order to limit any bias

generated by surface non-homogeneity. Each operator measured the diameter of the sand patch four times along different axis.

Figure 5.1 provides the boxplot of the measured diameters for seventeen operators in two different test sections. These boxplots show the lowest and highest diameters, the first and third quartiles, the median represented by a horizontal line, and the mean (indicated with an "X" mark). These plots illustrate the variation of the diameter measurements for each operator and the variation of the diameter measurements between the operators. It is evident that the sand patch results highly depend on the operator's perception of the edges of the sand patch and its ability to create a circular patch.

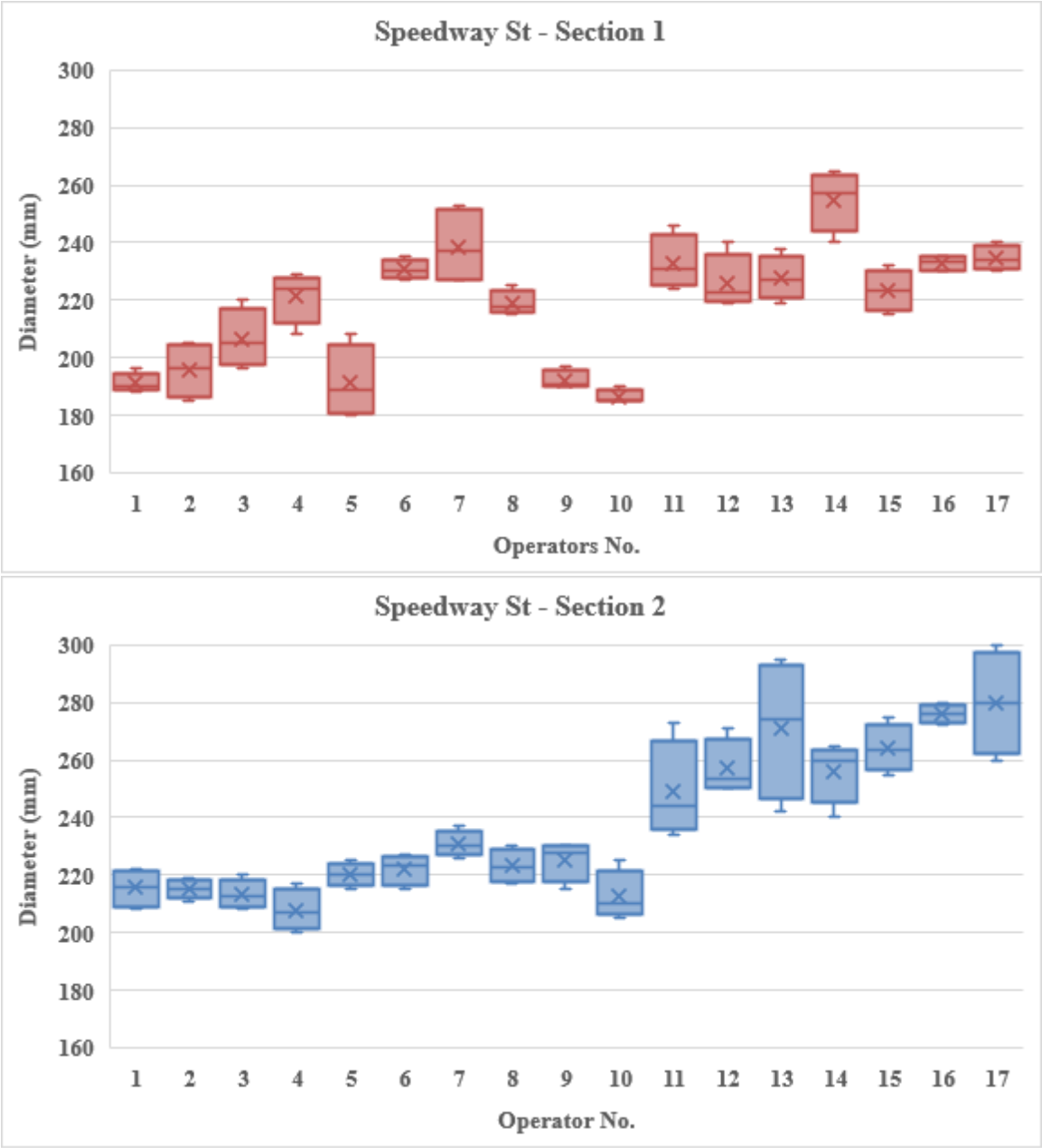

Figure 5.1: Box plots of the measured diameters by the different operators on two sections.

DEVELOPING THE DIGITALIZED VERSION OF SPT

This section describes the development of a new automated MTD measuring algorithm. To meet the objective of this part of the study, several field tests were performed to collect data using the LLS and the SPT. Three test locations across Texas were selected. The chosen locations and tested pavement sections were explained in Chapter 4. Once the surface data acquisition was complete, the scans were subjected to a preliminary filtering step (explained in Chapter 3). The filtering step is required because ignoring this step while creating the 3D models of the pavement surfaces could result in the miscalculation of the MTD.

Generally, in the SPT, the sand filled the pavement surface voids, covering most but not all the peaks. An understanding of how high the sand typically fills the pavement surface depressions helps in deriving a method for calculating the MTD. As suggested by Meegoda et al., 2002 and Hao et al., 2016, a reference point is required in the calculation process of the MTD. For instance, the maximum height value is one of the options as the reference point. However, for pavements with a few large surface stones or debris, the maximum height value could overestimate the MTD. Accordingly, the first consideration in developing this algorithm regards the choice of a general reference point.

For this purpose, a MATLAB algorithm was developed to mimic the SPT in the computer on the pavement surface models. For each test section, the sand patch tests were performed, as illustrated in Figure 5.2 (a), according to the ASTM E965 Standard. In each section, the sand patch test was conducted within the scanned pavement surface to provide consistent texture measurements. The area covered by the patch of sand (shown in Figure 5.2 (b)) was calculated using the average diameter. To simplify the process, a rectangle with an area equivalent to that of the circle was fitted on the

pavement models in the same location as the sand patch test, as depicted in Figure 5(a). The width of the rectangle is equal to width of the scanned area. The length of the rectangle is equal to the calculated sand patch test area divided by the rectangle width. The center of the rectangle coincides with the center of the computer-generated surface model. Afterwards, the considered area was extracted (as shown in Figure 5(b)) and entered into an iterative algorithm for the MTD calculation.

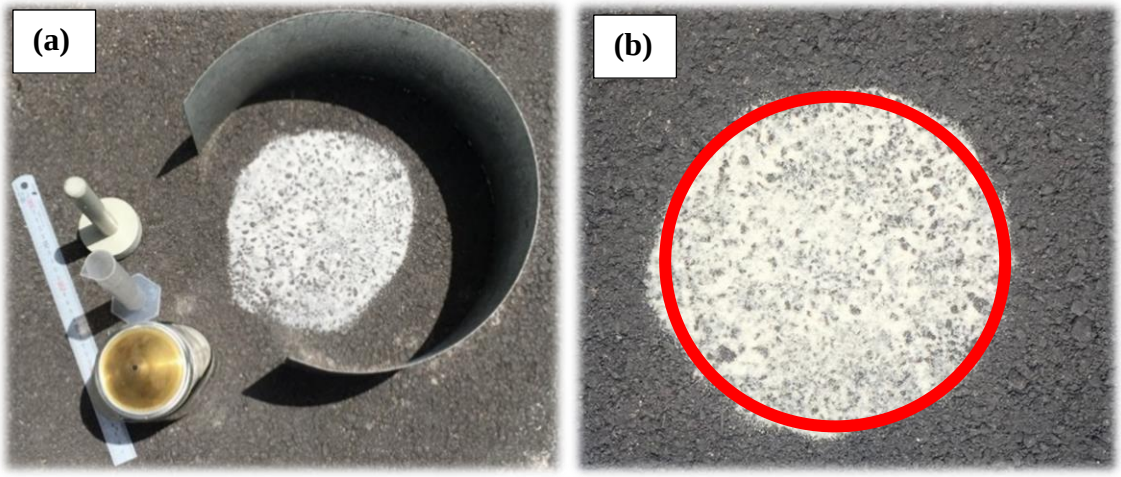

Figure 5.2: a) Sand patch test, b) area of the sand patch.

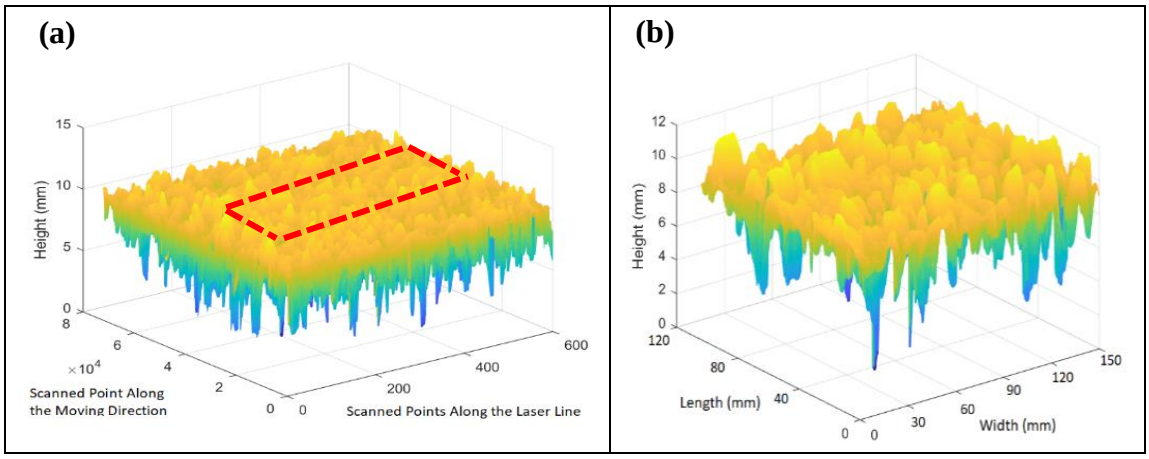

Figure 5.3: Schematic representation of a) the fitted rectangle on the corresponding 3D pavement model, and b) the data within the rectangle.

A schematic illustration of the iterative algorithm is presented in Figure 5.4. In this iterative algorithm, the reference height is simulated at different percentile values of heights ranging from the 50^{th} to the 100^{th} percentile. In each iteration, a uniform horizontal plane is created with a height equivalent to the iterated percentile value, i.e., from the 50^{th} to the 100^{th}. This plane intersects the pavement section, as shown in Table 5.1, and the sand is assumed to fill the voids up to that height value. The pavement surface points below the reference plane are identified and counted. Then, the vertical distance between each point and the horizontal plane is calculated. Afterward, the MTD is estimated as the mean of the vertical distances. The MTD values are shown in Table 5.1.

For each reference plane ranging from 50^{th} to 100^{th} percentile of the surface heights, the MTD values calculated for the eighteen studied pavements sections were plotted against the corresponding measured wet friction coefficients. The friction measurement on these pavement sections was explained in detail in Chapter 4. These plots are provided in Table 5.2. The correlation coefficient (R) was used to evaluate the strength of the correlation between these two variables. As the strength of the relationship between the MTD and friction increases the value of the correlation coefficient increases. As illustrated in the plot presented in Figure 5.5, R has the highest value when the reference plane is at the 94^{th} percentile of the surface heights. Accordingly, the 94^{th} percentile shows the most promising plane for simulating the SPT on the 3D models of pavements.

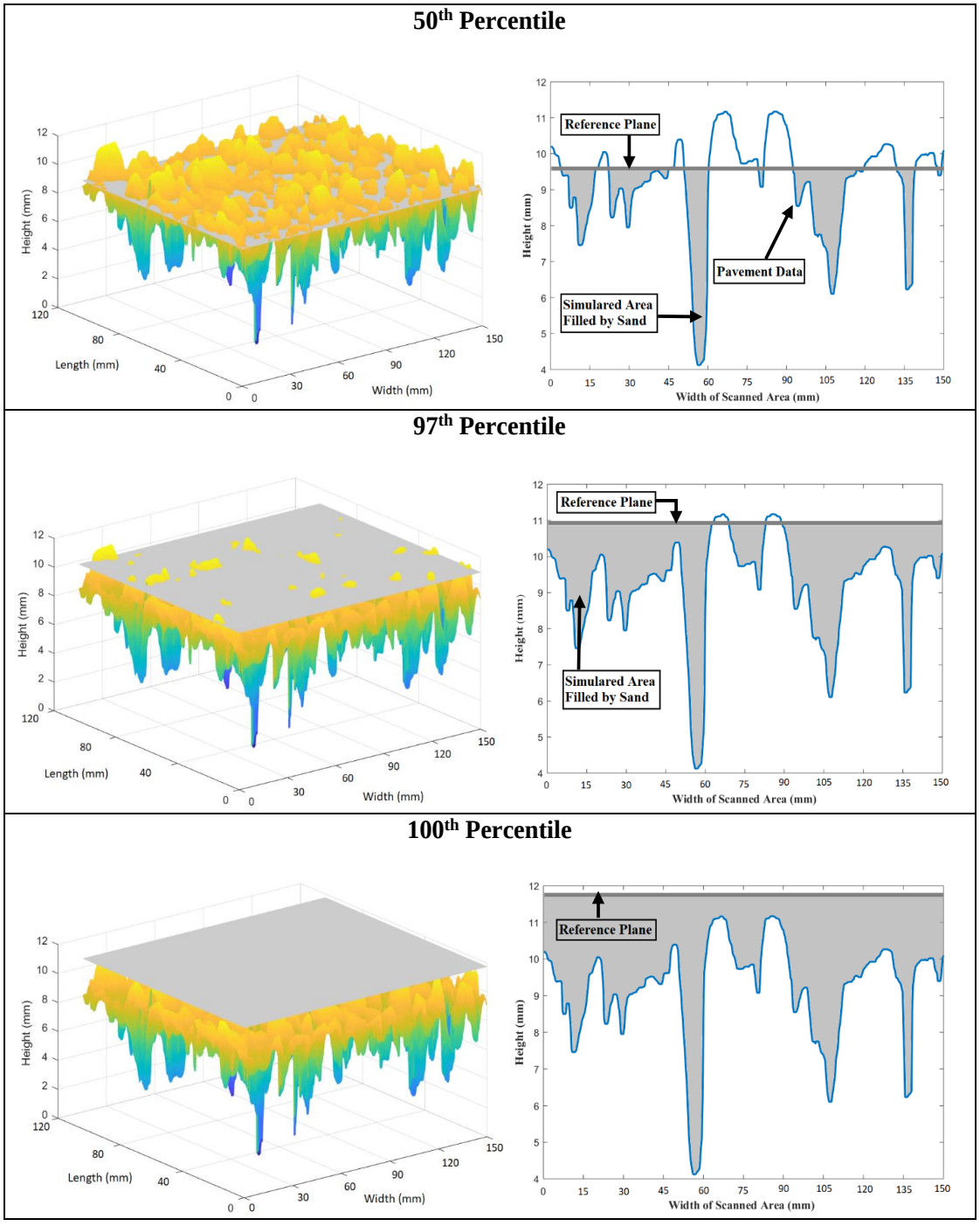

Figure 5.4: 3D representation of the uniform, horizontal plane intersecting the pavement model at 50th, 99th, and 100th percentiles and 2D view of the simulated area between the crossing plane and the lower data points filled by sand.

Location	Bryan						Brastrop US290						Fort Worth IH35					
Surface ID	S1Right	S2Right	S3Right	S1Center	S2Center	S3Center	S1Right	S2Right	S3Right	S1Center	S2Center	S3Center	S1Right	S2Right	S3Right	S1Center	S2Center	S3Center
GN	0.55	0.52	0.49	0.92	0.90	0.91	0.53	0.51	0.52	0.71	0.69	0.69	0.20	0.21	0.19	0.29	0.26	0.26
Percentile	MTD Obtained By the Developed Algorithm																	
50th	0.249	0.149	0.187	0.753	0.893	0.817	0.848	0.962	0.785	0.988	0.995	0.834	0.354	0.252	0.342	0.255	0.261	0.280
60th	0.280	0.158	0.211	0.812	1.003	0.914	0.879	0.980	0.813	1.020	1.020	0.863	0.367	0.254	0.346	0.260	0.261	0.284
70th	0.323	0.175	0.245	0.885	1.131	1.043	0.928	1.045	0.867	1.069	1.080	0.912	0.390	0.262	0.363	0.271	0.269	0.296
80th	0.395	0.208	0.287	1.011	1.335	1.180	1.028	1.158	0.956	1.164	1.191	0.990	0.425	0.278	0.395	0.294	0.293	0.315
85th	0.440	0.238	0.318	1.100	1.457	1.275	1.109	1.249	1.014	1.244	1.287	1.062	0.457	0.292	0.419	0.314	0.315	0.332
86th	0.450	0.245	0.325	1.119	1.485	1.300	1.126	1.273	1.029	1.264	1.315	1.080	0.465	0.296	0.425	0.320	0.321	0.336
87th	0.460	0.253	0.332	1.140	1.518	1.328	1.143	1.299	1.046	1.286	1.344	1.101	0.474	0.299	0.432	0.326	0.327	0.341
88th	0.472	0.262	0.340	1.162	1.552	1.356	1.161	1.330	1.066	1.311	1.373	1.124	0.483	0.304	0.440	0.333	0.334	0.346
89th	0.484	0.272	0.349	1.185	1.588	1.386	1.180	1.362	1.088	1.337	1.402	1.148	0.493	0.308	0.450	0.341	0.342	0.352
90th	0.497	0.283	0.357	1.208	1.629	1.413	1.200	1.393	1.112	1.365	1.434	1.175	0.505	0.314	0.460	0.349	0.352	0.358
91th	0.510	0.295	0.368	1.235	1.683	1.442	1.225	1.429	1.140	1.397	1.468	1.206	0.519	0.320	0.472	0.359	0.361	0.365
92th	0.525	0.308	0.379	1.267	1.740	1.473	1.254	1.467	1.171	1.431	1.509	1.239	0.536	0.327	0.486	0.369	0.372	0.374
93th	0.542	0.324	0.392	1.306	1.802	1.515	1.288	1.509	1.204	1.466	1.560	1.279	0.555	0.335	0.503	0.381	0.384	0.384
94th	0.562	0.342	0.408	1.350	1.861	1.567	1.332	1.553	1.246	1.515	1.624	1.325	0.576	0.345	0.523	0.396	0.398	0.396
95th	0.585	0.361	0.426	1.399	1.912	1.628	1.382	1.606	1.296	1.573	1.706	1.376	0.601	0.357	0.546	0.413	0.414	0.410
96th	0.614	0.383	0.445	1.462	1.971	1.701	1.451	1.670	1.360	1.640	1.825	1.436	0.630	0.373	0.580	0.434	0.433	0.429
97th	0.652	0.409	0.470	1.557	2.037	1.786	1.554	1.756	1.435	1.735	1.994	1.519	0.672	0.394	0.621	0.462	0.459	0.453
98th	0.708	0.445	0.508	1.694	2.109	1.877	1.683	1.890	1.542	1.882	2.157	1.630	0.724	0.427	0.673	0.505	0.497	0.487
99th	0.787	0.502	0.565	1.861	2.224	2.025	1.856	2.087	1.757	2.178	2.479	1.860	0.803	0.483	0.762	0.573	0.566	0.536
100th	1.154	1.268	0.921	2.531	3.704	2.883	5.588	3.440	3.310	7.248	4.398	3.212	1.259	1.327	1.253	1.277	0.960	2.401

Table 5.1: MTD Values.

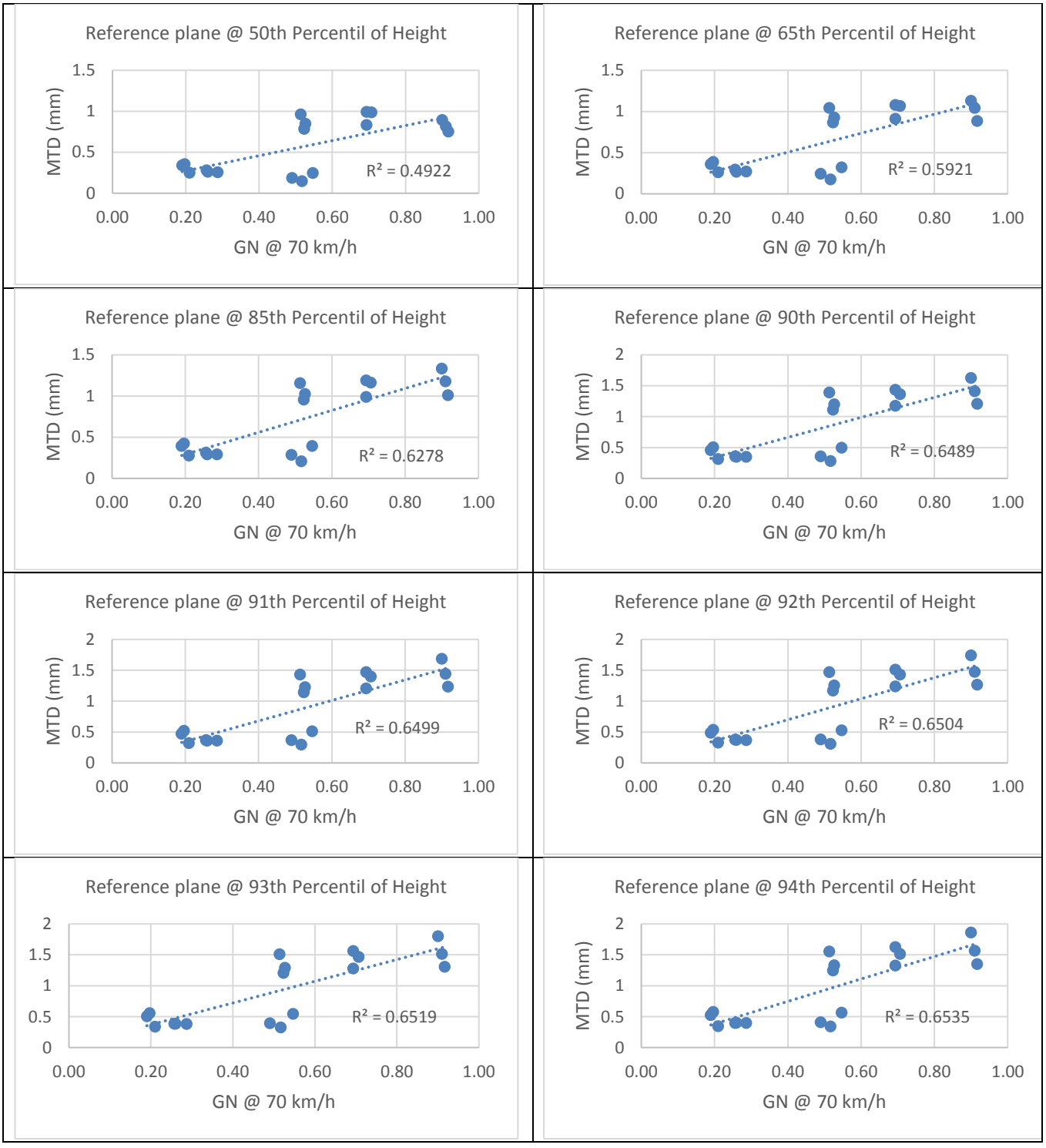

Table 5.2 Continued

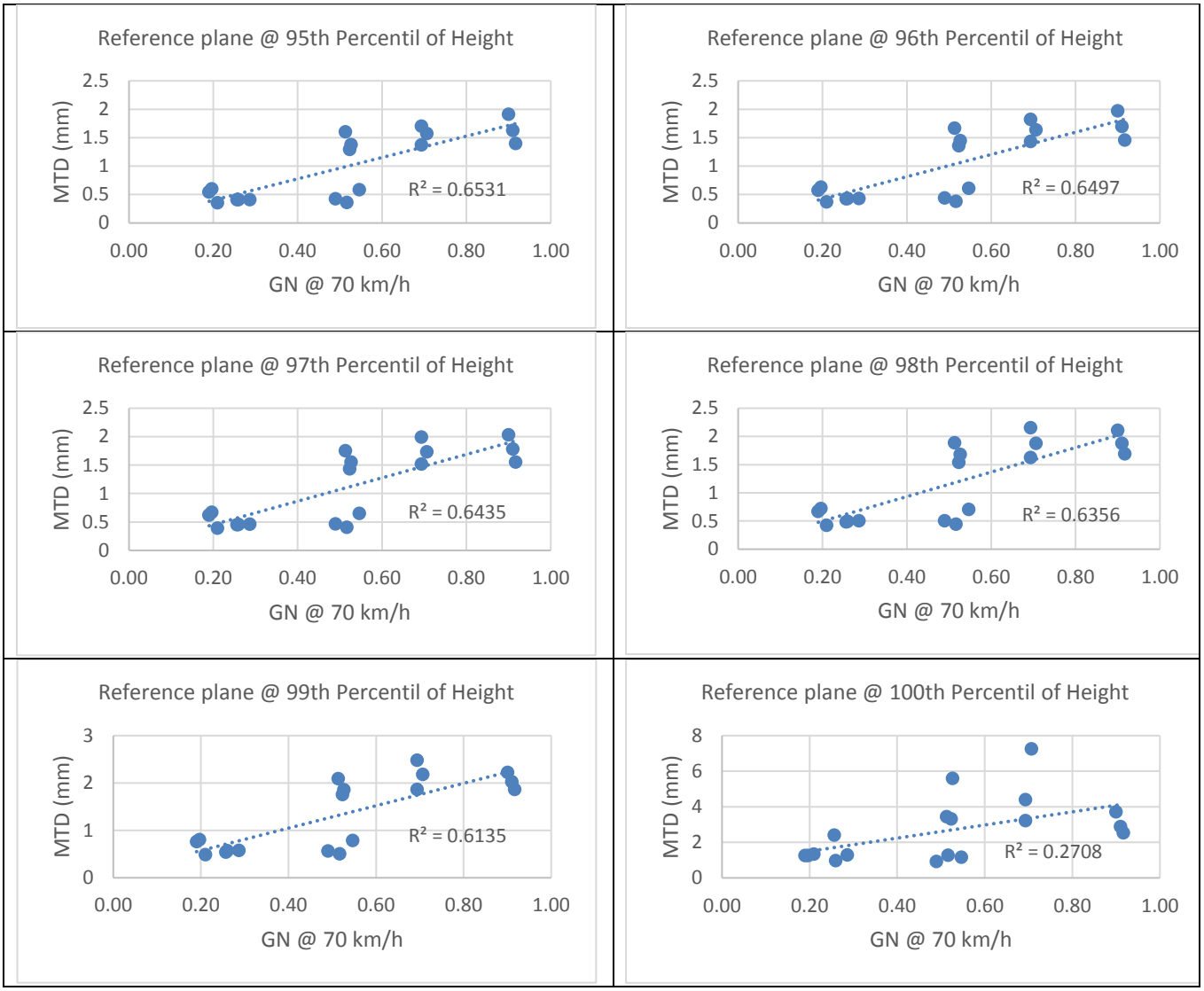

Table 5.2: MTD Values.

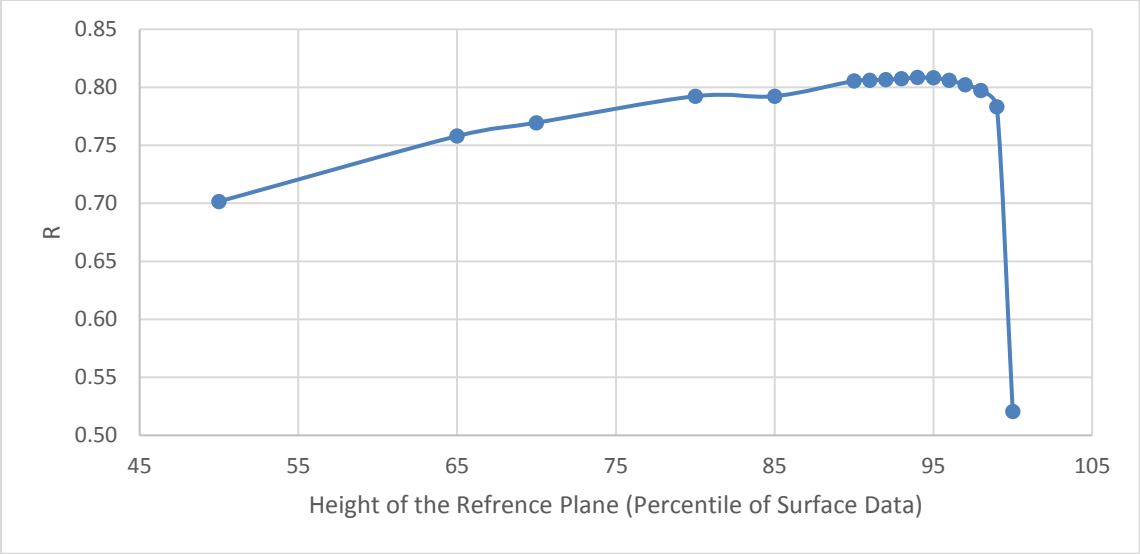

Figure 5.5: Plot of R value vs height of the Reference Plane.

RELIABILITY OF THE DIGITALIZED SAND PATCH TEST

The applicability and the reliability of the developed algorithm was assessed on six other pavement sections, each with a different mix design. The test locations and a picture of their pavement surface are provided in Table 5.4. In each pavement section, two locations were selected where a SPT was conducted followed by a laser scan. The MTD values obtained from the sand patch tests were compared to those obtained from the proposed algorithm. The results of this analysis are presented in Table 5.5. The plot of the MTD values obtained by the SPT versus those obtained by the proposed algorithm are provided in Figure 5.6. The R values of 0.965 shows a strong relationship which indicates that the developed digitalized SPT yields result close to the sand patch test.

San Antonio, US 181	Bryan, US 84	Austin, FM 1626
		
Brownwood, SH36	**Brownwood, IH20**	**Austin, SH195**
	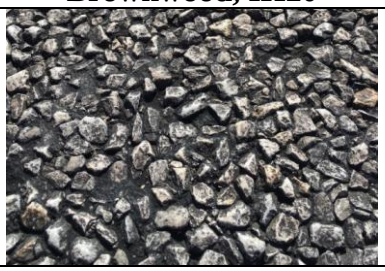	

Table 5.4: Test Locations.

Test Locations	Section #	MTD by SPT	MTD by the Proposed Algorithm
San Antonio, US 181	1	1.36	1.21
	2	1.33	1.21
Bryan, US 84	1	1.18	0.95
	2	1.24	1.07
Austin, FM 1626	1	0.75	0.68
	2	0.73	0.63
Brownwood, SH195	1	1.60	1.46
	2	1.79	1.49
Brownwood, IH20	1	2.33	2.51
	2	2.29	2.16
Austin, Speedway	1	0.71	0.63
	2	0.68	0.63

Table 5.5: MTD results by SPT and the proposed algorithm.

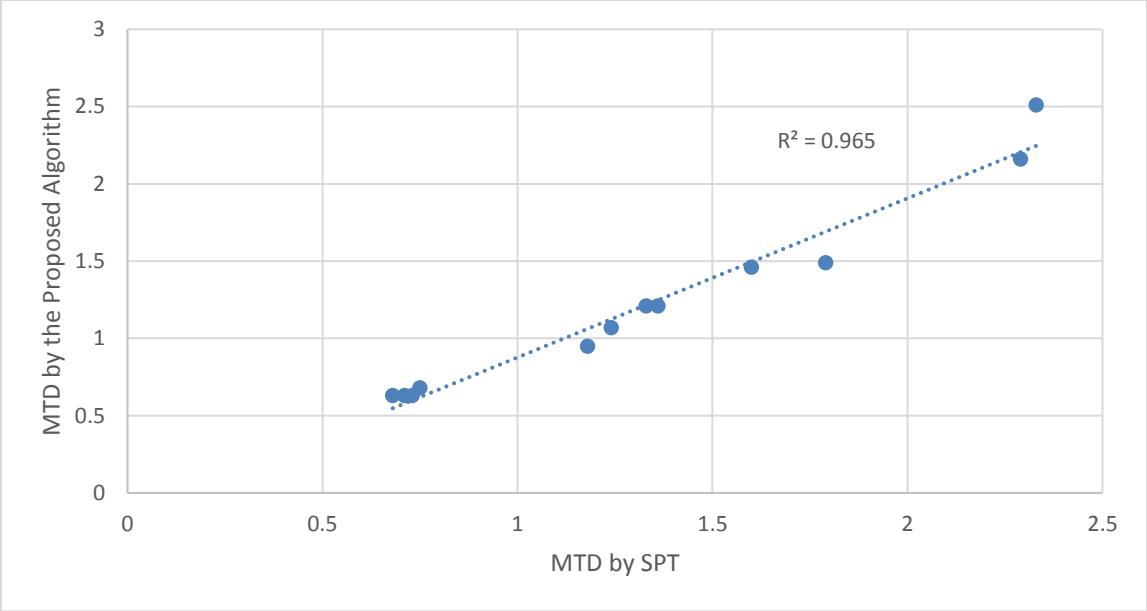

Figure 5.6: Plot of MTD_by_SPT vs MTD_by_proposed.

The experimental results proved the capability of the LLS prototype and the developed algorithm for measuring the MTD on different pavement surfaces. Additional advantages to this prototype are high testing speed and larger area coverage. In contrast, the sand patch test is a tedious test and is limited to few test sections. Using this prototype, larger representative sections along both the width and the length of the road can be assessed. This prototype system has the advantage of capturing 3D data on pavement surfaces using an automatic, simple, and quick operation. In addition, the measuring algorithm can provide more consistent measurement of the MTD. This approach both increases the efficiency of assessing the pavement texture and provides a better understanding of the pavement surface texture.

Chapter 6: Characterizing Aggregate Surface Texture

INTRODUCTION

As mentioned previously, microtexture is an important characteristic of pavement, as it contributes to friction. It is therefore important to carefully select the aggregate properties that exhibit desirable qualities to achieve good performance. To provide enough stability and strength to the asphalt mixture, most specifications limit the amount of aggregate particles with rounded, smooth texture. Aggregates with rough surface texture provide greater surface area between the tire and the pavement. In the case of wet pavements, a rougher microtexture contributes to skid resistance by breaking the thin layer of water on the surface, promoting the contact between pavement and tire required to develop the interatomic attractive forces of the adhesion component (*Serigos et al., 2014; Araujo et al., 2015; Hu et al., 2016; Wang et al., 2017*).

If different aggregate types could be given a unique number, a number that completely characterized its texture, then we would have succeeded in obtaining an objective texture measurement method. Objective characterization of aggregates surface texture would help engineers to select appropriate types of aggregate for different regions with various frictional demands. This chapter intends to find a method for characterizing the aggregates surface texture and, based on that, differentiating the aggregates. The methodology relies on the LLS measurements and numerical methods such as FT and PSD.

MATERIAL PREPARATION

Two different types of aggregate commonly used for asphalt mixtures in Texas were obtained from two different quarries. Three particles were selected from each type

A paper based on this chapter was published: Kouchaki et al., "Evaluation of aggregates surface micro-texture using spectral analysis," Journal of Construction and Building, vol. 156, pp.944–955, 2017. The author of this dissertation contributed to this published article by designing the research methodology, collecting and analyzing the data, and preparing the manuscript.

of aggregate (Figure 6.1). The particles' dimensions are provided in Table 6.1. These aggregates were provided by TxDOT's Materials and Testing Division in Austin, TX. TxDOT's Materials and Testing Division regularly monitors the properties of aggregates produced in different sources based on the following tests:

- Abrasion of Coarse Aggregate Using the Los Angeles Abrasion Machine
- Soundness of Aggregate by Use of Magnesium Sulfate
- Degradation of Coarse Aggregate by Micro-Deval Abrasion
- Acid Insoluble Residue for Fine Aggregate.

In Texas, the above tests are related to the frictional and durability properties of highway construction aggregates. The properties of the selected aggregates for this research study are provided in Table 6.2.

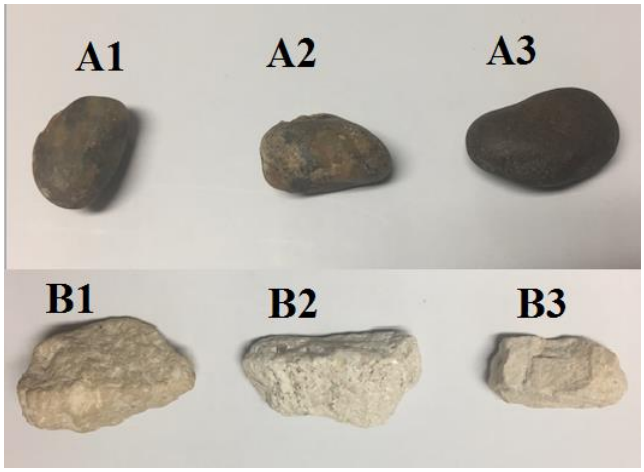

Figure 6.1: Aggregate particles.

Aggregates	Length (mm)	Width (mm)	Thickness (mm)
A1	20.43	12.30	8.65
A2	15.69	11.63	7.45
A3	17.45	13.08	11.12
B1	31.24	19.24	17.02
B2	34.05	17.30	9.74
B3	24.63	12.34	10.07

Table 6.1: Dimensions of aggregate particles used in this study.

Aggregate	Material	SAC	RSLA (%)	RSSM (%)		RSMD (%)	CA-RSAI (%)
				HMAC	ST		
Aggregate A	Crushed Siliceous and Limestone Gravel	A	37	18	13	13	90
Aggregate B	Crushed Limestone	B	30	28	24	24	1

Table 6.2: Aggregates Properties (*CST-M&P, 2016*).

SAC: Surface Aggregate Classification

RSLA: Rated Source Los Angles Abrasion

RSSM: Rated Source Soundness Magnesium

RSMD: Rated Source Micro-Deval

HMAC: Hot Mix Asphaltic Concrete

ST: Surface Treatment

CA: Coarse Aggregate

RSAI: Rated Source Acid Insoluble

The aggregates were first washed in order to remove any dust and undesirable particles. Then, the aggregate particles were oven-heated to 160°C for 24 hours followed by 4 hours of regulated air temperature (23 °C) and humidity (38%) to reach air-dry condition.

DATA COLLECTION

To quantify the aggregate texture, a digital representation of the aggregate surface height profiles is required. The LLS was used to scan the aggregates and to collect their surface height profiles. For this part of the study, the LLS-80 was used. During measurement, and following manufacturer's instructions, the optimum distance between the laser and object (reference distance) was kept to 80 mm. Considering the fact that the mechanism of the laser is based on projecting light and capturing its reflection, all tests were performed in a laboratory with constant light condition to avoid any further signal noise associated to the light variation. Along with the light, the room temperature and humidity, 23°C and 45% respectively, were also kept constant during the experiments.

DATA ANALYSIS

Once the height profiles acquisition step was complete, the scans were exposed to a preliminary filtering step explained in Chapter 3. In this step, all those parts of the scans that do not belong to the aggregate particle were eliminated. For each aggregate particle, one height profile captured on the highest part of the aggregate surface was selected.

Each surface profile consists of macro-level and micro-level components. The macro-level of a surface profile, which associates to the components with large wavelengths, describes the shape of the profile. Components with small wavelengths are related to the micro-level of the profile and form the small irregularities of the profile. To extract spatial information of surface profiles and separate different components, Fourier Transform (FT) was used. The FT performs a decomposition of a height profile into its components at various spatial wavelengths. In Figure 6.2, an example of a surface profile and some of its components with their associated wavelength range are shown.

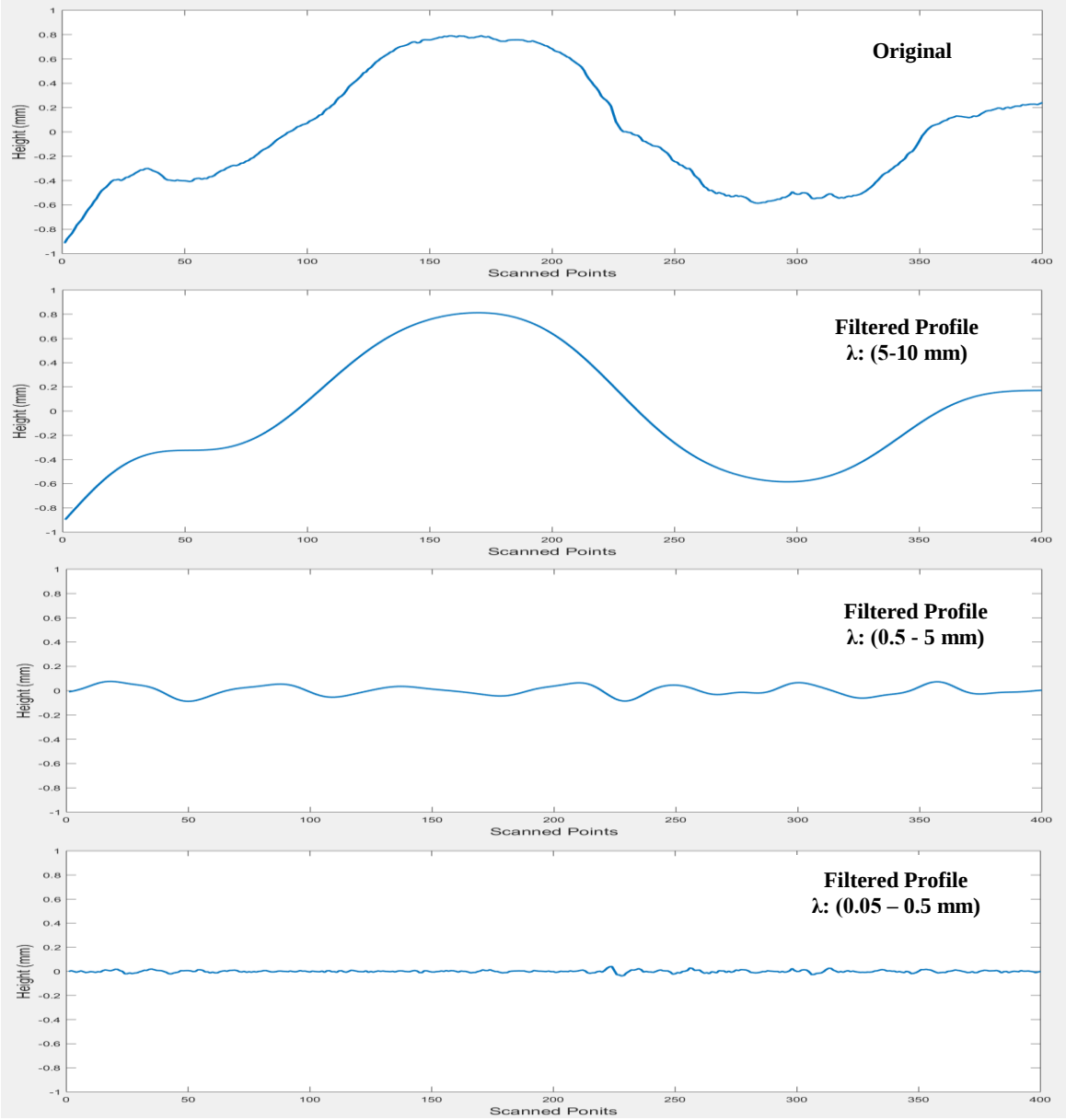

Figure 6.2: An example of a surface profile and its components extracted using FT.

The goal of this study is to differentiate the surface texture of aggregates at different wavelength ranges. Power Spectral Density (PSD) function is useful in this case. This function provides a representation of the amplitude of the profile components as a

function of their spatial frequencies. The PSD of a height profile can be directly calculated using the FT of that profile and squaring the results. In this part, the PSD functions of the profiles were obtained by a MATLAB program. The information associated with the first decades of microtexture (wavelengths between 0.005 mm to 0.50 mm) and the first decade of macrotexture (wavelengths between 0.5 mm to 5 mm) were extracted.

RESULTS AND DISCUSSIONS

Effect of Aggregate Orientation on PSD

In principle, aggregate particles tend to randomly arrange within the pavement surface layer. Hence, studying the aggregates' characteristics associated with surface texture using PSD plots might be affected by aggregates' orientations. To investigate the effect of orientation, aggregate A1 was scanned in four different directions ranging from 0° to 270° with an interval of 90°. It needs to be mentioned that this research assumed that the aggregate particles on the pavement surface settle on their flattest side, the most stable position. In addition, in this research study, the highest part of the surface of the aggregates was of interest since the possibility that the tire contacts with the aggregate particle at the higher points. The surface height profiles were collected. Subsequently, the data were analyzed, and the PSD values were plotted with respect to the wavelengths as seen in Figure 6.3. This figure shows that the PSD plots of different orientations cannot be differentiated and all follow a similar pattern, so it was concluded that the orientation of aggregate particles does not have a significant effect on PSDs. These results are consistent with the outcomes of a study conducted earlier by Wang et al., 2005 which indicated that the influence of aggregate orientation in profile images is negligible.

Comparison of PSD Results

Figure 6.4 presents the PSD of two aggregate groups: A and B (shown in Figure 6.1). According to this figure, the PSD values of aggregates within each group are similar in the first decade of microtexture. Slight differences were observed in the first decade of macrotexture. These results suggest that the PSD of the aggregates in the first decade of microtexture might depend on the mineralogical properties of the aggregates since they are obtained from the same quarry. Therefore, it can be concluded that aggregates obtained from the same source behave similarly in the first decade of microtexture.

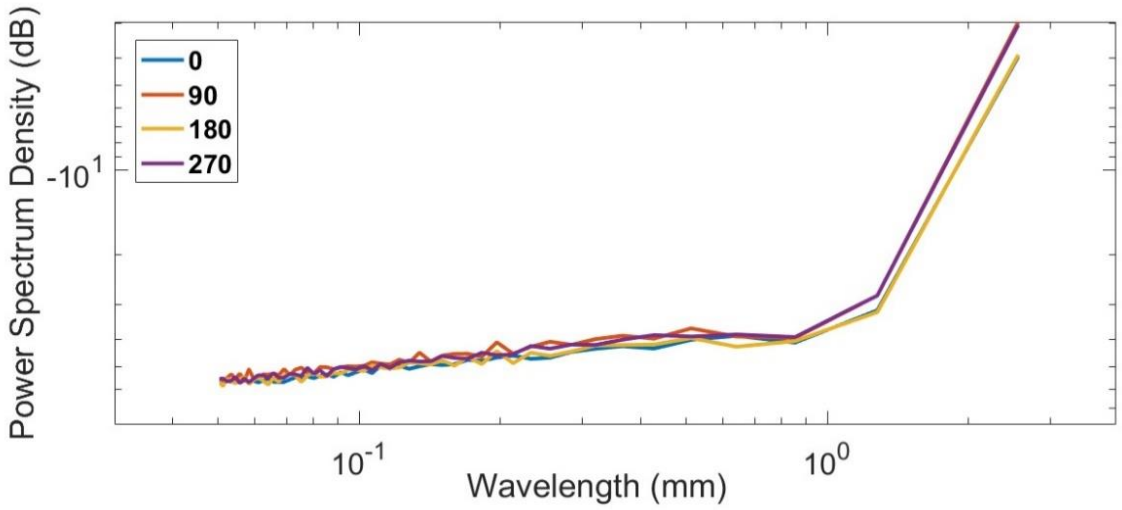

Figure 6.3: PSD of Aggregate A1 in different angles.

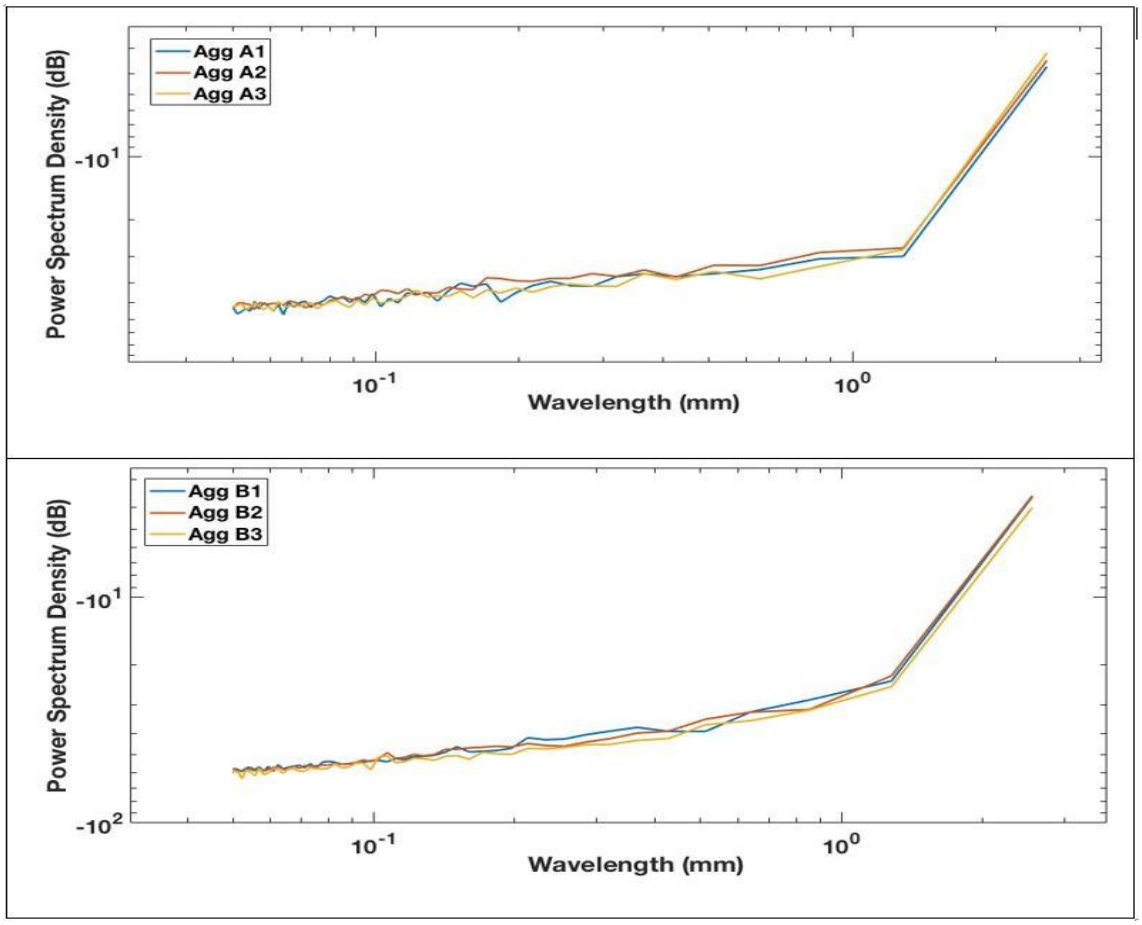

Figure 6.4: Comparison of PSD values of all aggregates.

Paired t-test

To better quantify the aggregates' surface characteristics, two levels of wavelengths (first decade of microtexture, 0.05 to 0.5 mm, and first decade of macrotexture, 0.5 to 5 mm) were broken into smaller sub-bands so that the aggregates can be compared and analyzed in each sub-band in terms of their PSD values. For this purpose, the paired t-test was used. This statistical tool determines if there is a significant difference between the PSD values of aggregates A and B obtained in each sub-band. Table 6.3 provides the wavelength range of each sub-band along with the results of its

paired t-test. The null hypothesis was that there is no statistical difference between the mean PSD values of aggregate A and aggregate B. Note that the significant comparisons remain significant even after multiplicity correction using a rough Bonferroni adjustment. According to the paired t-test results, the PSD data for aggregates in all microtexture sub-bands can be differentiated; however, the test shows no significant difference in the macrotexture sub-bands, indicating that the PSD in those sub-bands could not be differentiated. Hence, the macrotexture data were eliminated and the microtexture data were used for further investigation.

Sub-band	Range (mm)	t stat	P-value	Possibility of Differentiation
First part of micro-texture (L1)	0.05 – 0.075	19.9	0.00	Yes
Second part of micro-texture (L2)	0.075 – 0.1	25.62	0.00	Yes
Third part of micro-texture (L3)	0.1 – 0.25	11.25	0.00	Yes
Fourth part of micro-texture (L4)	0.25 – 0.5	6.54	0.002	Yes
First part of macro-texture (L5)	0.5 – 1.0	1.44	0.29	No
Second part of macro-texture (L6)	1.0 – 2.56	-1.46	0.38	No

Table 6.3: Sub-Bands of Wavelengths.

Evaluation of Root Mean Square Roughness (Rq) and Depth of Surface Roughness (Rp)

The spatial signals captured with the LLS from the aggregate's surface texture were processed using band-pass filters in order to separate the microtexture components.

The profiles in the frequency domain were cut off between the wavelengths 0.05 to 0.075 mm, 0.075 to 0.1 mm, 0.1 to 0.25 mm, and 0.25 to 0.5 mm. These wavelength cut-offs were selected based on the defined sub-bands in Table 6.3 for the first decade of microtexture. The filtered profiles were subsequently used to compute the texture parameters Rq and Rp in the space domain. A research study conducted by Cafiso and Taormina in 2007 found that there was a good correlation between these two parameters and surface friction. As an example, Figure 6.5 shows the height profile of aggregate A1 along with the four filtered profiles that were used to calculate the Rq and Rp values.

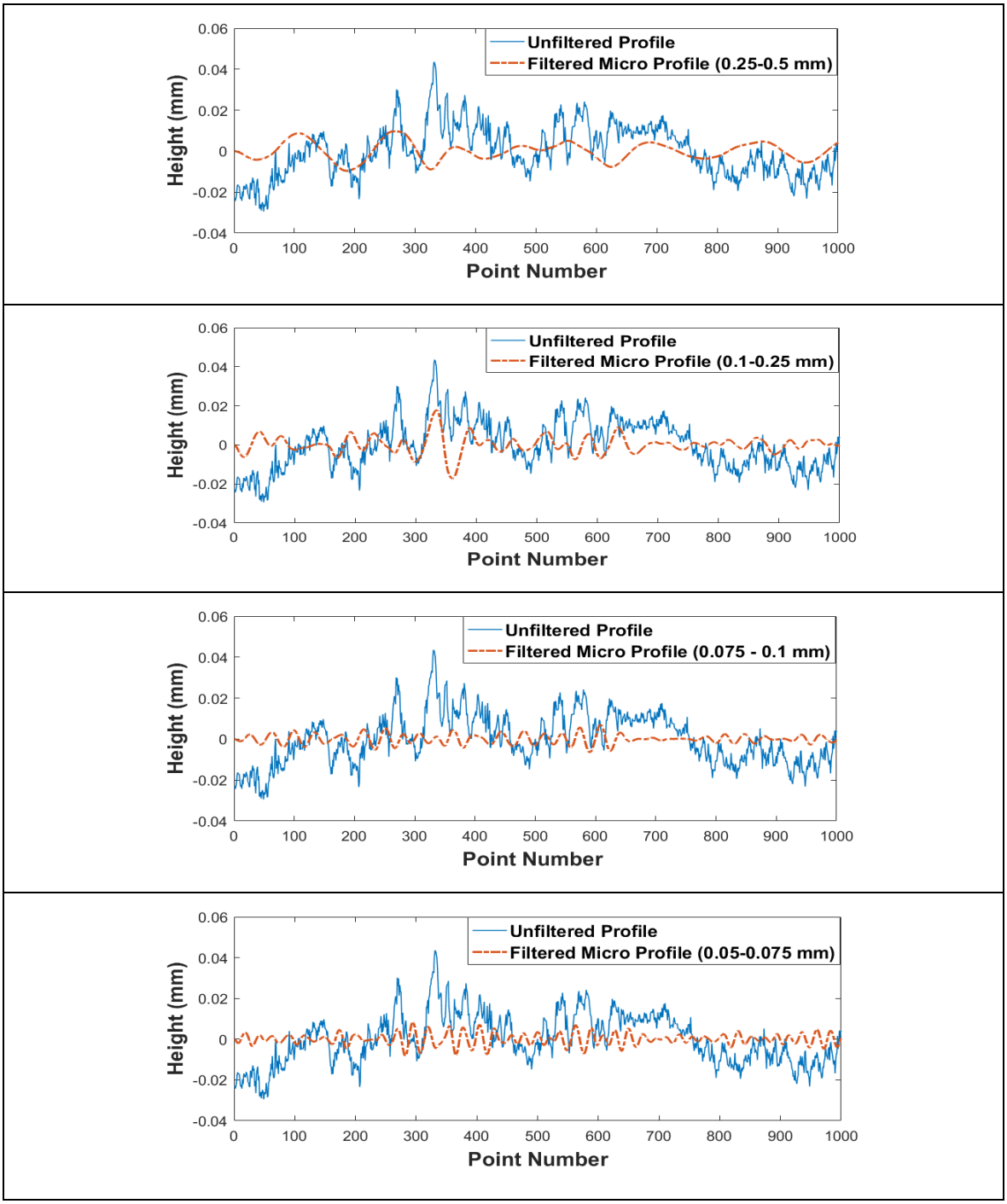

Figure 6.5: The profile of aggregate A1 with the micro-scale filtered profiles.

Figure 6.6 shows the texture parameters Rq and Rp calculated for the different sub-bands (L1 through L4). As this figure demonstrates, the Rq and Rp values of aggregate type A are significantly higher than those in aggregate type B in all sub-bands except L4 (0.25-0.5 mm). The difference between the Rq and Rp values is more significant in sub-bands L1 (0.05-0.075 mm), L2 (0.075-0.1 mm), and L3 (0.1-0.25 mm), therefore, quantifying the different microtexture of aggregates A and B.

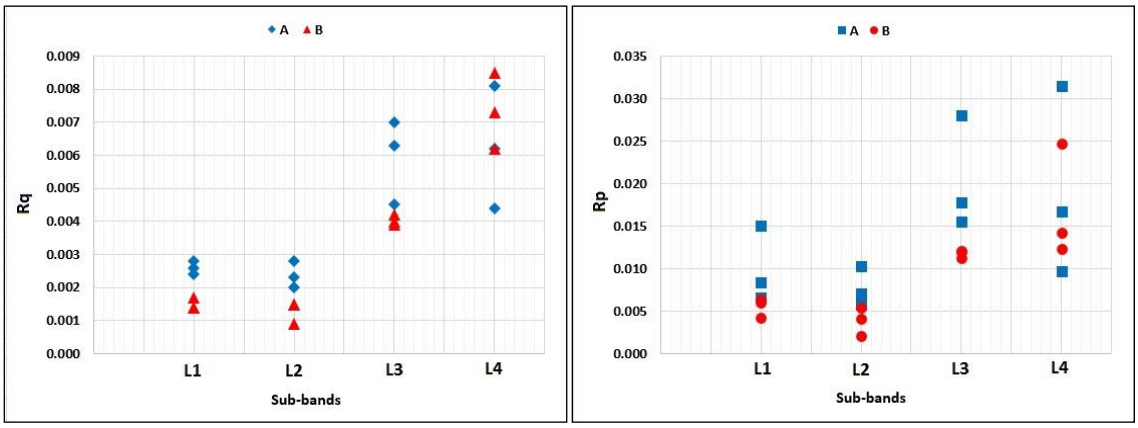

Figure 6.6: a) Root mean square roughness values in different sub-bands of wavelengths; b) Values of the depth of surface smoothness in different sub-bands of wavelengths.

Comparing Texture Parameters

Table 6.4 provides a comparison between the texture parameters used in this study to differentiate aggregates in four ranges of wavelength. The results showed that in the frequency domain, PSD can capture the differences between the surface texture of two aggregates at four ranges of microtexture, L1 to L4. In the space domain, the two parameters Rq, and Rp, were able to distinguish the variation between the surface texture of aggregate in the first three ranges L1 to L3. Accordingly, the results of PSD, Rq, and Rp were consistent only in the wavelength range of 0.05 to 0.25 mm.

Texture Parameters	**Wavelength Range (mm)**					
	Microtexture				**Macrotexture**	
	L1 (0.05-0.075)	L2 (0.075-0.1)	L3 (0.1-0.25)	L4 (0.25-0.5)	L5 (0.5-1.0)	L6 (1.0-2.5)
PSD	✔	✔	✔	✔	X	X
Rq	✔	✔	✔	X	X	X
Rp	✔	✔	✔	X	X	X

Table 6.4: A side-by-side comparison of texture parameters in different wavelength ranges.

SUMMARY

Nowadays, due to the expansion of high-resolution scanners characterization of texture on different scales is possible. However, in general, the assessment of pavements surface texture is limited to the macro-level. Various research studies have shown that the measurement of smaller texture scales is essential concerning skid resistance. Therefore, improvement of surface texture characterization at the micro-level is needed.

In this part of the study, measurements of surface texture were made on two types of aggregates using the LLS prototype. Using the filter method, the texture features were divided into four ranges of wavelengths. Quantitative analysis of surface texture was carried out using the texture parameters, PSD, Rq, and Rp. The results of this chapter showed potential applicability of the developed LLS prototype in the field of aggregate texture quantification which could enable transportation agencies to assess and differentiate the aggregates with regard to their texture properties.

Chapter 7: Clustering Aggregates Based on Polishing Resistance

INTRODUCTION

With the passage of the time, traffic polishes off the texture of the pavements which results in smoothed and round aggregates. The aggregates capability of being resistant to polishing should be considered before any pavement construction. Failing to consider this aspect in the mix design process would result in increasing the risk of accidents.

This chapter presents an analysis of the polishing resistance of aggregates. In order to investigate the polishing resistance, the evolution of aggregate surface texture after the polishing process was assessed. Micro-Deval polishing machine and the LLS were utilized. This chapter also presents the results of clustering analysis to group the examined aggregate particles based on their polishing resistance. Model-based clustering technique was utilized in order to group aggregate particles. In this research, Bayesian estimation was employed to perform statistical inference on the classification model.

MATERIALS

Seven different aggregate sources from Texas were studied for this part. The chosen aggregate sources are commonly used in Texas for road construction. The used aggregates have different mineralogical characteristics. Some of these aggregates are sandstone, limestone, and granite, while a few of them are basalt and lightweight aggregates. Personnel from TxDOT's Materials and Testing Division provided these aggregates. The material type of the chosen aggregates is given in Table 7.1.

POLISHING AGGREGATE PARTICLES

Each aggregate was divided into two groups. One group was polished, and the other group was kept as non-polished samples for comparison. Polishing was performed using the Micro-Deval apparatus in the TxDOT laboratory. The Micro-Deval test was conducted according to the Tex-461. The results of Micro-Deval testing are provided in Table 7.1. As shown in Table 7.1, the selected lightweight aggregates have the highest weight loss in the Micro-Deval. Examples of the polishing effect in the Micro-Deval test are shown in Figure 7.1. Figures on the left show aggregate particles from the non-polished group and figures on the right show aggregate particles taken from the polished group. Performing visual inspection, it could easily be observed that the surface texture of aggregates changed due to polishing.

Aggregate Particles from Quarry # 3	
Non – Polished Particles	Polished Particles
	
Aggregate Particles from Quarry # 5	
Non – Polished Particles	Polished Particles
	

Figure 7.1: Examples of the Polishing Effect in the Micro-Deval Test.

In addition to Micro-Deval polishing, soundness loss measurement and rating of acid insolubility were also obtained for the selected aggregates. The results are tabulated

in Table 7.1. According to the TxDOT aggregate classification, the quarries #1, #4, #5, and #7 fall into the classification of A and the quarries #2, #3, and #6 are in the classification of B.

Quarry No.	Material	MDML (%)	MSL (%)	AIR (%)	SAC
1	Crushed Granite	3	1	99	A
2	Crushed Limestone	15	16	4	B
3	Crushed Dolomite	13	6	12	B
4	Crushed Sandstone	8	11	99	A
5	Basalt	10	3	100	A
6	Crushed Dolomite	11	1	7	B
7	Slag	29	2.4	99	A

Table 7.1: Aggregate Properties.

MDML: Micro-Deval Mass Loss

MSL: Magnesium Soundness Loss

AIR: Acid-Insoluble Residue

MEASURING AGGREGATE SURFACE FRICTION

In TxDOT's aggregate laboratory, Dynamic Friction Tester (DFT) is used to measure the aggregates surface friction before and after the Micro-Deval polishing process. DFT (shown in Figure 7.2(a) and 7.2(b)) is a stationary compact device used for measuring the friction coefficient. It consists of a rotating disk and three rubber pads attached to the bottom of the disk. The disk is pushed by an electric motor to rotate until

it reaches the target speed set by an operator. At the same time, water is applied to the target surface. The disk drops and the rubber pads come into contact with the wet area. Each rubber pad is loaded vertically at 11.8 N (2.65 lb). The friction force developed between pads and the pavement slows down the disk. The DFT measures the friction coefficient continuously until the disk stops completely (*Huang and Pan, 2006; Masad et al., 2009*). The coefficient of friction is the ratio between the friction force or horizontal torque force and the applied vertical load on the rubber sliders of the DFT (*Austroads, 2005*).

The DFT is applied on a ring-shaped specimen of aggregate particles (shown in Figure 7.2 (c) and (d)) to measure the coefficient of friction. The ring is a circular grove with a depth of 1/8 inch (3.18 mm) made on high-density polyethylene (HDPE) template as can be seen in Figure 7.2 (c). Before placing the aggregates on the ring, a debonding grease is used to allow the ring to be removed from the HDPE template. Using a ratio of 0.8 lb (351 gram) of polyester to 0.06-ounce (1.7 gram) methyl ethyl ketone peroxide provides enough time to work (placing and rolling) with the aggregates before the polyester hardened. With the use of a scoop with the same width as the ring, the aggregates are manually introduced to the areas of the ring to create a loose arrangement while the HDPE template is rotated slowly on a turn table. Then, the aggregates should be flushed with the HDPE template surface. This can be done by rolling a hard rubber roller over the aggregates. The last step of the ring preparation is curing, in which the specimen is left for about an hour (*Mercado et al., 2018*). A finished specimen can be seen in Figure 7.2 (d).

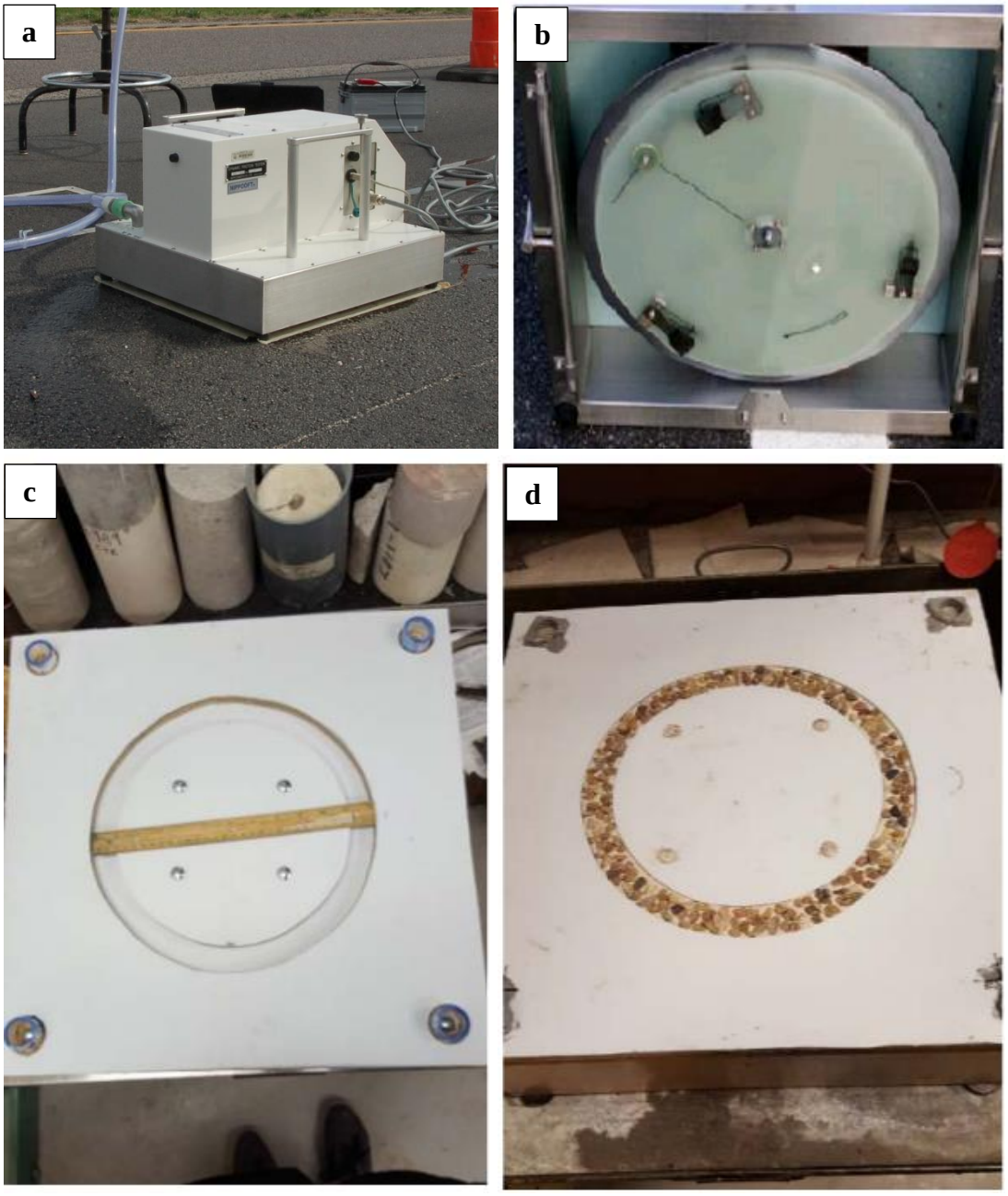

Figure 7.2: (a) DFT Device, (b) Bottom View of DFT, (c) Ring Shaped Specimen, (c) HDPE Template, (d) Cured Ring-Shaped Specimen (*Mercado et al., 2018)*.

Table 7.2 provides the results of the DFT test for quarry aggregates obtained before and after the Micro-Deval polishing process. The results show that aggregates obtained from quarry #3 have the lowest values of DFT_{before} and DFT_{after}. On the other hand, aggregates from quarry #5 show the highest amounts of DFT_{before} and DFT_{after}. This quarry aggregate also presents the lowest drop in friction (DFT_{drop}) after polishing while the aggregates taken from quarry #6 have the highest value of the DFT_{drop}.

Quarry No.	DFT Before Polishing (DFT_{before})	DFT After Polishing (DFT_{after})	DFT_{drop}
1	0.608	0.487	0.121
2	0.352	0.246	0.106
3	0.407	0.281	0.126
4	0.737	0.521	0.162
5	0.792	0.730	0.062
6	0.463	0.272	0.191
7	Not Available	No Available	No Available

Table 7.2: Aggregates Friction Results.

In Figures 7.3 (a), (b), and (c), the values of DFT_{drop} were compared to the results of the Micro-Deval percentage mass loss, soundness loss, and acid-insoluble residue results respectively. These graphs showed that there is no correlation between the DFT_{drop} and measured aggregate properties. One possible explanation for this is that the results of DFT tests could be highly affected by factors such as the arrangement of the particles, their size distribution and the magnitude and number of gaps between the

aggregates. This means that this test is affected by the hysteresis component of the friction, and hence could not reliably and adequately describe the friction created by the surface texture of aggregates.

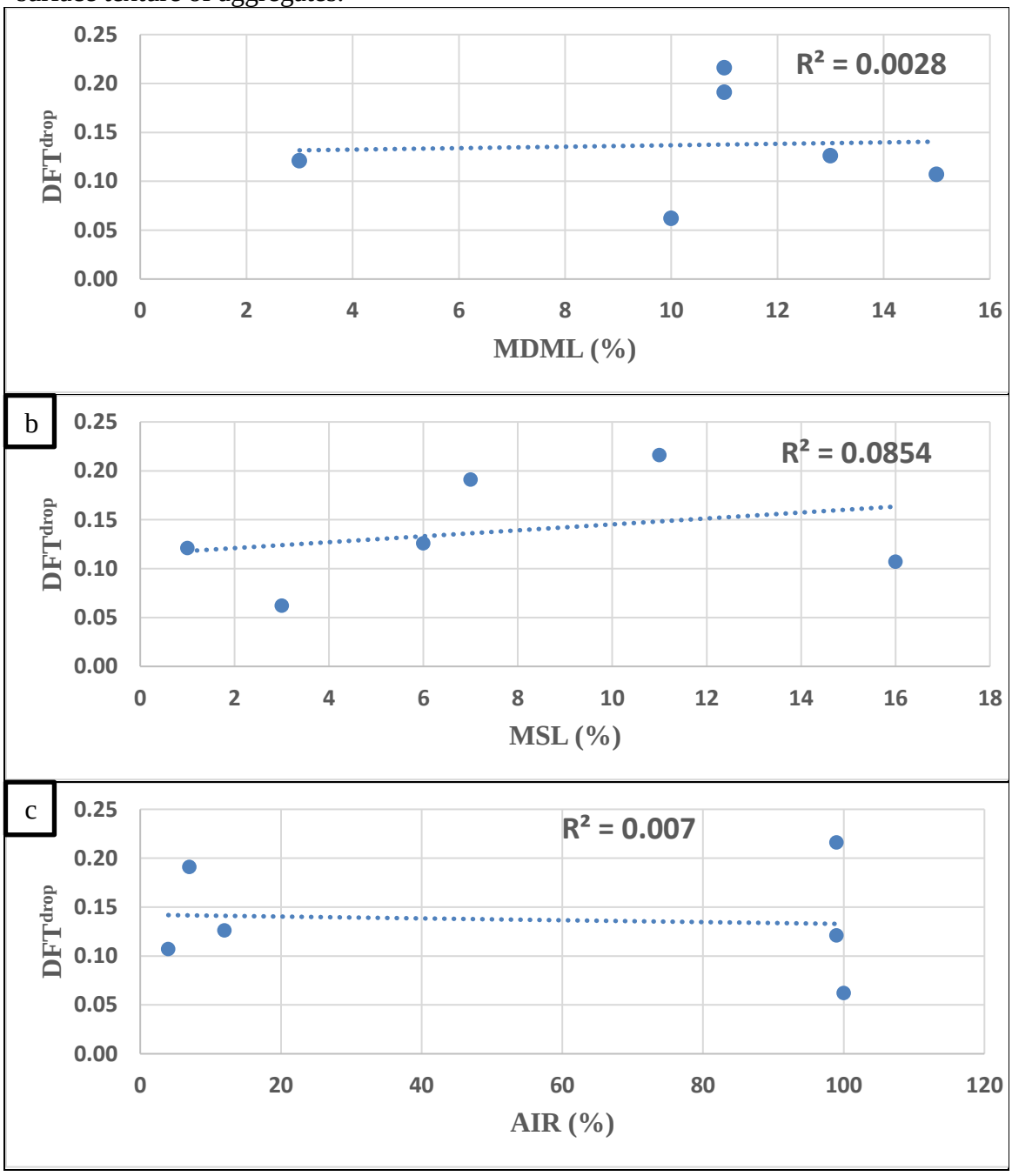

Figure 7.3: Plots of (a) DFT_{drop} Values to Micro-Deval Mass Loss Results, (b) DFT_{drop} Values to Soundness Test Results, and (c) DFT_{drop} values to Acid Insoluble Residue Results.

MEASURING AGGREGATE SURFACE TEXTURE

Masad et al. (2009) found that the change in aggregate texture before and after Micro-Deval and the texture after Micro-Deval both are significant factors for assessing the friction resistance of pavement mixtures. Accordingly, this study aimed to assess the feasibility of using the texture change after polishing to differentiate the aggregates. Following the polishing process, surface elevation profiles were obtained using the LLS – 80 and analyzed to determine the rate of change in the surface texture of aggregate samples.

As previously mentioned, an acceptable level of microtexture is necessary at all stages of the pavement life to break up the remaining layer of the water and promote the bonding between the tire and the pavement surface. The role played by the microtexture under wet pavements give importance to the depth level of aggregates texture profiles as well as their roughness of texture. To measure these two features of surface profiles, several texture parameters were used. Power spectral density (PSD), root mean square roughness (R_q), and mean profile depth (MPD) which measure the height level of texture profiles. Root mean square slope (Δ_q) and root mean square second derivative of the profile **(**δ_q) which measure the rate of roughness of texture profiles. The mathematical formulation of these parameters is provided in the following sections:

1. Power Spectral Density (PSD)

The texture analysis done in Chapter 6 showed that the PSD values of the two aggregate types vary significantly in the micro level within the wavelength range of 0.05

to 0.25 mm. In this chapter, the PSD results within this wavelength range were used to compare the surface texture change of the aggregates. The PSD of a surface profile contains a large amount of data; hence it is not appropriate to be directly utilized as a discriminator. A further data reduction needs to be done to obtain a parameter that summarizes the PSD. Cafiso and Taormina in 2005 conducted a study to identify some parameters of the aggregate profile having a direct connection with skid resistance. In the microtexture level, the results of their analysis showed that the area under the PSD curve has a significant correlation with the British Pendulum number. Accordingly, the area under the PSD curve was used in this part of the study.

2. Root Mean Square Roughness (R_q)

The mathematical definition of R_q is shown in Equation 7.1. R_q represents the standard deviation of the profile height values. This parameter is sensitive to large deviation from the mean line (*ASME B46.1*).

$$R_q = \sqrt{\frac{1}{n}\sum_{i=1}^{n}(y_i - \bar{y})^2} \qquad \textbf{Eq 7.1}$$

Where R_q = root mean square roughness (mm), y_i = the individual values of the profile (mm), $\bar{y}$ = average value (mm), n = number of points.

3. Root Mean Square Slope of the Profile (Δ_q)

The concept of the root mean square was extended to the first and second derivatives of the height profile by Myers in 1962 and resulted in two texture parameters, the slope variation and the curvature of a profile. The mathematical formulation of slope variation is presented in Equation 7.2. As shown in Figure 7.4, a surface profile whose

amplitudes change slowly regarding space gives a low value of Δ_q while a profile that fluctuates widely results in the high value of Δ_q (*ASME B46.1*).

$$\Delta_q = \sqrt{\frac{1}{n-1}\sum_{i=1}^{n}(\theta_i - \bar{\theta})^2}, \qquad \textbf{Eq 7.2}$$

$$\theta_i = \frac{y_{i+1} - y_i}{\Delta x}$$

Where Δ_q = root mean square slope, θ_i =Slope between i+1th and ith points, $\bar{\theta}$ = mean slope, which is determined by calculating all slopes between each two successive points of a surface profile, then calculating the average of these slopes., *n* = number of points.

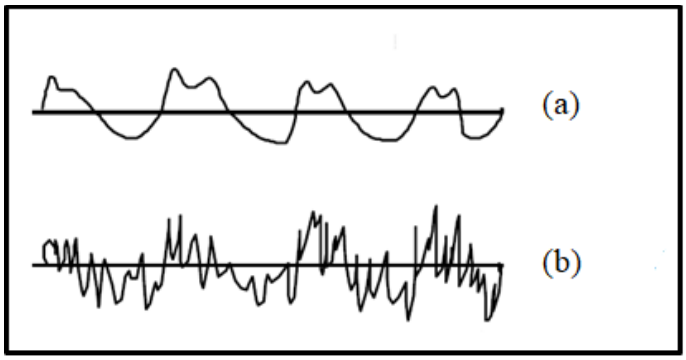

Figure 7.4: Examples of Profiles with (a) Low Δ_q and (b) High Δ_q.

4. Root Mean Square Second Derivative of the Profile (δ_q)

δ_q is calculated through Equation 7.3. This parameter represents the rate of height change in a surface profile.

$$\delta_q = \sqrt{\frac{1}{n-1}\sum_{i=1}^{n}(\dot{\theta}_i - \bar{\dot{\theta}})^2}, \ \dot{\theta}_i = \frac{\theta_{i+1} - \theta_i}{\Delta x}, \ \bar{\dot{\theta}} = \frac{1}{n-2}\sum_{i=1}^{n-2}\frac{\theta_{i+1} - \theta_i}{\Delta x} \qquad \textbf{Eq 7.3}$$

Where δ_q = root mean square of the second derivative of the profile (mm^{-1}), $\dot{\theta}_i$ = The second derivative of profile between $i+1^{th}$ and i^{th} points, θ_i =Slope between $i+1^{th}$ and i^{th} points, $\bar{\dot{\theta}}$ = mean of second derivatives, n = number of points.

5. Mean Profile Depth (MPD)

At the macrotexture level, the MPD is calculated for the profiles having a baseline of 100 mm. This baseline corresponds to two times the maximum wavelengths in the macrotexture range (*Zuniga, 2017*). For the microtexture level, there is no standard for the length of the baseline. In 2014, Serigos et al. demonstrated that baselines shorter than 10 mm could improve the prediction of surface friction and suggested a baseline of 1.0 mm for describing microtexture. Accordingly, in this study, a baseline of 1.0 mm was used in the MPD calculation.

To calculate the MPD, first, the captured height profile is divided into segments with a length of 1 mm. The second step is to correct for the inclination slope of the segments such that a regression line is calculated and then subtracted. Then, each 1-mm segment is divided into two 0.5-mm segments for which the maximum height is calculated. MPD is calculated as the average of the determined maximum heights.

TEXTURE DATA ANALYSIS

Each aggregate sample considered for this analysis consists of 60 aggregate particles: 30 particles taken from the non-polished aggregates and 30 particles obtained from the polished ones. Thirty surface profiles were obtained for a particular aggregate particle. Several discrete height profiles, as the aggregate surface topography, captured by the laser scanner, are presented in Table 7.3. The plots show that for quarries #2, #3, #6, and #7 polishing has a significant impact on the surface texture of aggregates while it has

little effect on aggregates from quarry #4. Visually, no texture changes can be observed on quarries #1 and #5.

Quarry # 1			
Non-Polished	Particle #1	Particle #2	Particle #3
	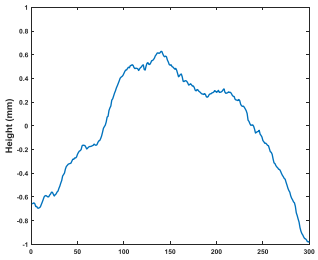	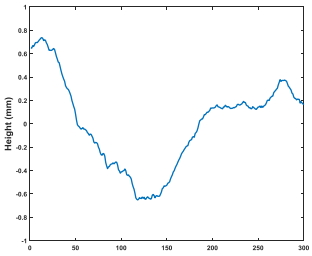	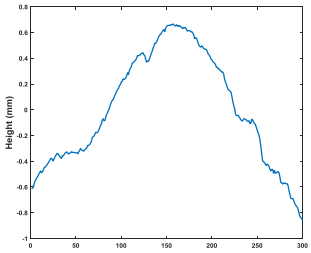
Polished	Particle #4	Particle #5	Particle #6
	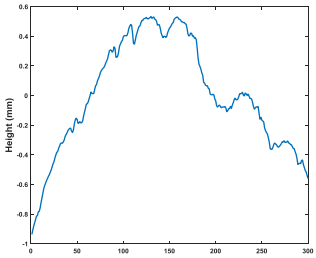	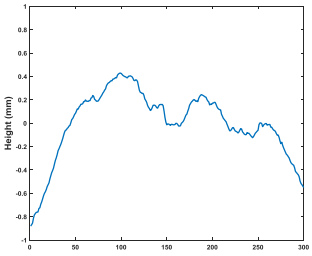	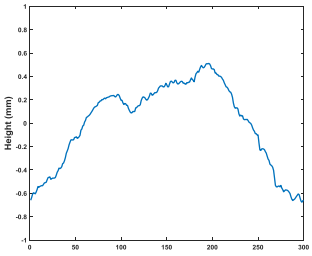
Quarry # 2			
Non-Polished	Particle #1	Particle #2	Particle #3
	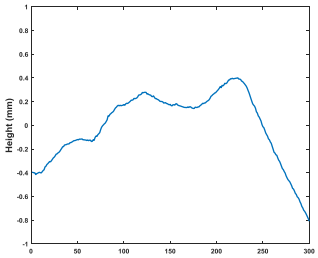	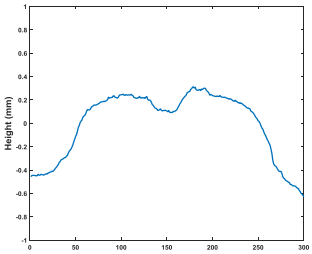	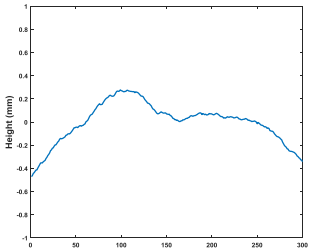
Polished	Particle #4	Particle #5	Particle #6
	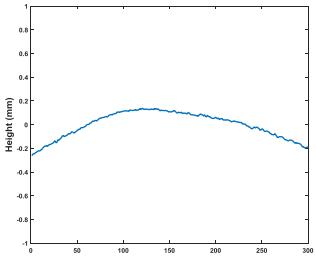	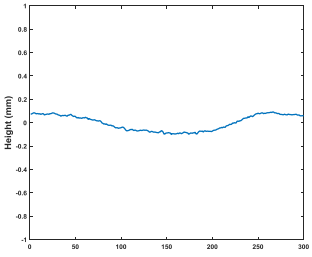	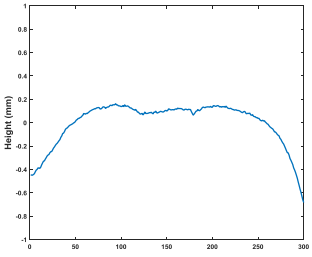

Table 7.3: Continued

Quarry # 3			
Non-Polished	Particle #1	Particle #2	Particle #3
	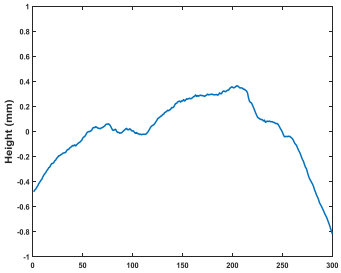	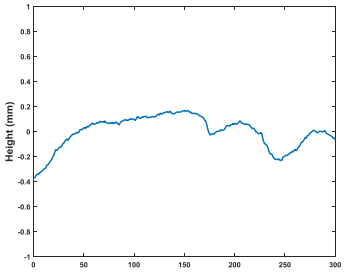	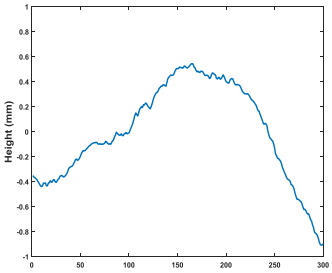
Polished	Particle #4	Particle #5	Particle #6
	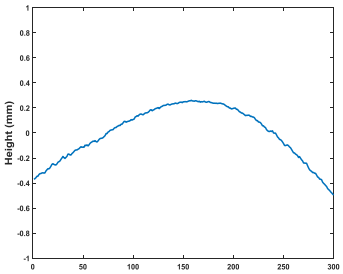	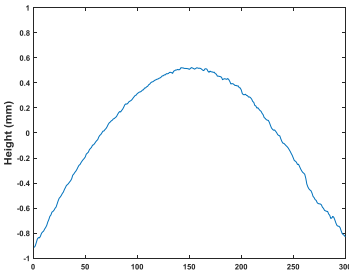	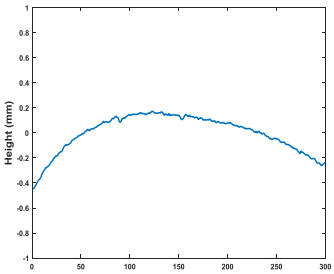
Quarry # 4			
Non-Polished	Particle #1	Particle #2	Particle #3
	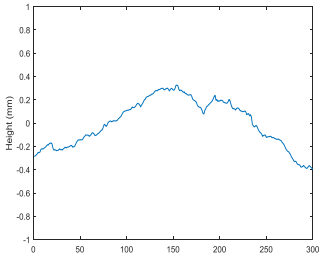	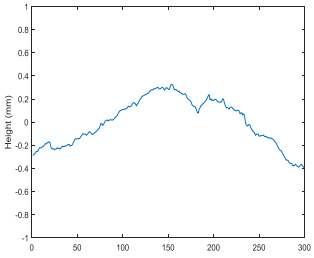	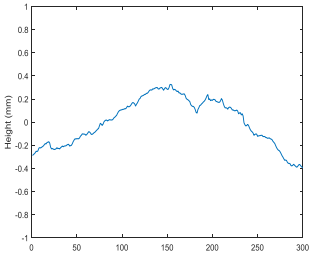
Polished	Particle #4	Particle #5	Particle #6
	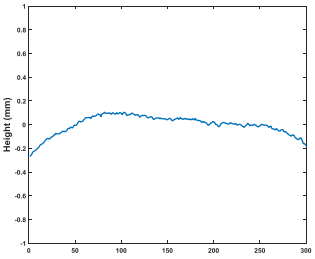	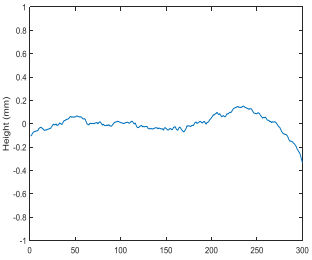	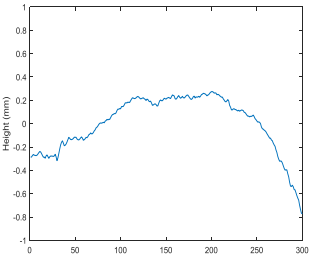

Table 7.3 Continued

Quarry # 5			
Non-Polished	Particle #1	Particle #2	Particle #3
	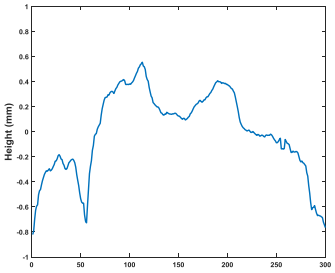	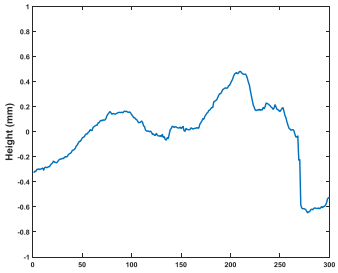	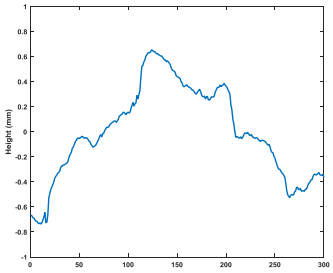
Polished	Particle #4	Particle #5	Particle #6
	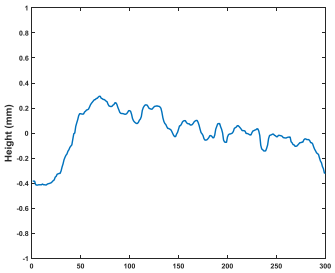	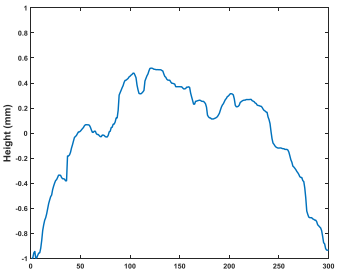	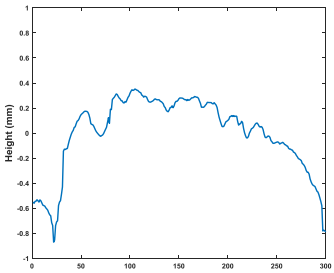
Quarry # 6			
Non-Polished	Particle #1	Particle #2	Particle #3
	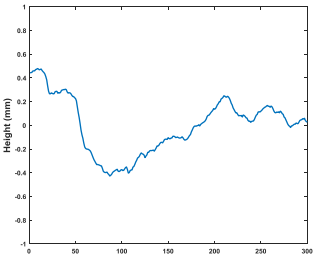	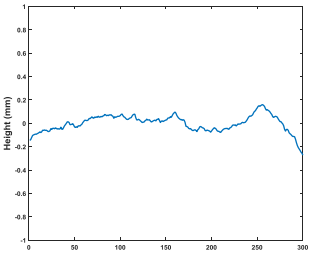	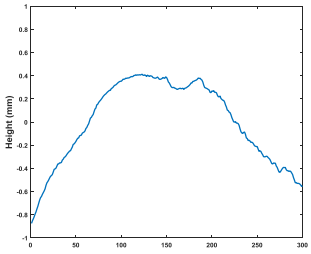
Polished	Particle #4	Particle #5	Particle #6
	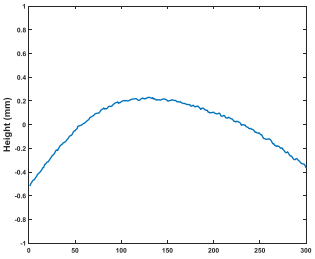	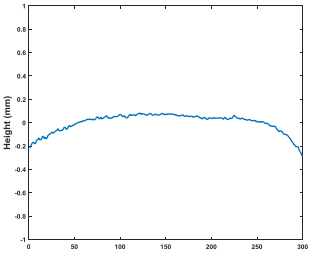	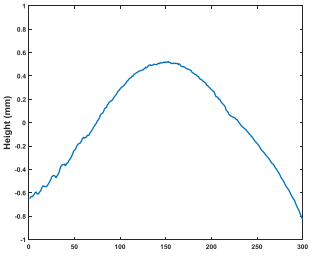

Table 7.3: Continue

Quarry # 7			
	Particle #1	Particle #2	Particle #3
Non-Polished	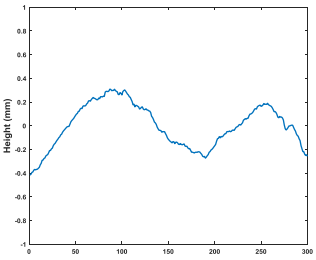	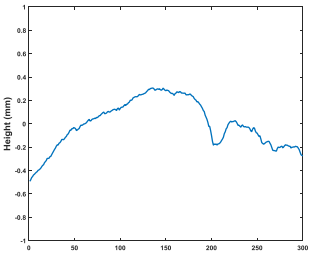	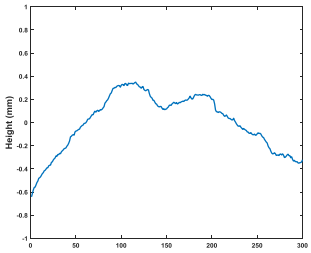
	Particle #4	Particle #5	Particle #6
Polished	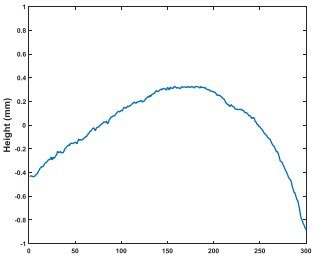	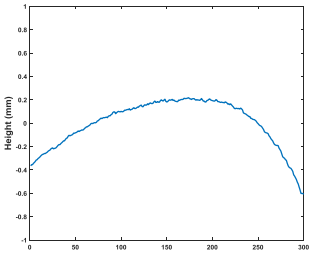	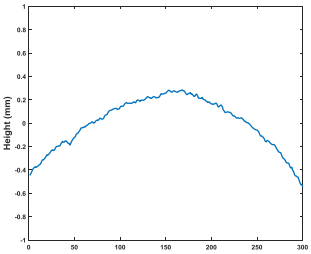

Table 7.3: Examples of Surface Height Profiles.

The above-described texture parameters were calculated for each profile. The algorithms for calculation of the statistics were generated in MATLAB. For each aggregate, the mean of the parameters derived for the thirteen profiles was determined. Figure 7.5 through 7.9 shows the boxplots of the measured parameters for seven quarries non-polished and polished samples. These plots illustrate the range and variations of the texture parameters of aggregate samples. Besides, the mean value of each group is shown with an "X" mark. Two primary differences are of interest. The difference between the quarries and the difference between polished and non-polished groups. As seen in these figures, aggregate samples from quarry #5 have the widest spread in all texture statistics except the RMS. It should be noted that in each boxplot, quarries are arranged according

to the amount of drop. For all texture parameters except the MPD, some quarries revealed a negative drop which means the average value of the parameters increased after polishing. For instance, the box plot of the δ_q (Figure 7.9) shows a negative drop for the aggregate samples from quarry #1. According to the definition of this parameter, higher roughness should be expected when the δ_q is higher. A negative drop indicates that the grains of aggregate particles break during the polishing and produce fresh surface texture.

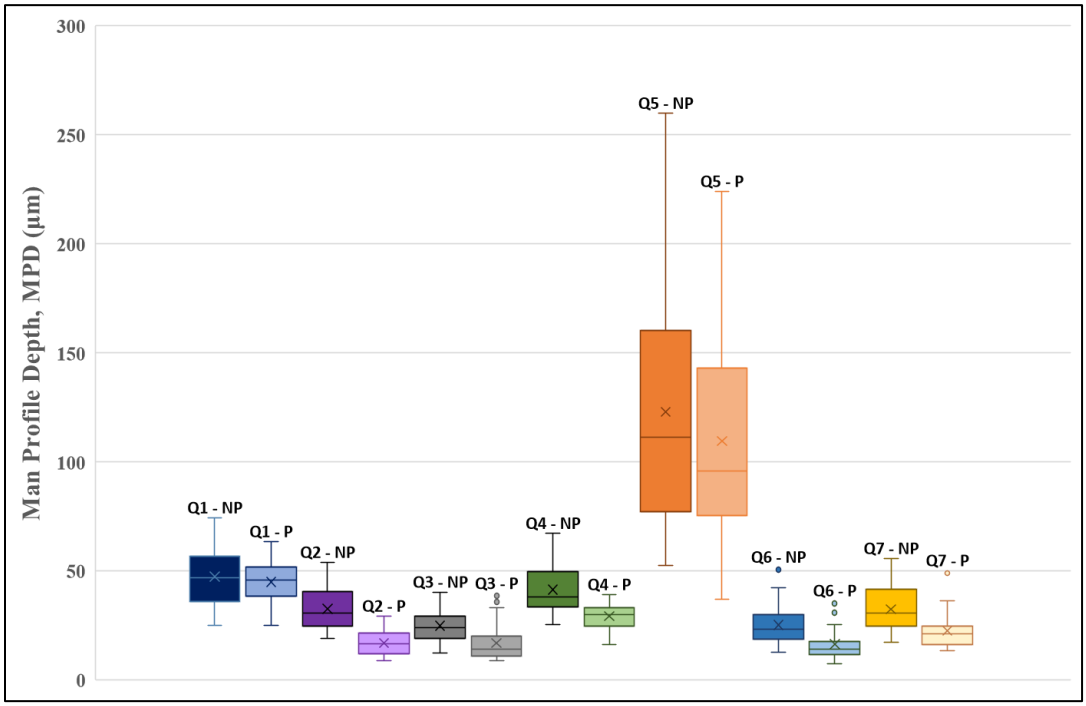

Figure 7.5: Box Plot of the Mean Profile Depth.

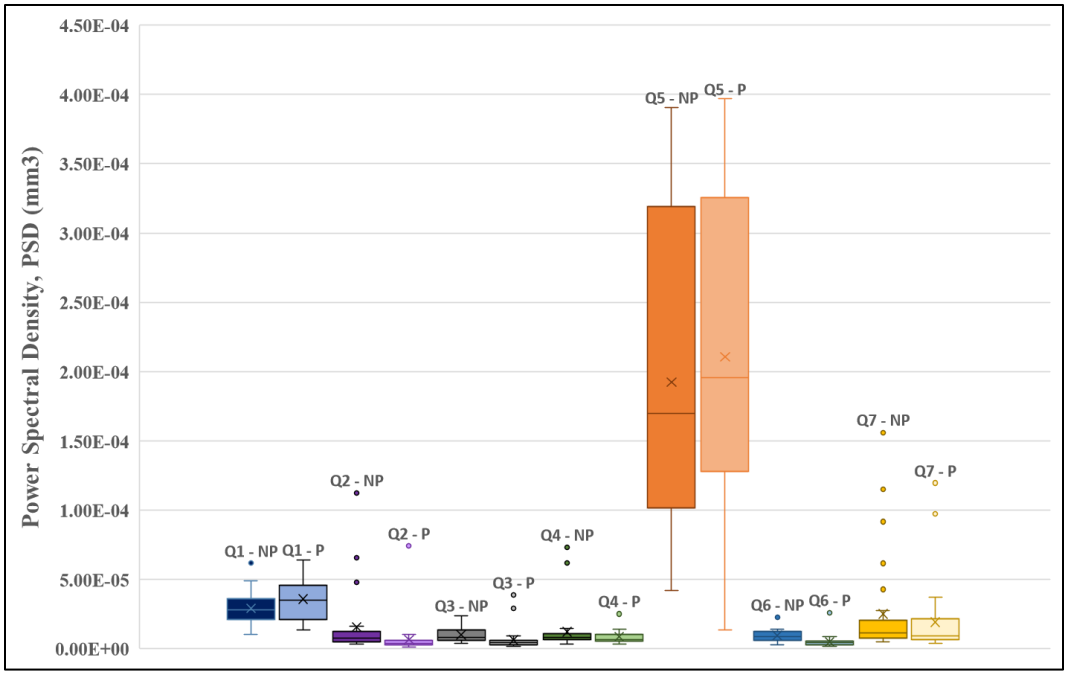

Figure 7.6: Box Plot of the Power Spectral Density.

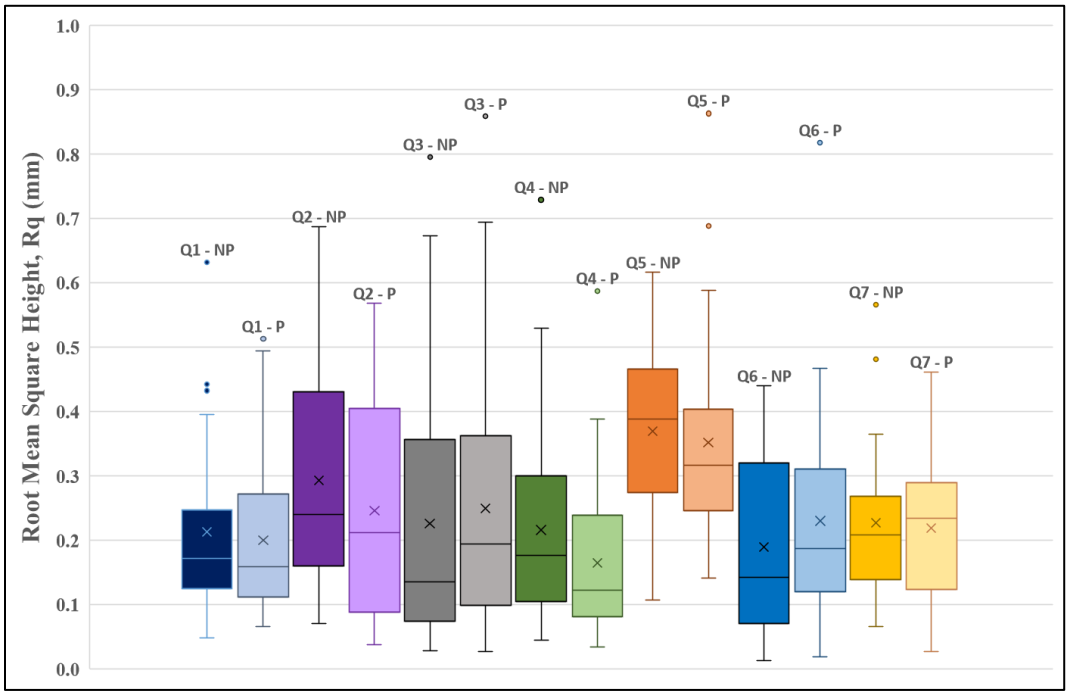

Figure 7.7: Box plots of the Root Mean Square Height.

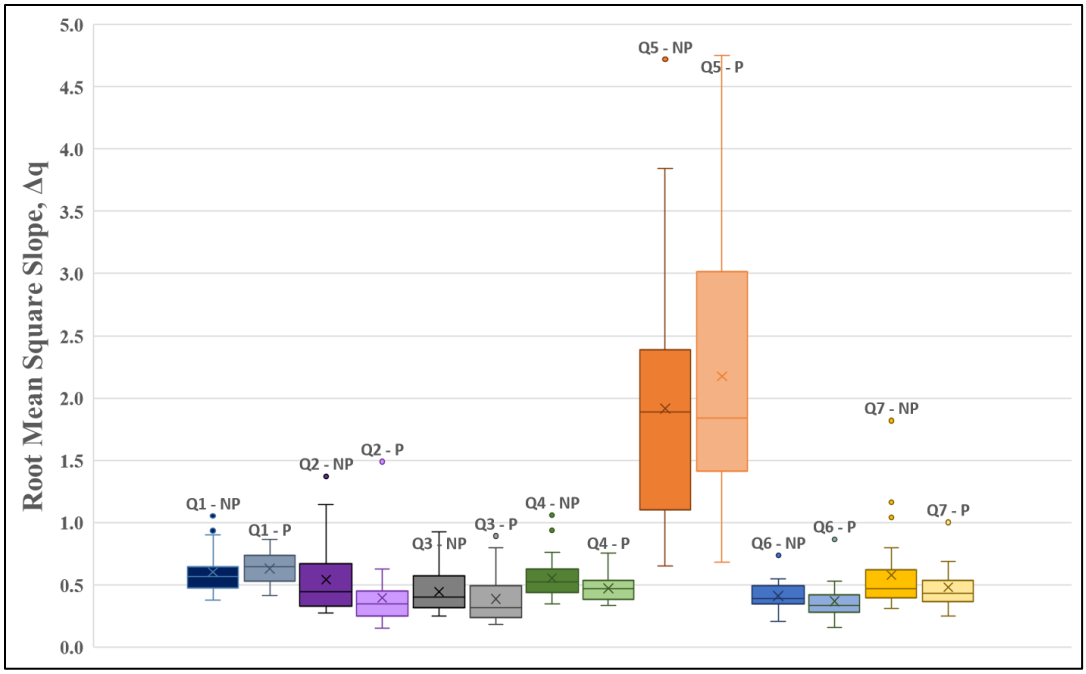

Figure 7.8: Box Plot of the Root Mean Square Slope of the Profile.

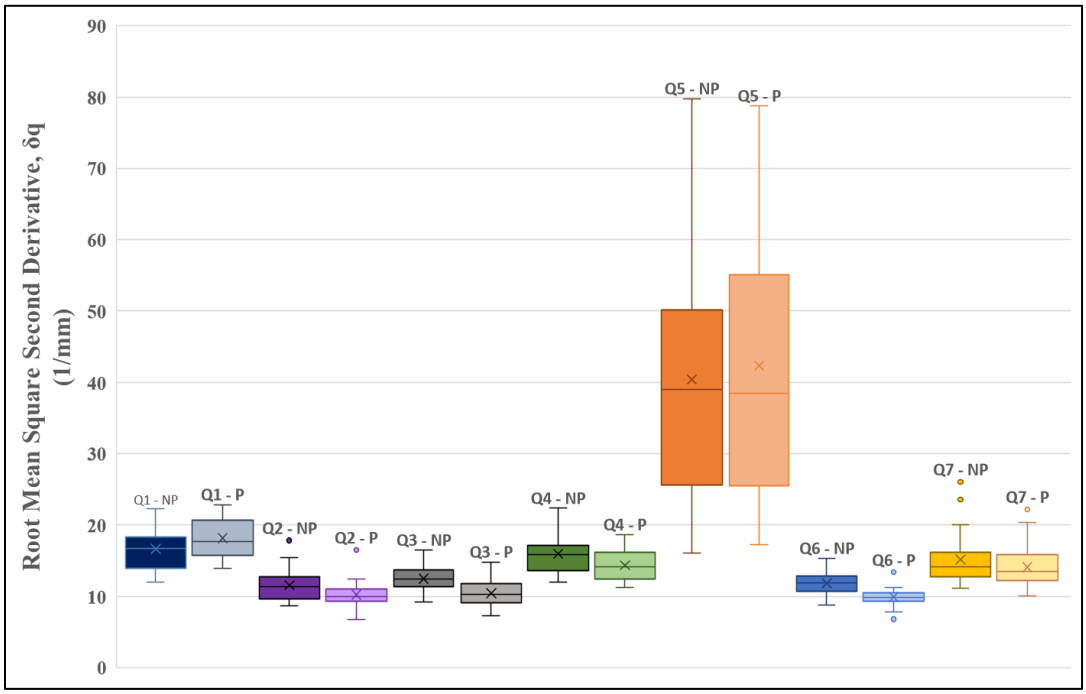

Figure 7.9: Box Plot of the Root Mean Square Second Derivative of the Profile.

Comparing Aggregates Durability Measurements with Texture Statistics

This research study intended to group aggregate particles based on their texture change after polishing. To do so, it was decided to choose two of the statistics as classifiers. The representative values of investigated texture parameters for each quarry were determined by the difference between the averages of polished and non-polished aggregates. These measurements were compared to the testing results obtained from measurements done in the TxDOT laboratory. Table 7.4 presents these comparisons. Among the height parameters, MPD and PSD showed a better correlation to aggregate durability parameters. From shape parameters, δ_q presents a stronger correlation to the durability measurements. It should be mentioned that these comparisons are based on the results of seven quarry aggregates.

	MDML (%)	MSL (%)	AIR (%)
PSD	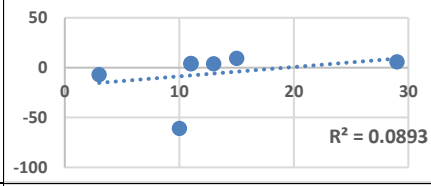	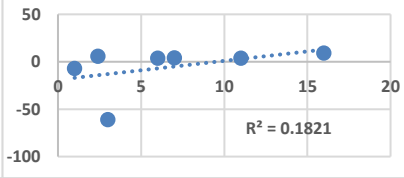	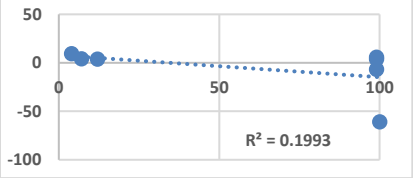
R_q	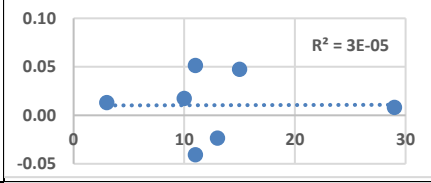	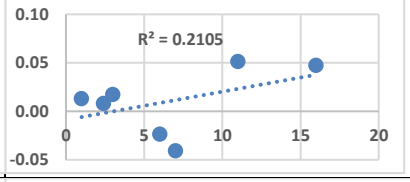	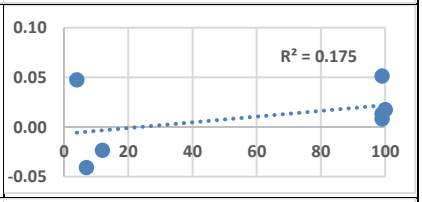
Δ_q	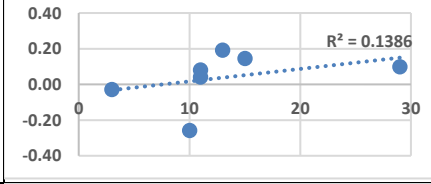	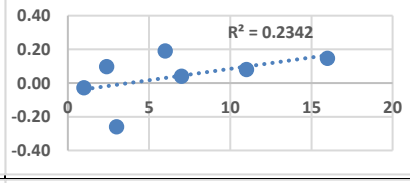	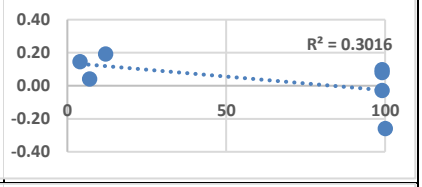
δ_q	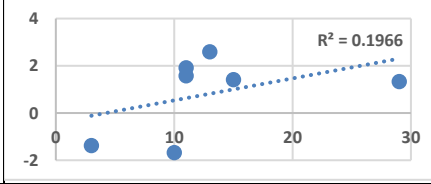	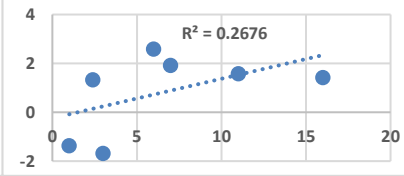	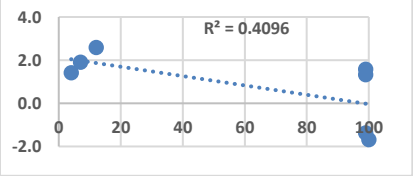
MPD	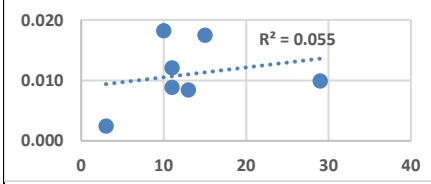	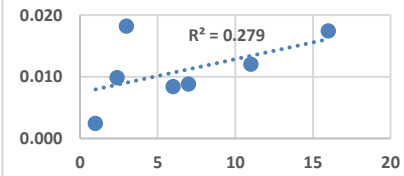	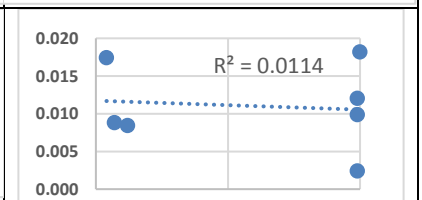

Table 7.4 Plots of Aggregate Texture results vs. Durability Measurements.

CLUSTERING ANALYSIS

This research employed a clustering analysis technique to group aggregates into acceptable and non-acceptable groups for friction purposes. This clustering is based on the drop level of the MPD and δ_q parameters. For this purpose, the model-based clustering technique was used. In the following sections, first the model-based clustering

technique and then the steps to develop the clustering model are explained. Afterward, the results of the aggregate particles clustering model are provided.

Model-based Clustering Technique

Model-based clustering involves statistical concepts and views the observations as random variables generated from a probability distribution (*Chamroukhia, 2015*). Data is assumed to come from a mixture of K distributions, where each distribution represents a cluster. For example, assume $y = \{y_1, y_2, \ldots, y_n\}$ is a sample of observations of size n, where y_i $(for\ i = 1,2,\ldots,n)$ is a p-dimensional observation. As shown in Equation 7.4, model-based clustering considers the density function of the observations as a weighted sum of K density functions. Commonly, the Gaussian mixture model is the used model for multivariate real data where each component is a Gaussian distribution with its own mean and variance (*Diebolt, 1994*). In other words, the Gaussian mixture model identifies each cluster with one of its Gaussian components.

$$\boldsymbol{f(y_i) = \sum_{k=1}^{K} w_k N_k(y_i|\mu_k, \varepsilon_k)} \qquad \boldsymbol{i = 1, 2, \ldots, n} \qquad \textbf{Eq 7.4}$$

Where

y: p-dimensional observations,

w_k: mixing proportion or weight of each distribution such that $0 < w_k < 1$, $\sum_{k=1}^{K} w_k = 1$,

f_k: mixture components, and

K: number of mixture components.

Fitting a mixture model to data can be interpreted as finding clusters by using mixture components. Along with the means (μ) and covariances (Σ) of clusters, the

mixing weight for each cluster (w), and the classification vector, Z = (z_1, $z_{2, \ldots,}$ z_n), need to be estimated. The vector Z indicates the component observation y_i belongs.

Bayesian Inference

Bayesian inference was used in this study to estimate the parameter of the clustering model. Bayesian estimation is implemented based on the Bayes theorem (which is shown in Equation 7.5). According to this theorem, there is an initial guess on the probability distribution of the parameter which is called prior and reflects our knowledge regarding the parameter before observing the data. This prior distribution is updated by the likelihood function of data and turns into a new probability distribution which is called posterior distribution (*Heller 2007*).

$$\boldsymbol{p(\theta|y) \propto p(\theta)p(y|\theta)} \qquad \textbf{Eq 7.5}$$

where

$p(\theta)$ is prior distribution,

$p(y|\theta)$ is the likelihood function, and

$p(\theta|y)$ is the posterior distribution.

In this research study, the parameter $\boldsymbol{\theta}$ is a set of means of Gaussian distributions (μ), covariances of Gaussian distributions (Σ), weights of Gaussian distributions (w), and the classification vector (Z). To apply Bayesian inference, priors on θ must be defined. For convenience, conjugate priors are often used. For a mixture of Gaussian distributions, components' mean, $\{\mu\}_{k=1}^{K}$, can be assigned a vague Normal prior (e.g., centered at zero with a covariance (Σ_k)) whilst covariances $\{\Sigma\}_{k=1}^{K}$ can be assigned a

vague inverse Wishart distribution. The prior distribution for weight parameters, w, is a Dirichlet distribution; $(w_1, w_2, \ldots, w_k) \sim Dirichlet(\alpha_1, \alpha_2, \ldots, \alpha_k)$. The Dirichlet distribution is a multivariate distribution and is used where k $\geq$ 2.

According to Bayesian inference, a joint posterior distribution over the set of unknown parameters is needed, i.e., $p(\mu, \Sigma, w, Z|y)$. By sampling from the joint posterior distribution, any features such as moments can be obtained. A Gibbs sampling algorithm, which is a Markov Chain Monte Carlo (MCMC) algorithm, was codded (Appendix A) to construct the joint posterior distribution of the model parameter. The Gibbs sampler iteratively generates samples from full conditional posterior distributions of the individual parameters. This algorithm makes the process approach the equilibrium which means that the sample values have the same distribution as if they were sampled from the true posterior joint distribution (*Yildirim, 2012*).

Conditional posterior distributions

The following expressions give the full conditional posterior distribution of means and covariance matrices:

$$\boldsymbol{p(\mu_k|\mathbf{y}, \Sigma_k, \mathbf{Z}) \sim \mathbf{N}\left(\frac{s_k}{n_k + 1}, \frac{\Sigma_k}{n_k + 1}\right)} \qquad \textbf{Eq 7.6}$$

where

n_k is the number of observations allocated to component k,

s_k is the sum of the value of the observations allocated to component k.

$$\boldsymbol{p(\Sigma_k|y, \mathbf{Z}) \sim inverse - Wishart\ (a + n_k\ ,\ b\ + \Lambda_k\ +\ \frac{n_k}{n_k + 1}\ (\bar{y}_k\ -\ 1)(\bar{y}_k - 1)^T} \qquad \textbf{Eq 7.7}$$

where

n_k is the number of observations allocated to component k,

a and b are the parameters of the prior inverse Wishart distribution,

$\Lambda_k = \sum_{k \epsilon K}(y_{ik} - \bar{y}_k)(y_{ik} - \bar{y}_k)^T$,

$\bar{y}_k$ is the mean of the values of the observations allocated to component k,

y_{ik} is the value of an observation allocated to component k.

For the weight parameter, w, the full conditional is a Dirichlet distribution with parameters $(\alpha_1 + n_1, \alpha_2 + n_2, \ldots, \alpha_k + n_k)$. The full conditional distribution for classification vector Z is a discrete distribution which can be stated by Equation 7.8.

$$\boldsymbol{p(z_i|\mathbf{w}, \boldsymbol{\mu}, \boldsymbol{\Sigma})} = \frac{\boldsymbol{w_k f_k(y_i|\mu_k, \Sigma_k)}}{\sum_{\boldsymbol{k=1}}^{\boldsymbol{K}} \boldsymbol{w_k f_k(y_i|\mu_k, \Sigma_k)}} \qquad \textbf{Eq 7.8}$$

Gibbs Sampler Algorithm

Following provides the steps to run the Gibbs sampler algorithm using the full conditional posterior distributions:

Step 1: Assign initial values to μ, Σ, w, Z: $(\mu^{(0)}, \Sigma^{(0)}, w^{(0)}, Z^{(0)})$,

Step 2: For i = 1,2, …N repeat

a. Draw sample $\Sigma^{(i)} \sim$ p $\left(\Sigma \middle| y, Z^{(i-1)}\right)$

b. Draw sample $\mu^{(i)} \sim$ p $(\mu|\mathrm{y}, \Sigma^{(i)}, Z^{(i-1)})$

c. Draw sample $\omega^{(i)} \sim$ p $\left(\omega \middle| Z^{(i-1)}\right)$

d. Draw sample $Z^{(i)} \sim$ p $(z_{ik}|\, \mu^{(i)}, \Sigma^{(i)}, \omega^{(i)})$

For an inadequate number of iterations, the simulations might be unrepresentative of the posterior distribution. After enough number of iterations, Gibbs sampling will

provide samples from the joint posterior distribution of (μ, Σ, w, Z). Bayesian estimation will be based on these samples. The early iterations must be discarded from the analysis since they are influenced mainly by the initial values rather than the posterior distribution. To determine the appropriate number of iterations, different numbers were tried in this study, and the convergence of the sampling was evaluated. Convergence is assumed when the sampling of all parameters seems to have reached the stationary regime. Based on the history plot of the Markov chain for parameters, one can judge practical convergence of the chain. By using these plots, we can see whether the value of a parameter jumps in certain areas or it follows a straight path (*Faranzen, 2006*).

Running the Clustering Algorithm on an Artificial Data

The Gibbs sampler algorithm explained above was first tested on several generated datasets. Results of these evaluations are presented in the next subsections.

Case Study 1

An artificial dataset which consists of 1,000 data points were simulated from five two-dimensional Gaussian distributions with different mean vectors (μ_k) and covariance matrices (Σ_k). Data is shown in Figure 7.10.

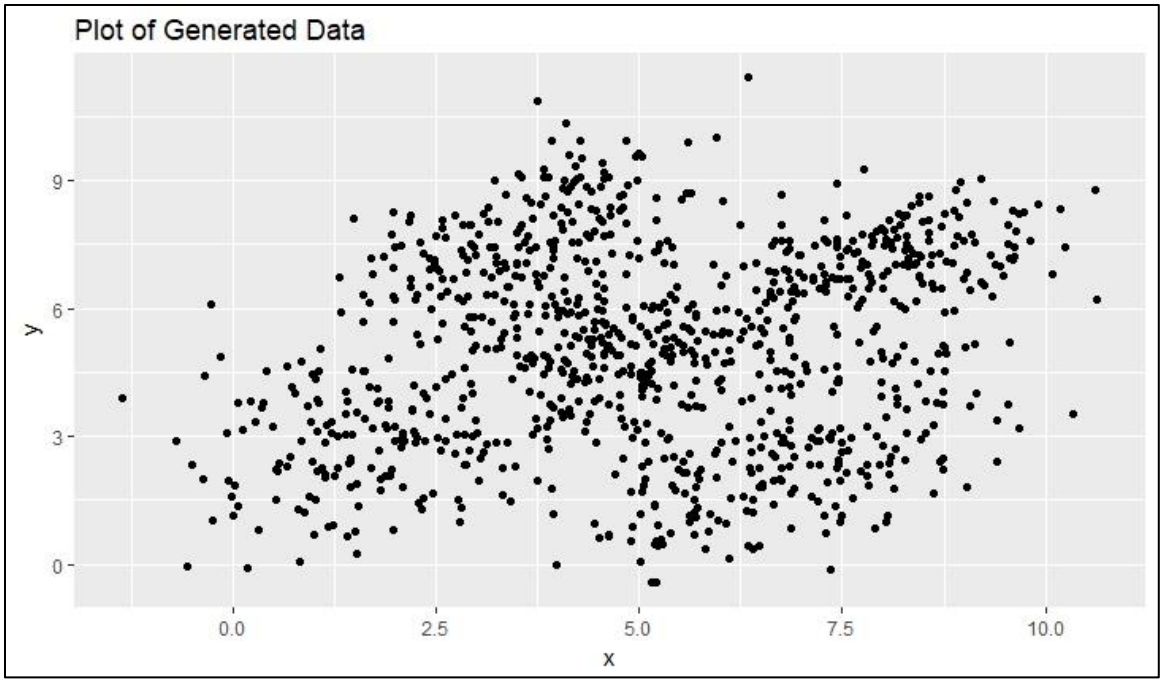

Figure 7.10: Plot of Data Generated from Five Gaussian Distributions.

In the Gibbs sampler algorithm, the number of clusters K is given a fix number, for example, any number greater than one. The process of sampling was set to be repeated for 2,000 iterations. At each time, one sample of parameters is drawn, and a clustering of data is produced. Accordingly, in the end, 2,000 clusterings of data are obtained. The method developed by Dahl (2006) can be employed to select the appropriate clustering. For each clustering $\boldsymbol{c}$ in $\boldsymbol{c}_1, \ldots, \boldsymbol{c}_{2000}$, an association matrix $\delta(\boldsymbol{c})$ of dimension n × n (where n is the number of the data) is created. The element (i, j) of this matrix indicates whether data i is clustered with data j or not. Then, a matrix called the pairwise probability matrix ($\hat{\pi}$) is calculated by taking an element-wise average of $\delta(\boldsymbol{c})$ matrices. The clustering $\boldsymbol{c}^*$ is selected which minimizes the sum of squared deviations of its association matrix $\delta(\boldsymbol{c})$ from the pairwise probability matrix $\hat{\pi}$:

$$c^* = \boldsymbol{argmin} \sum_{i=1}^{G} \sum_{j=1}^{G} (\boldsymbol{\delta}_{i,j}(c) - \hat{\boldsymbol{\pi}}_{i,j})^2 \qquad c \in \{c_1, \dots, c_{2000}\} \qquad \textbf{Eq 7.9}$$

The clustering results of the generated data are shown in Table 7.5. In each case, ellipses were drawn to represent the standard deviation around the mean of clusters. in real applications the number of clusters is unknown. Given a set of data points, one can select the number of clusters based on the application or find the optimum number of clusters by using statistical tools. Spiegelhalter et al., 2002 suggested using the Deviance Information Criterion (DIC) to find the optimum number of clusters. The calculation of this parameter is given in Equation 7.10. Models with smaller DIC values are preferred over models with larger DIC. In this case, a different number of clusters $2 \leq K \leq 7$ were examined even though it is already known that the dataset built by five Gaussian distributions. Figure 7.11 presents the plot of DIC versus the number of clusters. Clustering data in five groups resulted in the smallest DIC value.

$$\mathbf{DIC} = \hat{\boldsymbol{D}} + \boldsymbol{P_D}$$

$$\mathbf{D}(\mathbf{y}, \boldsymbol{\theta}) = -2 \log[\mathbf{p}(\mathbf{y}|\boldsymbol{\theta})]$$

$$\hat{\boldsymbol{D}} = \boldsymbol{E}(\mathbf{D}(\mathbf{y}, \boldsymbol{\theta})|\mathbf{y})$$

$$\boldsymbol{P_D} = \hat{\boldsymbol{D}} + 2\, \boldsymbol{log}\, [\boldsymbol{p}(\boldsymbol{y}|\bar{\boldsymbol{\theta}})]$$

$$\bar{\boldsymbol{\theta}} = \boldsymbol{E}\,(\boldsymbol{\theta}|\mathbf{y}) \qquad \textbf{Eq 7.10}$$

where

DIC: deviance information criterion

y: vectors of observations

θ: vector of mixture model's parameters

p(y|θ): likelihood function

D(.): deviance

P_D: posterior mean deviance - deviance of posterior means.

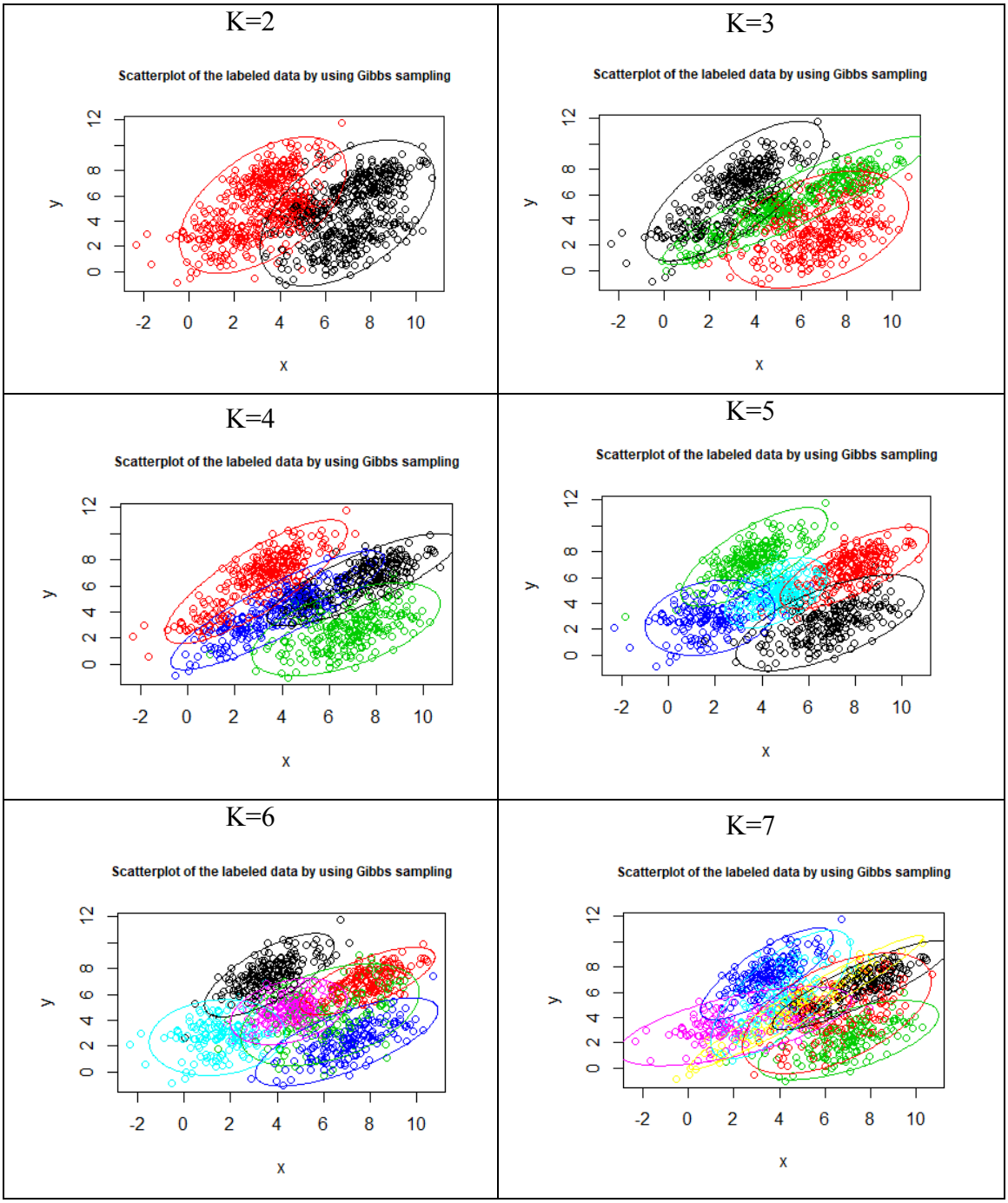

Table 7.5: Results of Clustering on Generated Data.

Figure 7.11: Plot of DIC vs. Number of Clusters.

Table 7.6 compares the Bayesian estimate of the mean and covariance of obtained five clusters with their actual values. All mean and covariance values estimated fairly close to the actual values. The history plot of means, weights, and covariances were also examined. The plots showed that the convergence was rapidly attained for the parameters. Figure 7.12 presents the history plots of means.

True Mean	**Mean Obtained by Clustering**	**True Covariance**	**Covariance Obtained by Clustering**
(5,5)	(5.1,4.9)	(0.7,0,0,0.8)	(0.5, 0, 0, 0.7)
(8,7)	(7.8,7)	(1,0.5,0.5,1)	(1, 0.6, 0.6, 1)
(3.5,7.5)	(3.6,7.5)	(1.2,0.9,0.9,1.7)	(1.2, 0.8, 0.8, 1.5)
(2,3)	(1.8, 2.9)	(2,0.5,0.5,2)	(1.8, 0.3, 0.3, 2.3)
(7,2.5)	(6.8,2.8)	(1.8,0.9,0.9,1.5)	(1.7, 0.6, 0.6, 1.6)

Table 7.6: Comparing the Clustering Results to True Means and Covariances.

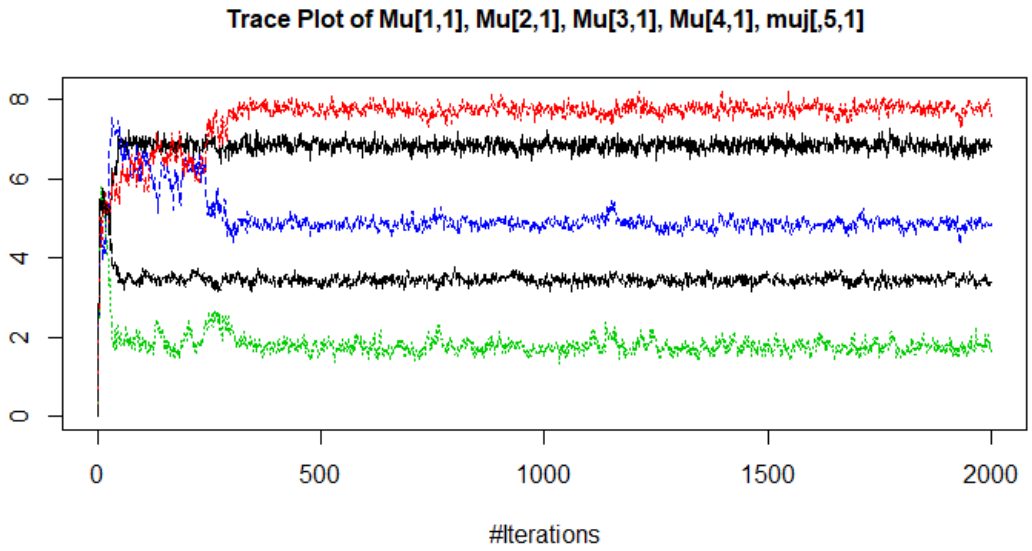

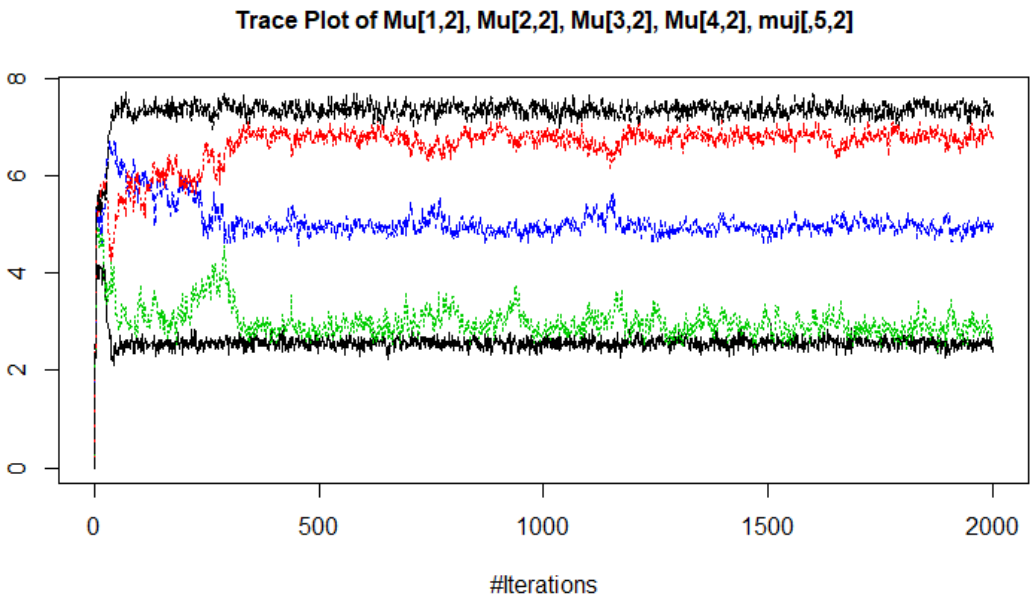

Figure 7.12: History plots of Clusters Mean.

Case study 2

In this case, the generated dataset consists of 200 data points simulated from four two-dimensional Gaussian distributions with different mean vectors (μ_k) and covariance matrices (Σ_k). As shown in Figure 7.13(a), the mean of Gaussian distributions was chosen so that the four groups of data are spaced apart. The developed algorithm was run on this dataset to find the four clusters. The clustering result for this case is tabulated in Figure 7.13(b).

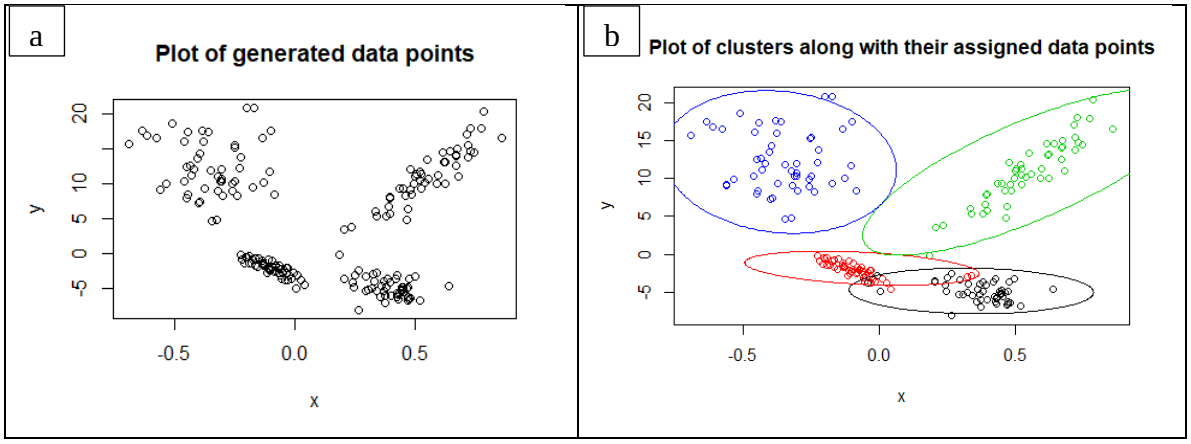

Figure 7.13: Plot of Generated Data and Results of Clustering for Case Study 3.

Case study 3

So far, case studies 1 and 2 showed that, the developed clustering algorithm could identify the clusters within the data with different shapes and direction. In this case study, similar to the case study 2, a dataset consists of 200 data points was generated from four Gaussian distributions; however, the mean of four distributions was chosen closer to each other (as shown in Figure 7.14(a)). In this case, although the data points were generated from four Gaussian distributions, the results (Figure 7.14(b)) showed that the optimum

number of clusters might be three which could be due to the overlapping data and small dataset.

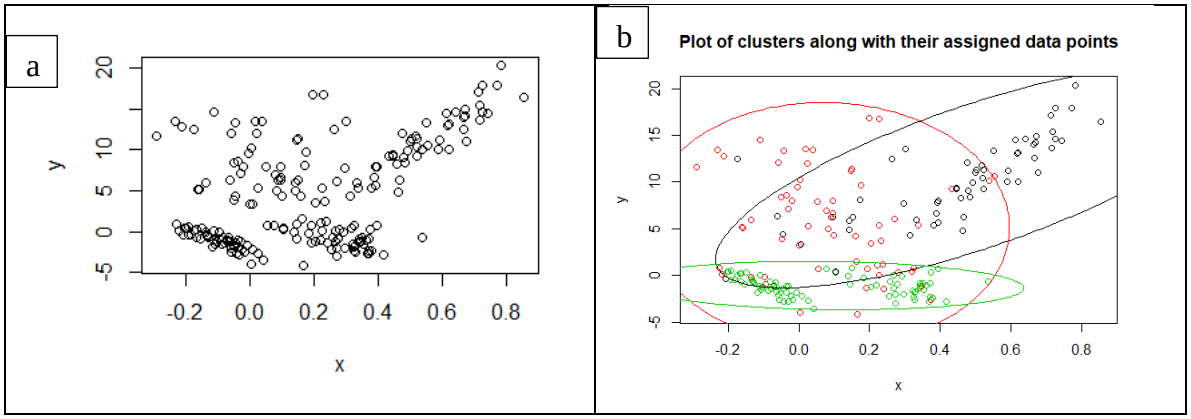

Figure 7.14: Plot of Generated Data and Results of Clustering for Case Study 3.

Clustering Aggregate Particles

Mentioned previously, the objective of this study is to classify aggregate particles based on their polishing resistance. By using the model-based clustering technique, aggregates can be classified into several groups such that aggregates in the same group have similar frictional properties. Two parameters – drop level of the MPD and δ_q – were selected from the analysis of texture parameters in order to characterize the evolution of the surface texture after polishing.

Given the parameters chosen, the classification of aggregates into four ideal groups is assumed. A rough representation of these four groups is shown in Figure 7.15. Each group of aggregates can be used for different applications based on the needed friction level. For instance, zone A represents aggregates with the lowest drop in both values of MPD and δ_q which means these aggregates are more resistant against the polishing. On the other hand, zone D includes aggregates with the lowest level of

resistance which should be avoided in the pavement surfacing. Aggregates in zone B and C represents aggregates with mid-level of polishing resistance. In order to use these aggregates in the pavement surfacing application, several factors need to be considered. For instance, aggregates in zone C show a higher drop in the MPD that means that by polishing, the depth level of their texture decreases significantly hence the risk is high to use these aggregates in rainy regions. Zone B represents aggregates that lose their texture roughness by being exposed to traffic. In fact, by polishing, these aggregates would lose their ability to create the adhesion component of the friction and hence they must be avoided in the high-speed regions.

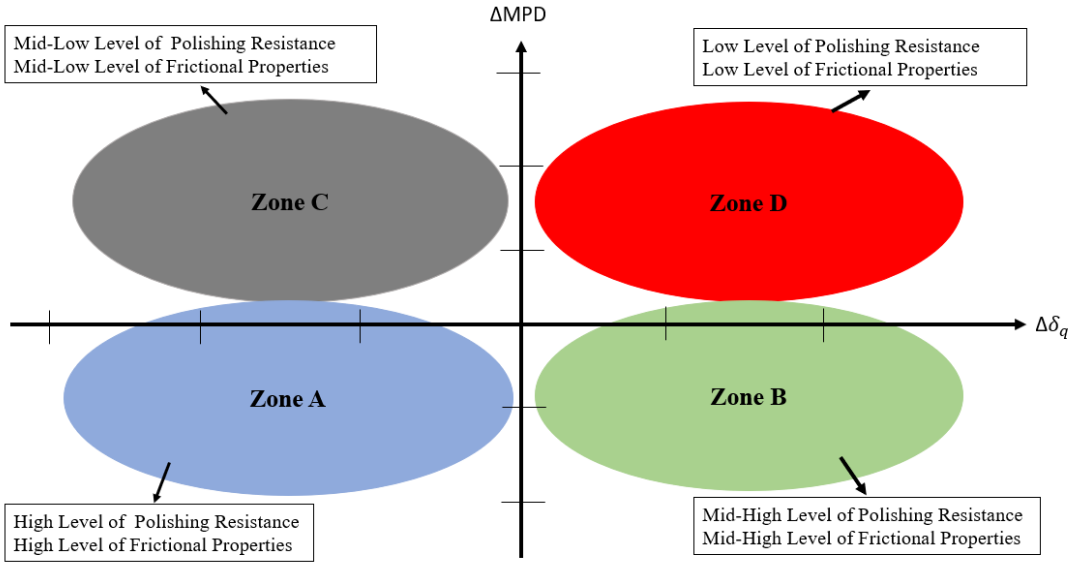

Figure 7.15: A Rough Representation of Ideal Clusters for Aggregates based on the Selected Parameters.

In this section, the model-based clustering technique, discussed in the previous section, was applied to aggregates data to find the four clusters. The result of clustering

of aggregate is shown in Table 7.7. It needs to be mentioned that this clustering is based on the data from seven quarry aggregates. By considering more different quarry aggregates a better clustering boundaries might be achieved. In Figure 7.16, the plot of the average of ΔMPD and $\Delta\delta q$ for chosen seven quarry aggregates is provided. Comparing this plot to the result of clustering (Table 7.7) shows that the blue cluster includes quarry #1. The aggregates that fall in this cluster can ensure high skid resistance pavements. The black cluster captures quarry #5. This cluster represents zone C. Quarry #2 falls in the red cluster (Zone D) and quarries #3, #4, #6, and #7 are classified in the green cluster (Zone B).

Mentioned previously, that AIR tests are vital in the TxDOT's aggregate classification in deciding the polishing and frictional properties of aggregates. However, this test limits the usage of carbonate aggregates in the pavement surfacing. The AIR test results (Table 7.1) performed for the seven quarry aggregates showed that quarries #2, #3, and #6 contain a significant amount of carbonate and hence are not appropriate to be used for the surfacing according to the TxDOT's classification. However, the results of this research revealed that among these three quarry aggregates, #3 and #6 maintained the depth level of their surface texture well after the polishing. Therefore, the usage of these aggregates could help in the drainage of the water from the surface and thus prevent hydroplaning.

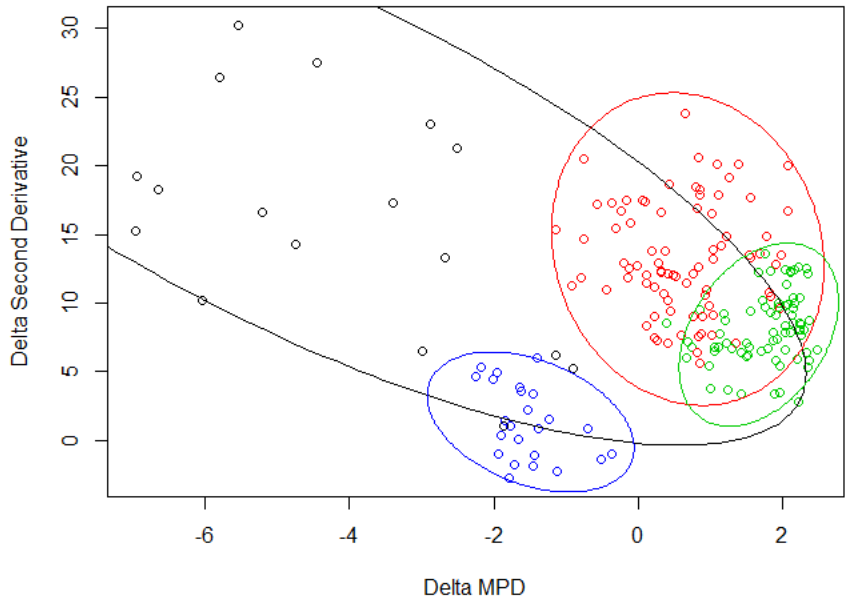

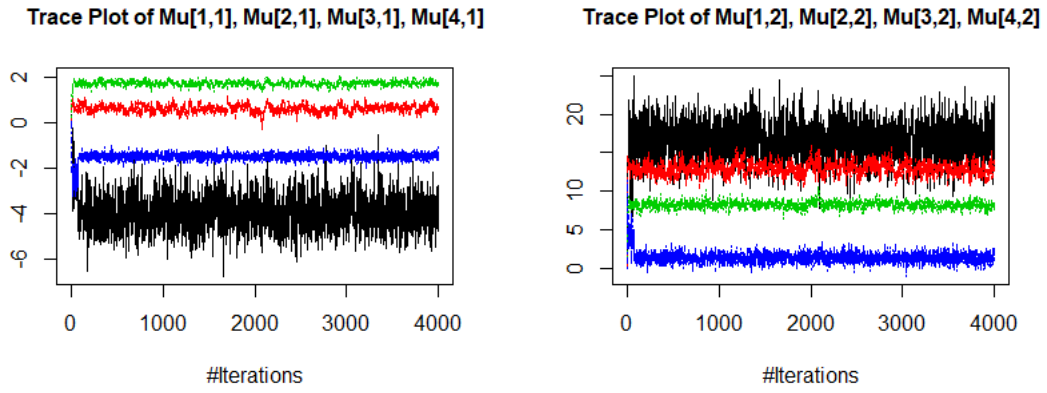

Cluster	Blue	Green	Black	Red
Mean	(-1.5, 1.4)	(1.7, 8.3)	(-3.9, 16.4)	(0.6, 13)

Table 7.7 Results of Aggregate Clustering.

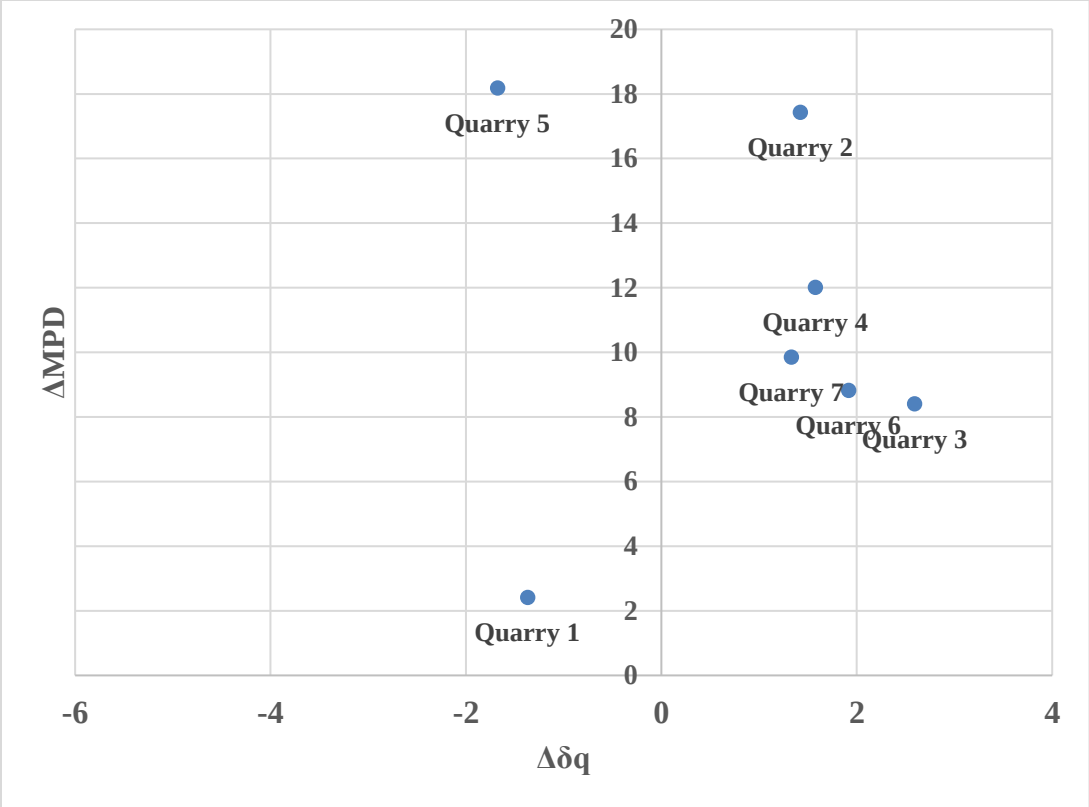

Figure 7.16: Plot of the ΔMPD versus $\Delta\delta q$ for the Chosen Seven Quarry Aggregates.

SUMMARY

Aggregates with various mineralogy show different polishing and retention behavior. It is essential to make sure that aggregates to be used in the pavement surfacing are resistant under the polishing effect of traffic. This aspect should be taken into account at the stage of pavement design to optimize the skid resistance.

In this chapter, the LLS prototype was used to compare the surface texture of non-polished aggregates with the surface texture of the polished aggregates to observe changes in the surface texture due to polishing. Analysis of surface profiles taken from

aggregate surfaces as they were polished demonstrated that changes in the height amplitude and roughness of texture could be connected to their polishing resistance. An algorithm capable of classifying the aggregate particles was built by using statistical methods. This algorithm can be used to evaluate aggregates in terms of their textural polishing properties. This classification method would lead to a considerable improvement in the pavement surface friction, reducing road accidents, and a substantial cost saving for both highway agencies and drivers.

Chapter 8: Conclusion, Applications, and Recommendations

CONCLUSIONS

Wet-weather highway accidents are a major concern for pavement engineers and transportation agencies worldwide and in particular in Texas. Road safety studies indicate that approximately 15% to 35% of all highway accidents happen during wet-weather where skidding of the vehicles is one of the main contributor. Hence, assessing wet-weather pavement skid resistance is vital for highway agencies. The literature review conducted as part of this dissertation revealed that the resistance to sliding and skidding can be increased by adjusting the pavement surface texture. The pavement surface texture is composed by asperities of various sizes grouped into four scales: unevenness, megatexture, macrotexture, and microtexture. Macro and microtexture directly impact on the pavement skid resistance. Microtexture refers to texture features with wavelength of less than 0.5 mm and is a function of the aggregate source, mineralogy and production process. Macrotexture refers to the texture features with wavelengths in the range of 0.5 – 50 mm and is a function of aggregate size and particles' arrangement within the surface layer. Proper mix design accounting for pavement microtexture is achieved by accurately measuring the aggregates texture properties. Besides, regular measurement of macrotexture during the service life of pavements aid in maintaining the surface friction at an acceptable level. In an attempt to eliminate the limitations regarding measuring pavement surface texture, a series of experimental studies were performed to develop proper methodologies and algorithms. The main tasks undertaken in this research study are summarized as follows:

Laser Scanner Prototype

- In this study, a line laser scanner prototype – the LLS prototype – was developed and utilized to assess and describe the surface texture of pavements and aggregates.
- An efficient algorithm was developed for filtering the laser signal and removing the outliers from the data sets using signal and image processing techniques. This algorithm diminishes the number of erroneous points in the processed data, which significantly enhances the reconstruction quality of the 3D models of the pavement surface and aggregate particles.
- A technical approach to capture texture data using the LLS was applied in order to describe both micro and macrotexture.
- According to the repeatability analysis and standard deviation results, the LLS prototype was able to satisfactorily scan the surface profile within the first decade of microtexture (0.05-0.5 mm). However, it was observed that the data obtained in the second decade of microtexture (0.005-0.05 mm) was not reliable.
- An algorithm was established to solve the missing data in which the camera was not able to detect the laser line due to the limitations of the triangulation. The concept behind this algorithm rellies on scanning the object twice at two different angular positions, 0 and 180 degrees, and combining the two measurements.

Using LLS to Improve the Measurement of Pavement Surface Texture

- The efficiency and repeatability of the developed laser prototype were assessed through comparison to the Circular Track Meter (CTM) results in a field study. The study included testing three sites with different surface textures. The macrotexture components of the measured pavement surface profiles measured with the LLS prototype were extracted using spectral analysis to calculate the Mean Profile Depth

(MPD). The results of the repeatability analysis and standard deviation showed the high reliability of the developed LLS prototype for the texture measurement. In all the test sections, the MPD calculated from the LLS data was similar to that calculated from the CTM data.

- In this field study, the Grip-Tester was employed for friction measurements, and the relationship between the texture and friction of various pavement surfaces was investigated. The findings of the statistical analysis revealed a strong positive linear correlation between texture and friction for the pavements evaluated. The highest linear correlation coefficients (R) were observed between the Grip-Tester Numbers (GNs) obtained at 70km/h and texture data obtained using either the LLS or the CTM.
- According to the results of the field study, the developed LLS prototype is capable of providing an accurate and precise measurement of the pavement surface texture.
- In an attempt to eliminate the subjectivity of the operator and maintain the philosophy behind the sand patch test, a new, efficient and robust algorithm to measure the Mean Texture Depth (MTD) was also developed. A 3D model of the pavement surface is the input of this algorithm. The MTD algorithm consists of creating a virtual reference plane at the 94^{th} percentile value of the surface data. Then, the surface points below the reference plane are located. The distances between the points and the reference plane are calculated. The MTD of the scanned pavement is obtained by numerically integrating the volume between the measured surface and the reference plane. The field test results on six pavement sections with various surface textures proved the high repeatability of the proposed procedure. This method was also more consistent than the traditional sand patch test (SPT), faster, more practical to perform in the field and not affected by environmental conditions such as wind.

Using LLS to Improve the Characterization of Aggregate Surface Texture

- The variation of aggregates surface texture was investigated in this study. The evaluation was conducted using the surface profiles captured by the LLS. Power Spectral Density (PSD) analysis was undertaken with the aim of finding the variation of wavelength ranges of aggregate surface texture.
- Two different aggregate types, three particles from each type were used in this evaluation. The Texas Department of Transportation (TxDOT) provided aggregates. The selected aggregates belonged to two different TxDOT surface aggregate classification, herein referred as A and B.
- To study the effect of aggergate orientation on texture analysis, an aggregate particle was scanned in different orientations of 0°, 90°, 180°, and 270°. Comparison of PSD plots of data obtained at different orientations showed that the effect of aggregate orientation at the time of scanning is negligible.
- The PSD values of aggregate paticles obtained from the same source were found to behave similarly in the first decade of microtexture. Therefore, it was concluded that the aggregates PSD values in the first decade of microtexture are approximately consistent within a quarry.
- Based on the analysis conducted using the paired t-test, the PSD values of two different aggregate types vary in the first decade of microtexture. Thus, the first decade of the microtexture can be used to differentiate aggregate sources.
- The signals were processed in the space-domain by means of band-pass filters to separate the microtexture components from the macrotexture. The texture parameters of Rq and Rp calculated in different filtered profiles were consistent with the PSD values within the wavelength range of 0.05 to 0.25 mm.

- The results of PSD, Rp, and Rq were consistent with the Surface Aggregate Classification (SAC) provided by TxDOT in which the aggregate A exhibited higher frictional properties as compared to the aggregate B.
- The finding of this part of study revealed that the developed laser prototype showed promising results in terms of scanning the surface texture of aggregates and to use this information for classification purposes.
- The polishing resistance of seven different Texas aggregates were compared with surface texture measurements. The Micro-Deval apparatus and the LLS were utilized in this analysis. Following the polishing process, surface elevation profiles were obtained using the LLS and analyzed to determine the rate of change in the surface texture of aggregate samples. Analyses of surface texture measurements were carried out using a number of different texture parameters such as PSD, R_q, Δ_q δ_q, and MPD.
- Significant visual differences could be noted in particles texture before and after the polishing process. However, these differences were not being satisfactorily identified through the R_q, Δ_q. The other texture parameters, PSD, δ_q, and MPD worked reasonably well for differentiating among the texture change rate of different aggregate sources.
- Among the studied texture parameters, PSD, δ_q, and MPD showed a sensible correlation to the durability measurements of aggregate particles compared to R_q, Δ_q.
- A model-based clustering technique was used to group aggregates based on their texture and polishing resistance characteristics. Drop values of MPD and δ_q after polishing were used as classifiers.

- A clustering patterns was developed that classified the studied aggregates into four zones where each zone represents a unique behavior of aggregates with regard to the drop in MPD and δ_q.

APPLICATIONS

This study provides highway agencies and state departments of transportation with accurate, repeatable, and reliable testing methods and algorithms for capturing and measuring the pavement surface texture. The LLS prototype developed as part of this study is practical, simple, reliable and repeatable and produces outcomes that are easy to interpret and use. An additional advantage to this prototype is its larger area coverage compared to CTM and SPT. Using this prototype, larger pavement sections along both the width and the length of the road can be assessed. This system also provides the possibility of obtaining the texture information from 3D data, which increases the efficiency of evaluating the pavement macrotexture. The developed laser prototype and the algorithms can be used in place of traditional methods for quick surveys of pavement surface textures, both on site and in the laboratory.

Furthermore, this system can be employed for monitoring the texture properties of aggregate particles before mix design and pavement construction. The LLS prototype can scan a lot of particles in a significantly shorter time and provide their texture information in real time. This scanning prototype is also applicable in measuring the change in aggregate texture properties to assess their durability and resistance to polishing. The LLS can be used to study the effect of different aggregates polishing strength on pavement long-term performance.

RECOMMENDATIONS

This research study recommends advancing in implementing the LLS prototype and the developed algorithms as a measuring test for pavement surface texture as well as aggregate texture properties. When using the LLS prototype, there is still a need to control traffic in order to measure the pavement surface texture. Accordingly, it is recommended to mount this prototype on a high-speed survey vehicle and scan the pavement, thus eliminating the need to disrupt traffic. As a further recommendation, accurate friction prediction models could be developed based on the texture measurement data to eliminate the need for direct friction measurement. Regarding aggregate classification based on their polishing properties, further research project should include using other clustering methods such as clustering based on a "classification and regression tree" model.

Appendix

```r
## Model-based Clustering

## Step1: clean R Environment

rm(list = ls())

## Step 2 : Install Required Packages

## just run this section for the first time.

# install.packages("mvtnorm")
# install.packages("MASS")
# install.packages("ggplot2")
# install.packages("gtools")
# install.packages("MCMCpack")
# install.packages("plyr")
# install.packages("matrixcalc")
# install.packages("mixtools")

## Step 3: Download Required Libraries

library(mvtnorm)

library(MASS)

library(ggplot2)
library(gtools)

library(MCMCpack)

library(plyr)

library(matrixcalc)

library(mixtools)

## Step 4: Import Your Data

Y <- as.matrix(read.csv("data"))

##plotting data
df <- data.frame(x=Y[,1],y = Y[,2])

ggplot(df, aes(x,y))+
  geom_point()

## Step 5: Find The number of Row and Number of Columns of the Data

n <- nrow(Y)

d <- ncol(Y)

## Step 6: Select the Number of Clusters

K <- 4

## Step 7: Initializing (select K means and covariance matrices)

#means

muu <- matrix(0,nrow =K, ncol =d)
muu[1,] <- c(-2.5, 15)
muu[2,] <- c(-2.5, 15)
muu[3,] <- c(-2.5, 15)
muu[4,] <- c(-2.5, 15)

#covariances

Cov <- array(0, c(K, d, d))
Cov[1,,] <- matrix(c(1,0,0,1),2,2)
Cov[2,,] <- matrix(c(1,0,0,1),2,2)
Cov[3,,] <- matrix(c(1,0,0,1),2,2)
Cov[4,,] <- matrix(c(1,0,0,1),2,2)
```

```r
## Create a list of K means and a list of K covariances

mu1 <- as.list(data.frame(t(muu)))
MyList <- alply(Cov,1)

## Step 8:  Run this section to get the initial classification vector
## pay attention to the message after running this section

alpha <- 2                                  # dirichlet  parameter
w <- rdirichlet(1, matrix(alpha, nrow = K))   # mixture weights of k clusters.

z <- matrix(0, nrow = n)        # Classification vector based on the first developed clusters
for (j in 1:n){
  x_i <- Y[j,]
  p <- mapply(function(x, w_k, cov) w_k *
                dmvnorm(x_i, x, cov), mu1, w, MyList)
  z[j,] <- sample(1:K, size = 1, prob = p)
}


zz <- matrix(0, K, 2)
zz[,1] <- seq(from = 1, to = K, by = 1)

for (k in 1:K) {
  zz[k,2] <- sum(z == k)
}

if(any(zz[,2] <= 5)) {

  print("Select a better initial means and covariances")

} else { print("You are good to go to the next step")
}



## Step 9: Select the number of iterations

nsim <- 2000

## Step 10: MCMC (Running nsim simulations)

#matrices to store the results of each iterations
Z <- matrix(0, nsim + 1, n)
nj <- matrix(0, nsim, K)
sj <- array(0, c(nsim, K, d))
SSj <- array(0, dim = c(nsim, K, d, d))
muj <- array(0, dim = c(nsim + 1, K, d))
Sigmaj <- array(0, dim = c(nsim, K, d, d))


Z[1, ] <- z                     # store the initial classification vector
for (i in 1:K) {
  muj[1,i,] <- matrix(unlist(mu1[i]), nrow = 1, ncol=2) # store the initial means
}

## priors

prior <- list(mu0 = matrix(0, nrow = K, ncol = d), xi0 = 4, Omega0 = diag(d), kappa0 = 1)


# sampler

for (s in 1:nsim) {

  for (j in 1:K) {
    # statistics
    nj[s, j] <- sum(Z[s, ] == j)          # number of data points in cluster j
    if(nj[s,j] < 2) {
      (Omegaj <- prior$Omega0)
       xij <- prior$xi0 +  nj[s, j]
    }

    else{
      Yj <- Y[Z[s, ] == j, ]
      sj[s, j, ] <- apply(Yj, 2, sum)
      SSj[s, j, , ] <- crossprod(Yj)

      # parameters
      ybarj <- sj[s, j, ] / pmax(nj[s, j], 1)
      kappaj <-  nj[s, j]  + prior$kappa0
      muj_mean <- (nj[s, j] * ybarj + prior$kappa0 * prior$mu0[j]) / kappaj
```

```
      xij <- prior$xi0 +  nj[s, j]
      Omegaj <- prior$Omega0 + SSj[s, j, , ]  - nj[s, j] * tcrossprod(ybarj) +
        prior$kappa0 * nj[s, j] / kappaj * tcrossprod(ybarj - prior$mu0[j])
    }
    Lambda <- drop(rWishart(1, xij,  ginv(Omegaj)))
    Signaj[s, j, , ]  <- ginv(Lambda)
    muj[s + 1, j, ] <- rmvnorm(1, muj_mean, Signaj[s, j, , ] / kappaj)
  }

  # update classification vector
  for (i in 1:n) {

    wts <- numeric(K)
    for (j in 1:K) {

      nj_negi <- nj[s, j] - as.integer(Z[s, i] == j)

       ww <- rdirichlet(1, matrix(alpha+nj_negi, nrow = K))   # mixture weights of k clusters.

      wts[j] <-  (ww[j]) *
        pmin(dmvnorm(Y[i, ], muj[s+1, j, ], Signaj[s, j, , ]), 1)
    }

    if (sum(wts) == 0) wts <- rep(1, K)
    wts <- wts + 1e-8
    Z[s + 1, i] <- sample(1:K, size = 1, prob = (wts/sum(wts)))
  }

}

## Step 11: Plotting data along with K clusters


palette(c("green3","black","red", "blue"))


plot(Y[,1], Y[,2], col=Z[nsim,], main = "Scatterplot of the labeled data by using Gibbs sampling", cex.main=0.75)
for (j in 1: K) {
  ellipse((muj[nsim,j,]),(Sigmaj[nsim,j,,]), col=j )
}

## Step 12: Find number of data points assigned to each cluster

NP <- nj[nsim,]

## Step 13: Trace plot of means

matplot(cbind(muj[,1,1],muj[,2,1],muj[,3,1], muj[,4,1]), type='l',
        xlab = "#Iterations", ylab="",
        main = "Trace Plot of Mu[1,1], Mu[2,1], Mu[3,1], Mu[4,1]",
        cex.main = 1)

matplot(cbind(muj[,1,2],muj[,2,2],muj[,3,2], muj[,4,2]), type='l',
        xlab = "#Iterations", ylab="",
        main = "Trace Plot of Mu[1,2], Mu[2,2], Mu[3,2], Mu[4,2]",
        cex.main = 1)
```

References

Ashok, W. R., Panse, M. S. and Apte, H., 2015. Laser Triangulation Based Object Height Measurement. International Journal for Research in Emerging Science and Technology, Vol.2, Issue 3.

AASHTO Provisional Standards, TP 56–03, "Uncompacted Void Content of Coarse Aggregate _As Influenced by Particle Shape, Surface Texture, and Grading_," American Association of State Highway and Transportation Officials, Washington, DC, 2003.

AASHTO T 327, Standard Method of Test for Resistance of Coarse Aggregate to Degradation by Abrasion in the Micro-Deval Apparatus, American Association of State Highway and Transportation Officials, 2016.

Abdul-Malak, M., Fowler, D., and Constantino, C., 1996. Aggregate Characteristics Governing Performance of Seal Coat Highway Overlays. *Transportation Research Record 1547*, Transportation Research Board, Washington, DC, pp. 15–22.

American Association of State Highway and Transportation Officials. The Guide for Pavement Friction, Guidelines for Skid-Resistant Pavement Design. Washington, DC, 2007.

Andriejauskas, T., Vorobjovas, V., and Mielonas, V., 2014. Evaluation of skid resistance characteristics and measurement methods", 9th International Conference of Environmental Engineering, Vilnius, Lithuania.

Anochie-Boateng, J. K., Komba, J. J., and Mvelase, G. M., 2013, Three-dimensional laser scanning technique to quantify aggregate and ballast shape properties. *Journal of Construction and Building Materials*, Vol. 43, pp. 389–398.

Arámbula-Mercado, E., Fernando, E., Hu, S., and Crockford, W., 2018. Application of a Laser Scanning System to Dynamic Friction Test Specimens: Correlation between Texture and Friction, Texas A&M Transportation Institute, FHWA/TX-18/5-6921-01-R1.

Araujo, V.M.C., Bessa, I.S., Branco, V.T.F.C., 2015, Measuring skid resistance of hot mix asphalt using the aggregate image measurement system (AIMS), Construction and Building Materials, 98, 476–481.

Asi, I.M., 2007, Evaluating skid resistance of different asphalt concrete mixes, Build. Environ, 42, 325–329.

ASME. (2009). Surface Texture, Surface Roughness, Waviness, and Lay. ASME B46.1, American Society of Mechanical Engineers, Three Park Avenue, New Work, NY.

ASTM C535-16, Standard Test Method for Resistance to Degradation of Large-Size Coarse Aggregate by Abrasion and Impact in the Los Angeles Machine, ASTM International, West Conshohocken, PA, 2016, www.astm.org

ASTM E867-06, Standard Terminology Relating to Vehicle-Pavement Systems, ASTM International, West Conshohocken, PA, 2012, www.astm.org

ASTM E965-15, Standard Test Method for Measuring Pavement Macrotexture Depth Using a Volumetric Technique, ASTM International, West Conshohocken, PA, 2015, www.astm.org

ASTM Standard D 1252-03, "Standard Test Methods for Uncompacted Void Content of Fine Aggregate _as Influenced by Particle Shape, Surface Texture, and Grading_," Annual Book of ASTM Standards, Vol. 04.02, American Society for Testing and Materials, West Conshohocken, PA, 2003.

Austroads, 2005. Guide to the Management of Road Surface Skid Resistance. Sydney, Australia.

Baraniuk, R., 2009. Signals and Systems", Rice University, Houston TX. http://web.itu.edu.tr/hulyayalcin/Signal_Processing_Books/2003_Richard_Baraniuk_Signals_and_Systems.pdf, Accessed on Nov 18, 2017.

Behrens, M.W., 1999. Wet Weather Accident Reduction Program (WWARP)", Highway Design Division Operations and Procedures Manual, Texas Department of Transportation, Austin, Texas.

Benbow, E., Nesnas, K., and Wright, A., 2006. Shape (surface from) of Local Roads", TTS Research, PPR131 Project Report, Version 2.

Cafiso, S., and Taormina, S., 2007. Texture Analysis of Aggregates for Wearing Courses in Asphalt Pavements, International Journal of Pavement Engineering, 8, 45-54.

Chamroukhia, F., Bartcusa, M., and Glotina, H., 2015. Dirichlet Process Parsimonious Mixtures for clustering. Journal of Elsevier.

Chen, B., Zhang, X., Yu, J., and Wang, Y. 2017. Impact of contact stress distribution on skid resistance of asphalt pavements, Construction and Building Materials, 133, 330–339.

Chowdhury, A., Kassem, E., Aldagari, S., and Massad, E., 2017. Validation of Asphalt Mixture Pavement Skid Prediction Model and Development of Skid Prediction Model for Surface Treatments, Texas A&M Transportation Institute, FHWA/TX-17/0-6746-01-1.

Crouch, L., Gothard, J., Head, G., and Goodwin, W., 1995. Evaluation of Textural Retention of Pavement Surface Aggregates, *Transportation Research Record 1486*, Transportation Research Board, Washington, DC, pp. 124–129.

Dahir, S.H., 1979. A review of aggregate selection criteria for improved wear resistance and skid resistance of bituminous surfaces, Journal of Testing and Evaluation, 7, 245-253.

Dahl, D. B., 2006, Model-Based Clustering for Expression Data via a Dirichlet Process Mixture Model, in Bayesian Inference for Gene Expression and Proteomics, Kim-Anh Do, Peter Müller, Marina Vannucci (Eds.), Cambridge University Press.

Descornet, G., Schmidt, B., Boulet, M., and Gothie, M., 2006. HERMES Project: Harmonization of European Routine and research Measuring Equipment for Skid Resistance. FEHRL report, 2006.

Diebolt, J., and Robert, C. P., 1994. Estimation of Finite Mixture Distributions through Bayesian Sampling. Journal of the Royal Statistical Society. Series B (Methodological), Vol. 56, pp. 363-375.

Do, M.T., and Roe, P., 2008. Report on state-of-the-art of test methods. TYROSAFE project deliverable D04.

Do, M.T., Cerezo, V., 2015. Road Surface Texture and Skid Resistance, Surf. Topogr. Metrol. Prop. Vol.3, DOI:10.1088/2051-672X/3/4/043001.

Do, M.T., Tang, Z., Kane, M., de Larrard, F., 2007. Pavement polishing—Development of a dedicated laboratory test and its correlation with road results. Journal of Wear, Volume 263, Issues 1–6, 10, Pages 36-42.

Dunford, A., 2013, Friction and the Texture of Aggregate Particles Used in the Road Surface Course, Thesis submitted to the University of Nottingham for the degree of Doctor of Philosophy.

Elson, J.M., and Bennett, J.M., 1995, Calculation of the Power Spectral Density from Surface Profile Data, Applied Optics, 34 (1), 201-208.

Ergun, M., Iyinam, S., Iyaniam, A.F., 2005. Prediction of Road Surface Friction Coefficient Using Only Macro- and Microtexture Measurements. Journal of Transportation, DOI**:** 10.1061/(ASCE)0733-947X (2005)131:4(311).

Faranzen, J. Bayesian Inference for a Mixture Model using the Gibbs Sampler. Department of Statistics, University of Stockholm, 2006.

Flintsch, G.W., Luo, Y., and Al-Qadi, I.L., 2005. Analysis of the Effect of Pavement Temperature on the Frictional Properties of Flexible Pavement Surfaces. Presented at 84th Transportation Research Board Annual Meeting, Washington, D.C.

Flintsch, G.W., McGhee. K., Izeppi. E. L., and Najafi, SH., 2012. The Little Book of Tire Pavement Friction. Pavement Surface Properties Consortium.

Hall, J. W., Smith, K. L., Wambold, J. C., Yager, T. J., & Rado, Z., 2009. Guide for Pavement Friction. Washington D.C.: National Cooperative Research Program.

Hall, J.W., Smith, K.L., Titus-Glover, L., Evans, L.D., Wambold, J.C., and Yager, T.J. 2009, "Guide for Pavement Friction", Contractor's Final Report for National Cooperative Highway Research Program (NCHRP) Project 01-43, Transportation Research Board of the National Academies, Washington, D. C.

Hanson, D. I., Prowell, B. D., 2004. Evaluation of Circular Texture Meter for Measuring Surface Texture of Pavements. National Center for Asphalt Technology, Auburn University, NCAT Report 04-05.

Hao, X., Sha, A., Sun, Z., Li, W., and Zhao, H., 2016. Evaluation and Comparison of Real-Time Laser and Electric Sand-Patch Pavement Texture-Depth Measurement Methods. *Journal of Transportation Engineering*: 142(7): 04016022.

Heller, K. A., 2007. Efficient Bayesian Methods for Clustering. PhD Dissertation, University College London.

Henry J.J. 1996. Overview of the International PIARC Experiment to Compare and Harmonize Texture and Skid Resistance Measurements: The International Friction Index. Proceedings of the 3rd International Symposium on Pavement Surface Characteristics, Christchurch, New Zealand, September.

Henry, J.J., 2000, Evaluation of Pavement Friction Characteristics, NCHRP Synthesis of Highway Practice 291, Transportation Research Board, National Research Council.

Henry, J.J, 1983. Comparison of Friction Performance of a Passenger Tire and the ASTM Standard Test Tires. Philadelphia, Pennsylvania.

Hecht, Jeff. Understanding Lasers: An Entry Level Guide. Wiley, 2008.

Hoerner, T.E., and Smith, K.D., 2002. High performance concrete pavement: Pavement texturing and tire-pavement noise, Federal Highway Administration, USA, Report No. FHWA-DTFH61-01-P-00290.

Horne, W.B., 1977. Status of Runway Slipperiness Research. Transportation Research Record, 624, 95-121.

Hsu, H.P., 1995, "Schaum's Outlines of Theory and Problems of Signals and Systems", McGrew-Hill Companies, USA.

Hu, L., Yun, D., Liu, Z., Du, S., Zhang, Z., and Bao, Y., 2016, Effect of three-dimensional macrotexture characteristics on dynamic frictional coefficient of asphalt pavement surface, Construction and Building Materials, 126, 720–729.

Huang, H. and Pan, J., 2006. Speech pitch determination based on Hilbert–Huang transform. Journal of Signal Processing, Vol. 86, pp. 792–803.

ISO 13473-1 (1997), "Characterization of Pavement Texture by Use of Surface Profiles", ISO - International Organization for Standardization.

Jayawickrama P.W. and Thomas, B., 1998. Correction of Field Skid Measurements for Seasonal Variations in Texas. Transportation Research Record 1639, Transportation Research Board, TRB, National Research Council, Washington, D.C.

Jayawickrama, W. P., 1992, Limitation of the Use of Aggregate Sulfate Soundness for the Prediction of Field Performance of HMAC and Seal Coat Pavement Surfaces. Texas Tech University.

Kamel, N. and Gartshore, T., 1982. Ontario's Wet Pavement Accident Reduction Program. ASTM Special Technical Publication 763, American Society of Testing and Materials (ASTM), Philadelphia, PA.

Kamel, N., and Musgrove, G. R., 1981. Design and Performance of Bituminous Mixes in Ontario. RTAC Forum, Vol. 5, Issue 3.

Kandhal, P.S., Bishara, E.A., 1992. Evaluation of Limestone Aggregates in Asphalt Wearing Courses, Phase II, National Center for Asphalt Technology, Auburn University.

Kane, M., Artamendi, I., and Scarpas, T., 2013. Long-term skid resistance of asphalt surfacings: correlation between Wehner– Schulze friction values and the mineralogical composition of the aggregates. Wear, Vol. 303, pp. 235–243.

Karrenberg, U., 2013. Signals, Processes, and Systems, Third edition, Springer Heidelberg Dordrecht London New York.

KEYENCE, Measurement Sensors, http://www.keyence.com/products/measure/index.jsp, Accessed on January 1, 2017.

Kim, H., Hass, C.T., Rauch, A.F., and Browne, C., 2001. A Prototype Laser Scanner for Characterizing Size and Shape parameters in Aggregates. Proceedings of the 9th Annual Symposium, International Center for Aggregate Research, Austin, TX.

Knill D. G., 1960. Petrographical aspects of the polishing of natural roadstones. J Appl Chem, Vol.10: 28−35.

Kulakowski, B.T., Wambold, J.C., Antle, C.E., Lin, C., and Mason, J.M., 1990. Development of a Methodology to Identify and Correct Slippery Pavements. FHWA-PA90-002+88-06. State College, Pennsylvania: The Pennsylvania Transportation Institute.

Liu Q. and Shalaby A., 2015. Relating Concrete Pavement Noise and Friction to ThreeDimensional Texture Parameters. International Journal of Pavement Engineering, DOI: 10.1080/10298436.2015.1095897.

Mahone, D.C., and Sherwood, W.C., 1996. Virginia's Wet Accident Reduction Program: A User's Manual. VTRC 96-R10. Virginia Transportation Research Council, Charlottesville.

Masad E., 2007. Relationship of Aggregate Texture to Asphalt Pavement Skid Resistance Using Image Analysis of Aggregate Shape. Final Report for Highway IDEA Project 114.

Masad, E., 2003. The development of a computer-controlled Image Analysis System for measuring aggregate shape properties. Final report, NCHRP-IDEA Project 77. Transportation Research Board of the National Academies, Washington, D.C.

Masad, E., Rezaei, A., Chowdhury, A., and Harris, P., 2009. Predicting Asphalt Mixture Skid Resistance Based on Aggregate Characteristics. FHWA/TX-09/0 5627-1. FHWA, Texas A&M University.

MATLAB, MathWorks Inc. 2016. MATLAB-Getting Started Guide, Natick, MA.

Meegoda J. N., Hettiarachchi, C.H., Rowe, G.M., Bandara, N., and Sharrock, M.J., 2002. Correlation of Surface Texture, Segregation, and Measurement of Air Voids. Publication FHWA-NJ-2002-026, FHWA.

Meegoda, J.N., and Shengyan, G. 2015. Evaluation of pavement skid resistance using high speed texture measurement. Journal of Traffic and Transportation Engineering, Vol. 2 (6), pp. 382-390.

Miller, M.M. and Johnson, H.D., 1973. Effects of Resistance to Skidding on Accidents: Surface Dressing on an Elevated Section of the M4 Motorway, Report No. LR 542, Transport and Road Research Laboratory, Berkshire, United Kingdom.

Miller, T., Swiertz, D., Tashman, L., Tabatabaee, N., & Bahia, H., 2012. Characterization of asphalt pavement surface texture. Transportation Research Record: Journal of the Transportation Research Board, 2295, 19–26.

Myers, N. O., Characterization of Surface Roughness, Wear, 5 (1962) 182-I89, https://doi.org/10.1016/0043-1648(62)90002-9

Nataadmadja A, Do M.T., Wilson, D., and Costello, S., 2015. Quantifying Aggregate Microtexture with Respect to Wear—Case of New Zealand Aggregates J. Wear 332-3 907–17.

Olshausen, B.A. (2000), "Aliasing", PSC 129, Sensory Processes, http://redwood.berkeley.edu/bruno/npb261/aliasing.pdf, Accessed January 1, 2017.

Ong, G., Fwa, T. and Guo, J., 2005. Modeling Hydroplaning and Effects of Pavement Microtexture. Transportation Research Record: Journal of the Transportation Research Board, Vol.1905, 166-176.

Oppenheim, A., Willsky, A.S., and Nawab, S.H., 1998, Signals & Systems, Second edition, Pearson Education.

Orfanidis, S.J., 1995, Introduction to Signal Processing, US ed Edition, Prentice Hall.

Persson, B.N.J., Tartaglino, U., Albohr, O., and Tosatti, E., 2005. Rubber friction on wet and dry road surfaces: The sealing effect, Physical Review B, 71.

Sandberg, U. 1998. Influence of Road Surface Texture on Traffic Characteristics Related to Environment, Economy, and Safety: A State-of-Art-Study Regarding Measures and measuring Method, VTI notat53A-1997, Swedish National Road Association, Linkoping, Sweden.

Sengoz, B., Topal, A., and Tanyel, S., 2012. Comparison of Pavement Surface Texture Determination by Sand Patch Test and 3D Laser Scanning. *Journal of Periodica Polytechnica Civil Engineering*, 45:73-78.

Serigos, A.P., Smit, A., and Prozzi, J.A, 2014. Incorporating Surface Microtexture in the Prediction of Skid Resistance of Flexible Pavements. Transportation Research Record: Journal of the Transportation Research Board. 2457.105-113.10.3141/2457-11.

Serigos, P.A., Budhavarapu, P., Gorman, G. M., Hong, F., and Prozzi, J.A., 2016. The Contribution of Macro- and Micro-Texture to the Skid Resistance of Flexible Pavement. Center for Transportation Research, SWUTC/16/600451-00085-1.

Slimane, A.B., Khoudeir, M., Brochard, J., and Do, M. T., 2008. Characterization of Road Microtexture by Means of Image Analysis", Wear, Vol. 264, pp. 464-468.

Spiegelhalter, D. J., Best, N. G., Carlin, B. P., 2002. Bayesian Measures of Model Complexity and Fit, Journal of the Royal Statistical Society. Series B (Statistical Methodology), vol. 64, no. 4, pp. 583-639.

Texas Department of Transportation (TxDOT), 2016. Bituminous Rated Source Quality Catalog, Construction Division, Materials & Pavements (CST-M&P). ftp://ftp.dot.state.tx.us/pub/txdot-info/cmd/mpl/brsqc.pdf

Thomas, L, 2008. Grip-Tester MK2 D-type Maintenance Manual. Issue 4, Findlay, Irvine Limited, Scotland.

TRL, 2002. Transportation Research Laboratory, Incident on 28 February 2001 at Little Heck Railway Bridge, The Highways Agency of the Department for Transport, UK.

Ueckermann, A., Wang, D., Oeser, M., and Steinauer, B., 2015. A contribution to non-contact skid resistance measurement. International Journal of Pavement Engineering, Vol. 16, No. 7, 646–659, http://dx.doi.org/10.1080/10298436.2014.943216.

Wang, D., Liu, P., Wang, H., Ueckermann, A., and Oeser, M., 2017. Modeling and testing of road surface aggregate wearing behavior. Journal of Construction and Building Materials, Vol. 131, pp. 129–137.

Wang, H., and Wang, Z, 2013. Evaluation of pavement surface friction subject to various pavement preservation treatments, Construction and Building Materials, 48, 194–202.

Wang, L., Druta, C., and Lane, S.D., 2010. Methods for Assessing the Polishing Characteristics of Coarse Aggregates for Use in Pavement Surface Layers. Virginia Department of Transportation, Report No. FHWA/VTRC 10-CR7.

Wang, L., Wang, X., Mohammad, L., and Abadie, C, 2005. Unified Method to Quantify Aggregate Shape Angularity and Texture Using Fourier Analysis, Journal of Materials in Civil Engineering, 17 (5), 498-504.

Webb, J.W., 1970. The Wearing Characteristics of Mineral Aggregates in Highway Pavements. VHTRC 70-R7. Virginia Highway Transportation Research Council, Charlottesville.

Wilson, D.J., B. Jacobsen, and B. Chan, 2013. NZ Transport Agency research report 523: The effect of road roughness (and test speed) on GripTester measurements. NZ Transport Agency.

Woodward, W., Woodside, A.R., Jellie, J.H., 2002. Development of Early Life Skid Resistance for High Stone Content Asphalt Mixes. Proceedings of the 3rd International Conference on Bituminous Mixtures and Pavements, Thessaloniki, Greece.

World Health Organization, 2015. Global Status Report on Road Safety, Department of Violence & Injury Prevention & Disability (VIP).

Yang, G., 2017. Exploring Pavement Texture and Surface Skid Resistance Using Soft Computing Techniques. Doctoral Dissertation, Oklahoma State University.

Yildirim, I., 2012. Bayesian Inference: Gibbs Sampling, Department of Brain and Cognitive Sciences, University of Rochester.

Yoo, Y., 2001. Tutorial on Fourier Theory. http://www.cs.otago.ac.nz/cosc453/student_tutorials/fourier_analysis.pdf, Accessed on January 18, 2017.

Zuniga, N., 2017. Predicting Friction with Improved Texture Characterization, Master Thesis, University of Texas at Austin.